# Passive visible light communications

Ghiasi, S.K.

**DOI**
10.4233/uuid:3fe10afb-f073-4cc4-9fd1-1b2b3726bcb7

**Publication date**
2024

**Document Version**
Final published version

**Citation (APA)**
Ghiasi, S. K. (2024). *Passive visible light communications*. [Dissertation (TU Delft), Delft University of Technology]. https://doi.org/10.4233/uuid:3fe10afb-f073-4cc4-9fd1-1b2b3726bcb7

# Passive Visible Light Communications

# PASSIVE VISIBLE LIGHT COMMUNICATIONS

## Dissertation

for the purpose of obtaining the degree of doctor
at Delft University of Technology,
by the authority of the Rector Magnificus, prof. dr. ir. T.H.J.J. van der Hagen,
chair of the Board for Doctorates
to be defended publicly on
Wednesday 26 June 2024 at 12:30 o'clock

by

**Seyed Keyarash GHIASI**

Master of Science in Electrical Engineering and Information Techonology,
Eidgenössische Technische Hochschule (ETH), Zürich, Switzerland
born in Shiraz, Iran.

This dissertation has been approved by the promotors.

promotor: Prof. dr. K.G. Langendoen
promotor: Dr. M.A. Zuñiga Zamalloa

Composition of the doctoral committee:

| | |
|---|---|
| Rector Magnificus, | Chairman |
| Prof. dr. K.G. Langendoen | Delft University of Technology, promotor |
| Dr. M.A. Zuñiga Zamalloa | Delft University of Technology, promotor |
| | |
| *Independent members:* | |
| Prof.dr.ir. O. Isabella | Delft University of Technology |
| Prof.dr. O. Landsiedel | Kiel University, Germany |
| Dr. O. Durmaz | University of Twente |
| Dr. D. Giustiniano | IMDEA Networks & Universidad Carlos III de Madrid |
| Prof.dr. A.E. Zaidman | Delft University of Technology, reserve member |

This thesis has been part of the *LuxSenz* project, a *TOP-Grant, Module 1, Physical Sciences* with project number 612.001.854, which is financed by the Dutch Research Council (NWO).

*Keywords:* Passive visible light communication, Internet-of-Things, Embedded systems



ISBN 978-94-6384-603-5

An electronic version of this dissertation is available at
http://repository.tudelft.nl/.

# CONTENTS

# SUMMARY

The increasing number of portable electronics and Internet of Things (IoT) devices demand scalable, low-power, and versatile networks. The Radio Frequency (RF) band has long been the main carrier for communication technologies. For instance, Bluetooth, Wi-Fi, and LoRa are assigned specific RF bands and use matured techniques to avoid infringing other regions of the spectrum. However, the high number of RF devices make interference between those in the same band inevitable. Furthermore, the growing number of RF applications increases the demand for bandwidth, making it a costly resource.

To solve these issues, researchers are exploring other parts of the electromagnetic spectrum. A wide, free, and prevalent candidate is visible light. In this regard, Light-Emitting Diode (LED)s and lamps have been explored in building Visible Light Communication (VLC) platforms. However, all light emitting devices require power in the order of several watts, even the most power-efficient LEDs. This amount is difficult to afford by low-power and IoT devices. Therefore, a new communication paradigm has emerged in VLC, called passive VLC.

In passive VLC, a platform, instead of generating light, modulates the light in the environment to transmit data. A passive transmitter relies on other light sources, such as the sun or a ceiling lamp; it modulates the already-generated light, and redirects it towards a receiver. Although very promising in lowering power consumption, this method is not as easy to apply. Modulating light out of its source is a big challenge. Until now, various technologies have been used for this purpose, including Liquid Crystal (LC)s, Digital Micro-Mirror Device (DMD)s, and piezoelectric modulators, each with downsides and advantages. Among these, the most power-efficient are LCs, consuming in the order of microwatts. Nevertheless, this appealing low power comes at a price: they have an inherently low bandwidth, where the typical LC has a maximum switching frequency of few hundreds of Hz.

Motivated by their ultra low power prospects, we investigate LCs to overcome their disadvantages. We delve into their physical properties, use them as transmitters, and make systematic guidelines to increase the data rate of LC-based transmitters. As a result, we uncover new ways of operating LC cells. In addition, we bring the well-known concepts and methods of classical communications to the context of passive VLC, such as Multiple-Input Multiple-Output (MIMO), which has been proven to increase the data rate of a communication link. Lastly, besides technical enhancements, we investigate possible use cases of passive communications in people's daily lives, so as to pave the way for the adoption of this nascent area.

In short, we investigate the solutions to the low data rate of LCs, as well as their integration and acceptance as a novel method of communication.

# SAMENVATTING

Het toenemende aantal draagbare elektronica en Internet of Things (IoT)-apparaten vraagt om schaalbare, energiezuinige en veelzijdige netwerken. Het radiofrequentie (RF) spectrum is al sinds lange tijd de belangrijkste drager van communicatietechnologieën. Bluetooth, Wi-Fi, en LoRa bijvoorbeeld krijgen specifieke RF-banden toegewezen en gebruiken geavanceerde technieken om overspraak in andere delen van het spectrum te voorkomen. Het toenemende aantal RF-apparaten maakt storingen binnen dezelfde frequentie band echter onvermijdelijk. Dat effect wordt bovendien nog versterkt door de immer groeiende vraag naar bandbreedte van moderne draadloze toepassingen, waardoor het RF spectrum kostbaar wordt.

Om deze problemen op te lossen, worden tegenwoordig ook andere delen van het elektromagnetische spectrum onderzocht. Een breedbandige, vrij beschikbare en veel genoemde kandidaat is het zichtbare licht. In dit verband zijn lichtgevende diodes (leds) en lampen onderzocht als bouwstenen van VLC-platforms (Visible Light Communication). Alle lichtgevende apparaten vereisen echter een vermogen van enkele Watt's, zelfs de energiezuinigste leds. Zulke hoeveelheden zijn moeilijk op te brengen voor energiezuinige apparaten. Daarom is er een nieuw communicatieparadigma ontstaan genaamd passive VLC .

Bij passive VLC genereert een zender geen licht, maar moduleert het omgevingslicht om gegevens te versturen. Een passieve zender vertrouwt op andere lichtbronnen, zoals de zon of lamplicht; hij moduleert het reeds gegenereerde licht en stuurt het door naar een ontvanger. Hoewel deze methode veelbelovend is voor het verlagen van het energieverbruik, is ze niet zo gemakkelijk toe te passen. Het moduleren van licht uit een externe bron is een grote uitdaging. Tot nu toe zijn hiervoor verschillende technologieën gebruikt, waaronder Liquid Crystal (LC)s, Digital Micro-Mirror Device (DMD)s en piëzoelektrische modulatoren, elk met eigen voor- en nadelen. De meest energiezuinige LC's verbruiken in de orde van microwatts. Aan dit aantrekkelijke lage vermogen hangt echter een prijskaartje: ze hebben een inherent lage bandbreedte, waarbij typische LC's een maximale schakelfrequentie hebben van enkele honderden Hz.

Vanwege het vooruitzicht op ultralaag vermogen, onderzoeken we de fundamentele eigenschappen van LC's in dit proefschrift om zo de nadelen te kunnen adresseren. We verdiepen ons in de fysische eigenschappen, en gebruiken die op een vernieuwende, systematische manier om de datasnelheid van LC-gebaseerde zenders te verhogen. Daarnaast brengen we bekende concepten en methoden van klassieke communicatietechnieken over naar de context van passive VLC, zoals Multiple-Input Multiple-Output (MIMO), waarvan bewezen is dat het de gegevenssnelheid van een communicatieverbinding drastisch verhoogt. Tot slot onderzoeken we, naast technische verbeteringen, mogelijke gebruiksscenario's van passieve communicatie in het dagelijks leven, om zo de weg vrij te maken voor de toepassing van deze opkomende vorm van VLC.

Samenvattend, in dit proefschrift onderzoeken we technieken om de lage datasnelheid van LC's te verhogen, evenals hun integratie en acceptatie als nieuwe communicatiemethode voor energiezuinige apparaten.

# 1

# INTRODUCTION

The number of IoT and portable devices has seen a surge and continues to grow [1, 2, 3]. One of the most important requirements of these devices is performing wireless communications. Traditionally, RF has been the main carrier in wireless networks. It is already well-established and widespread, and most IoT devices implement several RF technologies such as Bluetooth, Wi-Fi, and LoRA, each targeting a specific range of needs. The viability of these devices has been proven over the years, however, this omnipresence is facing a big barrier. As the number of RF users increases, the radio spectrum–which is the most valuable resource–must be shared among more applications. This translates to more interference, higher spectrum costs, and stricter regulations. To solve these issues, RF researchers have used elaborate techniques, such as MIMO [4, 5, 6] and time or frequency sharing [7, 8]. However, the most fundamental challenge still exists: available RF bandwidth is becoming scarcer, which requires looking for new fundamental solutions.

## 1.1. BEYOND RADIO FREQUENCY

Historically, the first forms of wireless communication were based on visible light. In 1880, Alexander Graham Bell invented the Photophone [9]: a device that used sunlight reflections to transmit human voice. After this invention, however, the strong emergence of radio made it the prevalent communication technology instead. Radio can traverse obstacles, has more coverage than light, and is cheap to generate on silicon. However, as mentioned before, assigning RF bandwidth to novel applications is expensive and requires strict regulations by governing bodies such as the Federal Communications Commission (FCC) [10]. To ameliorate these shortcomings, researchers are looking for bandwidth beyond the traditional RF. During the last decade, a technology called Visible Light Communication (VLC) has gained significant attention, as it is unlicensed, relatively cheap, and has a wider bandwidth than RF (refer to Figure 1.1). VLC modulates the intensity of standard LEDs to transmit wireless data. Given the pervasive presence of light in our environments, VLC can be a suitable candidate to empower emerging IoT devices and applications. In addition, VLC has been identified as a key technology for 5G as its devices fare well on bandwidth, spectral efficiency, and form factor [11].

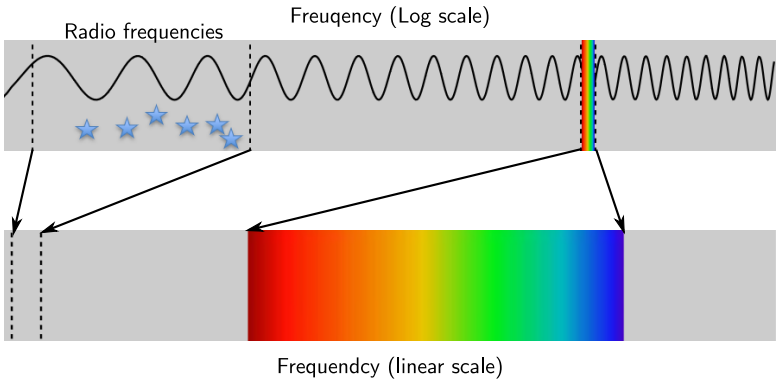


Figure 1.1: Electromagnetic spectrum on two scales: logarithmic and linear. RF-band applications are marked by stars.

### 1.1.1. VISIBLE LIGHT COMMUNICATION

Nowadays, any object with an LED can be transformed into a wireless transmitter, and thanks to their energy efficiency, LEDs are present in various types of objects, not only in ceiling and car lights, but also in home appliances and clothes. The widespread presence of LEDs, together with advancements in VLC, is leading to a wide range of novel applications, from the design of a new generation of toys [12] and indoor positioning systems [13] to human sensing [14]. VLC technology has reached the consumer market as well. Systems such as RONJA [15] and LiFi [16, 17] are examples of this, which transmit at a comparable speed to Wi-Fi using LEDs.

These VLC applications have proven to be desirable alternatives to RF, however, they cannot be adopted in many IoT devices due to their energy consumption. Most VLC transmitters are too power-hungry. For instance, an LED [18] consumes about 100 mW to emit a very low luminous flux of 70 Lux at a distance of 1 m[1]. Emitting light causes a high energy consumption, even from LEDs, which are a relatively low-power solution for illumination.

To reduce this high power, the following observation has inspired the researchers to move towards low-power VLC: **instead of using power to generate light, devices could exploit the light in our environment and use it directly for communications**. As a result, a new VLC paradigm has been proposed with a similar mindset as RF backscattering [19, 20, 21], where devices exploit the surrounding radio waves for communication instead of using power to generate new waves.

### 1.1.2. A LOW-POWER COMMUNICATION PARADIGM

To bring VLC to low-power applications, recent trends introduce *backscattering* communications with light. Similar to its concept in RF, instead of using a light-emitting device, a transmitter can use *ambient* light as the physical carrier, shown in Figure 1.2b. Thus, this type of communication relies on external light sources, such as natural sunlight or

[1] To put numbers in perspective, the minimum suggested flux for an office environment is about 500 Lux. Besides, sunlight is more than 20 kLux.

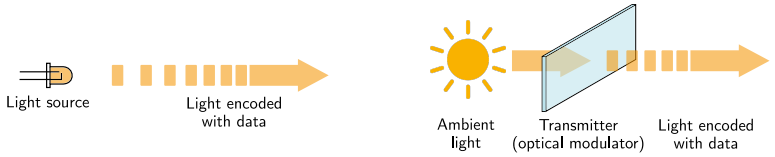


(a) Active VLC: a light source is modulated *directly* to emit light in certain patterns.

(b) Passive VLC: a special device (light modulator) creates patterns with ambient light.

Figure 1.2: An abstract depiction of active and passive VLC.

artificial light radiated by ceiling lamps. The omission of the light source in a VLC transmitter reduces the power consumption significantly–from several watts down to tens of microwatts. In the state-of-the-art (SoA), the traditional VLC systems controlling LEDs directly are called *active* and the systems using ambient light are called *passive*. A passive VLC transmitter modulates and redirects ambient light towards an optical receiver.

Although passive and active VLC links have several properties in common (e.g. their receivers are the same), their transmitters have different working principles. While active transmitters need to control a simple *electronic component*, such as an LED, passive ones need to control more sophisticated *electro-optical modulators*. There are several types of passive modulators and each varies in technology, power consumption, cost, voltage requirements, etc. Thus, a deep investigation of passive transmitters is necessary. In Section 1.1.3, we will briefly describe various passive VLC modulators used by the SoA for different IoT applications. However, many of these prototypes were designed in an experimental manner, rather than using a principled approach. As a result, there is still a lack of comprehensive methods for designing low-power passive transmitters. In this thesis, we address this challenge. However, before proceeding into more details, we introduce some fundamental building blocks of a (passive) VLC link, i.e. the transmitters and receivers.

### 1.1.3. PASSIVE VLC: THE BIG PICTURE

Similar to any communication system, there are numerous blocks constituting a passive VLC link, such as the transmitter and receiver hardware, channel model, coding techniques, and (de)modulation. The focus of this thesis is on challenges in the physical layer of VLC. Thus, we briefly mention the hardware used in passive receivers and transmitters

#### RECEIVER

In VLC systems, optically-sensitive components are used as receivers, such as photodiodes, cameras, color sensors, and spectrometers. While there is no fundamental difference between receivers of active and passive links, active systems predominantly focus on photodiodes and cameras. Below, we describe some of the most popular photosensors used in the SoA.

1. **Photodiodes and analog color sensors:** These are high-speed components to measure light intensity. Some analog color sensors are made when a photodiode's

aperture is covered by a color filter. Therefore, they are the same in operation and typical characteristics.

2. **Spectrometers:** They measure light intensity at fine wavelength divisions. This allows for a more accurate measurement of light and its properties. Their disadvantage compared to photodiodes is their much lower speed due to their higher precision. Besides, they are expensive.

3. **Cameras:** In addition to their regular use as image sensors, they found their use in screen-to-camera communication research papers [22, 23, 24, 25]. They are similar to large arrays of photodiodes, making them a good candidate as optical receivers. However, cameras have typically a much lower speed than the previous two devices, working at a maximum of 240 Frames Per Second (FPS).

These devices show a trade-off between speed and granularity. On the one hand, photodiodes and color sensors provide a high bandwidth by having only one pixel. On the other hand, cameras provide millions of pixels while operating at a slow speed. Spectrometers, different from the other two groups, provide valuable spectral information, while working at a medium sampling rate. In this thesis, we investigate all of these devices and use their advantages accordingly.

### TRANSMITTER

A passive transmitter interacts with ambient light and modulates light properties including intensity, spectrum, and polarization. The electro-optical modulators that show most promise for passive VLC are explained next:

1. **Liquid Crystal (LC) modulators:** These devices can be defined as optical shutters that either block light or let it pass through. To control the transparency level of the cell, LC modulators change the polarization direction of light. LCs are easily controlled when a voltage is placed on their two terminals. These modulators are low-cost, easy to manufacture, and broad-band (they can interact with an extensive range of light wavelengths). Additionally, they consume low power. However, they have a low switching speed (hundreds of Hz), resulting in low data rates.

2. **Digital Micro-Mirror Devices (DMD):** These modulators are arrays of tiny mirrors that reflect light in different directions. The dimension of the arrays does not exceed a few $mm^2$, and are primarily used in making over-head projectors. With a proper control voltage, they can act as a passive light modulator by directing light towards an intended receiver or a light absorber. DMDs are broad-band and have medium switching speeds in the order of tens of kHz. Their main disadvantage is the limited surface area. Due to which their Signal-to-Noise Ratio (SNR) drops rapidly at longer distances, although they have been used as modulators in passive VLC [26].

3. **Piezoelectric crystals:** Piezoelectric devices have electromechanical properties that change their structure when a voltage is applied on them. This change is enough to shift the direction or polarization of light, thus, making them suitable passive modulators. Piezoelectric devices have a very high bandwidth, and can

transmit data at a few megahertz. These crystals are widely used to modulate laser beams in experimental scenarios. The main limitation of these modulators is their need of high voltages for operation. Besides, they usually have a small form factor.

Among these devices, LC cells are the most suitable for low-power IoT applications: they are broad-band, relatively low-cost, and low-voltage. Despite the vast usage of these cells in passive VLC, they still have a significant bottleneck: their low bandwidth. These devices have a very slow electro-optical response; most of them can only modulate light at a few hundred Hz. For instance, a typical LC cell has a maximum bandwidth of 300 Hz. Therefore, a central research problem in passive VLC is developing links of higher data rates using LC cells. This thesis takes a step towards this goal.

## 1.2. PROBLEM STATEMENT

The quest towards faster passive links is an overarching problem covering various research areas. For example, investigating faster LC materials, developing cells with better structures, and adopting multiplexing techniques are all subjects of recent SoA studies that will be discussed in Chapter 2. Based on the SoA, we found that LC modulators are not deeply understood in the passive VLC community, as they are quite new and unexplored. Within the scope of this thesis, we do not delve into designing better LC cells, however, we try to understand the working principles of LC modulators and build upon their fundamental properties. Furthermore, we noticed there are few user applications in the SoA, which is an important limitation, since novel applications play an important role in adopting a new technology such as passive VLC.

These challenges, i.e. increasing data rates and novel applications, lead us to ask the research questions presented in the next subsections.

### 1.2.1. RESEARCH QUESTIONS

We structure the described challenges in three research questions. The first two questions aim at implementing a solid physical layer in passive VLC links, and the third one concerns novel applications.

1. Can we exploit the inherent physical properties of liquid crystals to increase the data rate?

In Chapter 2, we give a primer on LC cells, and show how they were traditionally used as light switches to modulate light. This picture helps to understand most of the SoA. However, the perception of LCs as a mere light shutter is too simplified. In fact, these cells can interact with light based on its wavelength and make phase shifts in light waves. Some of the SoA take advantage of this fact in a static manner to create localization signs and markers [24, 22]. Nevertheless, a well-formulated guideline to using these properties was lacking in the SoA. To address this gap, we introduce ChromaLux in Chapter 3. It prototypes a passive link taking advantage of a deeper analysis of LC properties. This work follows a principled approach to reach data rates of about 20× more than its predecessors. Additionally, it lays out a step-by-step guideline on designing and tuning a passive transmitter.

ChromaLux gives more insight into LCs. However, it uses a narrow portion of the visible light spectrum and does not achieve spectral efficiency. In Chapter 4, we propose SpectraLux, which uses the guidelines of Chapter 3 and expands it to use the visible light's full spectrum. Instead of modulating only two symbols, '0' and '1', SpectraLux sends multiple symbols, with each symbol carrying multiple bits. This bigger number of symbols spreads across the entire light spectrum and increases the data rate.

Both ChromaLux (Chapter 3) and SpectraLux (Chapter 4) are Single-Input Single-Output (SISO) systems. They have one modulator and one photosensor, which only allows creating a *single* channel. During the designs of the first two systems, we found that properties of modulated light, such as polarization and color, could allow the creation of a MIMO system with multiple channels. This insight led us to ask our second research question:

> 2. What adaptations are required to implement efficient MIMO techniques with liquid crystals?

Among the SoA, there is only one paper implementing a *true* MIMO link with transmitters working in parallel (RetroMUMIMO [27]). However, it only explores a limited subset of LC properties to make its MIMO system. Furthermore, it requires gathering a large data set of LC responses to train the receiver.

Chapter 5 presents a more efficient solution to this question of achieving a MIMO system. In particular, we implement a Multi-User MIMO (MUMIMO) link [28][2]. We formulate a novel method using LC cells, modeling the passive MUMIMO link, and analyzing an upper bound of the maximum number of parallel channels. Our framework shows that each MUMIMO channel can work independently of the others. Achieving in that way an almost linear performance where the link's total speed-up equals the number of MUMIMO channels.

The two previous research questions tackle challenges at the physical layer of LC-based systems. However, they do not take into account the potential users, ease-of-use, responsiveness, integration into the environment, etc. As one of the final goals of passive VLC is its use in common devices, coming up with real-life applications is also required. Thus, we pose the following research question:

> 3. What kind of applications can be developed with novel liquid crystal panels?

This question is answered in Chapter 6, where we present a passive screen-to-camera communication link. In the SoA, several studies are investigating the unobtrusive encoding of data in videos. In these studies, people see a normal video in a display, however, smartphone cameras can decode hidden information embedded inside the video.

In Chapter 6, we show that a Liquid Crystal Display (LCD) monitor can be categorized as an LC-based transmitter, since it has a similar internal structure as the transmitters of Chapters 3, 4, and 5. However, LCDs are equipped with powerful backlights to enable them operating in all lighting conditions. To make a passive LCD, we remove its backlight and place it on a window to make it work with sunlight. Instead of utilizing a large amount of energy to power the monitor's backlight, sunlight provides that functionality.

[2] As we only consider a Multi-User case, we use the term MUMIMO and MIMO interchangeably.

A passive LCD could both be seen as a smart window that is transparent when operating as a normal glass panel, and display images that overlay the window's view. These smart windows are already in use in public places–such as buses, airports, and office spaces– displaying relevant information to users. Combined with the methods in screen-to-camera communication, passive LCDs could be also used as wireless transmitters, displaying videos to people but also hidden (embedded) data to the user's smartphones. Transmitting data on these displays takes a step forward to bringing passive VLC applications to public users.

In the end, the research questions posed above help shifting the existing paradigms in designing passive VLC links, as well as revealing their potential applications.

### 1.2.2. RELATED PUBLICATIONS

As part of our contributions, we prepared the following publications, some of which were under submission at the time the thesis was compiled.

1. Seyed Keyarash Ghiasi, Marco A. Zúñiga Zamalloa, and Koen Langendoen. A principled design for passive light communication. In ACM MobiCom '21 .

   DOI: 10.1145/3447993.3448629

2. Seyed Keyarash Ghiasi, Vivian Dsouza, Koen Langendoen, and Marco Zuniga. SpectraLux: Towards Exploiting the Full Spectrum with Passive VLC. In IEEE/ACM IPSN '23 .

   DOI: 10.1145/3583120.3586966

3. Seyed Keyarash Ghiasi and Marco Zuniga. "PassiveMUMIMO:A General MIMO Framework for Passive Communications with Ambient Light".

   Under submission.

4. Seyed Keyarash Ghiasi, Marco Kaldenbach, and Marco Zuniga. "Passive Screen-to-Camera Communication".

   Under submission.

# 2

# BACKGROUND AND RELATED WORK

Designing passive VLC transmitters requires optical modulators. Since our aim is the application of these devices in IoT scenarios, they must meet specific requirements including being low-voltage, low-power, relatively cheap, and easy to manufacture. More importantly, a desirable modulator must have a low response time (a high switching speed) and a wide spectral bandwidth (to be effective on a wide range of visible light wavelengths). In Chapter 1, we briefly mentioned three types of optical modulators: LCs, Digital Micro-Mirror Devices (DMD)s, and piezoelectric crystals. The proper use of these technologies depends on the requirements of the transmitter. To provide a comparison guide, their most important aspects are summarized in Table 2.1.

| Technology | Switching speed | Voltage range | Power consumption | Spectral bandwidth |
|---|---|---|---|---|
| Liquid crystal (LC) [29] | few hundreds of Hz | **3.3 to 5 V** | **few micro-watts to few watts** | **wide** |
| DMD [30] | tens of kHz (full frame) | < 4 V | 45 mW | **wide** |
| Piezoelectric crystal [31] | **few MHz** | > 10 V | several watts | **wide**, mostly designed for laser beams |

Table 2.1: Comparison of popular passive light modulators

In Table Table 2.1, the *best* candidate for each criterion is put in boldface. LCs perform well on all aspects except for switching speed. Despite this, LCs seem to be one of the most suitable choices for IoT for two reasons: first, many applications–such as localization– can still be satisfied with lower data rates, and second, some research works have shown the potential to build links of higher data rates using LC cells with low speeds [32, 33, 34]. Therefore, we also focus on LC transmitters. However, before moving to the description of the SoA as well as the novelties of this thesis, we recap the most basic properties of LC cells.

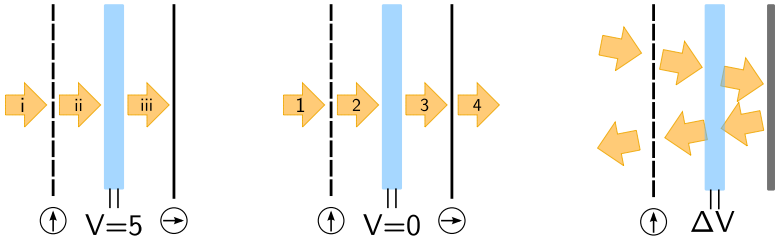


(a) A transmissive cell in 'off' state (b) A transmissive cell in 'on' state. (c) Reflective structure of a cell

Figure 2.1: LC types and modes of operation: (a) an LC cell in its 'off' state. (i) Unpolarized light hits the polarizer (dashed line) and (ii) becomes polarized. (iii) After crossing the crystal, the polarization direction does not change. In this case, a second polarizer, called the analyzer (solid line), blocks the light. (b) The same cell of Figure (a) in its 'on' state. Light in stages (1) and (2) has the same properties as (i) and (ii) in the first image, but between (2) and (3), the LC cell shifts the light's polarization by $\theta_{LC}$°. Therefore, (4) the light is allowed to exit from the analyzer. Finally, (c) depicts a reflective cell configuration, which has only one polarizing sheet and a reflective surface (gray bar).

## 2.1. A PRIMER ON LC MODULATORS

Liquid Crystals (LC)s are a family of chemical materials with unique optical characteristics [35]. At room temperature, they are in a crystal-like form between pure solid and liquid, and they appear transparent to light. When a *polarized* light ray crosses a layer of this material, its polarization direction rotates depending on the type, thickness, and structure of that LC layer. A useful property of the LCs is that in the presence of an external electric field (voltage), their structure changes slightly. This change is enough to incur a different amount of rotation in the light's polarization. Therefore, controlling this electric field (voltage) leads to arbitrary rotations in the polarization of a light ray.

To make an electro-optical modulator, a layer of LC is put between two conductive glass electrodes[1][2]. These electrodes apply an electric field on the LC layer changing its structure, which in turn shifts the crossing light's polarization, hence *modulating* the signal. However, most photosensitive devices measure light intensity, not polarization. Therefore, changes in polarization have to be converted to intensity variations so that it can be measured. This is done by adding two polarizing sheets to an LC cell: the first one–called the polarizer–is used to polarize the light entering the modulator, and the second one–called the analyzer– sits at the exit path of light. With this modification, first, the ambient light becomes polarized in the direction of the polarizer (with a direction of $\theta_p$). Then, as it passes the LC layer, its polarization rotates by $\theta_{LC}$. The value of $\theta_{LC}$ is determined by the voltage on the cell . After this stage, the light that is now polarized with the angle $\theta_p + \theta_{LC}$ encounters the analyzer with the orientation of $\theta_a$. According to Malus' law, the intensity of light coming out of the analyzer is determined by the following equation:

$$A_o = A_i Cos^2(\theta_p + \theta_{LC} - \theta_a) \tag{2.1}$$

where $A_o$ and $A_i$ are the output and input light intensities, $\theta_p$ and $\theta_a$ are the polarizer and analyzer orientations, and $\theta_{LC}$ is the polarization offset made by the cell and is the

[1] In reflective modulators, only one of these electrodes has to be transparent, and the other one reflective.
[2] The electrodes are made by depositing a layer of Indium Tin Oxide (ITO) on glass.

only parameter that a user can dynamically change . This allows an LC cell to output various levels of light ranging from transparent (Figure 2.1b) to opaque (Figure 2.1a), thus creating a modulator.

The cells that we described above are called *transmissive*, which let the light pass through. In almost all transmissive LC cells, the polarizer and analyzer are orthogonal. LC cells can also be manufactured to reflect the modulated light, shown in Figure 2.1c. In the reflective case, $\theta_p$ is equal to $\theta_a$, as the system uses only one polarizing sheet.

The description above draws an overarching picture of LC cells. In practice, manufactured cells can have different types, depending on their internal structure and the type of LC material. In the following section, we explain three different cells, which are either used in this thesis or by the relevant SoA.

### 2.1.1. TYPES OF LC MODULATORS

We explain the operation of the three most used modulators: Twisted Nematic (TN) cells, Pi cells, and Ferroelectric Liquid Crystals (FLCs). These cells have different power consumptions, switching speeds, and driver circuits.

#### TWISTED NEMATIC (TN) CELLS

These cells have the structure mentioned before: two transparent electrodes sandwiching a layer of Liquid Crystal. Their unique property is that electrodes are made with microscopic grooves on their inner surfaces. As a result, LC molecules attach to these grooves and align in their direction. In a TN cell, the grooves of one electrode are orthogonal to the other's. Thus, the molecules experience a 90° twist across the LC layer, hence the name Twisted Nematic[3]. This is shown in Figure 2.2. When a high enough voltage (e.g. 5 V) appears on the electrodes, the molecules rotate and the twist vanishes, When the voltage is released, the molecules return to their initial twisted form. Another important property is that any voltage between 0 and 5 v puts the molecules in an intermediate twist angle.

Next, we use the notation of Equation 2.1 to describe the behavior of these cells. In simple terms, when light enters the LC layer, its polarization direction ($\theta_p$) rotates the same amount as the twist angle of the molecules ($\theta_{LC}$). Thus, when there is no voltage, $\theta_{LC} = 90°$. On the other hand, when there is 5 v on the cell, the LC is untwisted ($\theta_{LC} = 0$), and the light reaches the analyzer with its initial polarization direction ($\theta_p$). In an LC cell, the polarizer and analyzer are normally perpendicular. Thus, in the first case, Equation 2.1 yields $A_o = A_i$, letting the light pass through, whereas in the second case, it results in $A_o = 0$, meaning that the light is blocked by the cell. Considering this behavior, which is illustrated in Figure 2.2, LC cells are also called light valves.

In passive VLC, in addition to the *static* characteristics of TN cells, their dynamic behavior–or switching speed–defines the available bandwidth. In Chapter 3, we will show that in most TN cells, the bandwidth bottleneck appears when the cells transition from a higher voltage to a lower one, e.g. when a falling pulse of 5 v to 0 v is applied. In such situations, LC molecules rely on their *weak* internal forces to reach their initial twisted state. In contrast, when a higher voltage is applied, those molecules swiftly

[3] "Nematic" denotes the property of LC molecules that align in mostly parallel lines, not in planes [36].

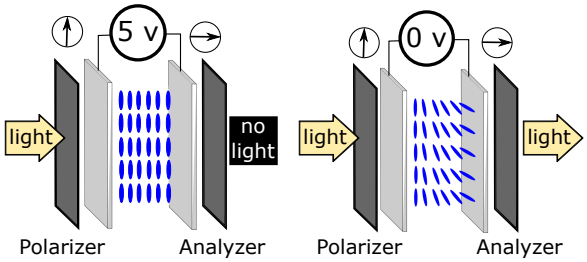


Figure 2.2: The operation of a liquid crystal cell.

straightened thanks to the large forces of the electric field. To put these two cases in perspective, our setup of Chapter 3 measures the rising pulse of a cell to take about 1 ms, whereas its falling pulse takes 5 ms.

The description presented in this chapter helps to understand why most of the SoA uses LC as light valves. However, in Chapter 3, we will show that the simplified model of a *light valve* neglects a beneficial property of LCs that can be used to increase the switching speed.

### PI CELLS

These light modulators are made similar to TN cells. They have a thin liquid crystal layer between two glass electrodes. However, the grooves on the inner side of one electrode are parallel to those of the other electrode. This structure helps LC molecules adjust faster when the voltage is released, making for a shorter switching time [37]. From a micro perspective, the Pi cells alleviate a fluid dynamics effect in TN cells called *backflow effect*, which is explained in more detail in Chapter 3.

Pi cells, despite solving the issue of switching speed, introduce two main disadvantages. First, they require a more elaborate driving voltage than their TN counterparts. For instance, a typical driving voltage for Pi cells is in the order of tens of volts, instead of five volts. Besides the higher voltage requirement, applying simple *high* and *low* pulses cannot properly turn these cells *on* and *off*, instead, an amplitude-modulated high-frequency voltage is needed[4], similar to the waveform in Figure 2.3. In this figure, the envelope of the signal decides the *on* and *off* switching pattern of the Pi cell. This requirement causes the power consumption of Pi cells to be much higher than TN cells. The second drawback of Pi cells is their lower contrast. When a Pi cell is in its dark state (high voltage on terminals), it leaks more light than a comparable TN cell. In a communication link, this light leakage results in a constant bias voltage in the receiver, causing saturation and reducing the SNR.

Although Pi cells are not very power efficient, they are still a possible choice in a passive link thanks to their higher switching speed. In Chapters 4 and 5, we use these cells to build a passive link. As far as we know, these cells have never been properly analyzed and employed in passive VLC.

[4] In this context, *high frequency* refers to 2 kHz or more, as the LC cells normally operate within few Hz.

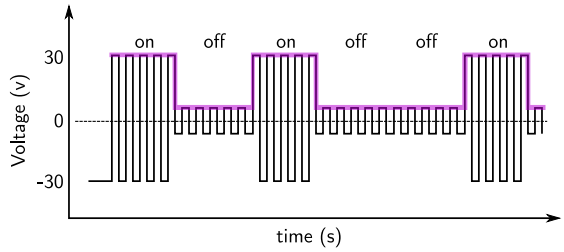


Figure 2.3: An example driving voltage of a Pi cell. The actual voltage is oscillating at 2 kHz (black line), whereas the 'on' and 'off' pattern of the Pi cell follows the envelope of this signal (pink line)

#### FERROELECTRIC LIQUID CRYSTAL (FLC) CELLS

FLCs are different from previous cells in their chemical composition, which is a liquid crystal in a *Chiral Smectic C phase* [38]. As a result, they are *bistable* [38], meaning that they can be either *on* or *off*, and not in any intermediate state unlike TN and Pi cells. These devices are not as prevalent as other crystal types, and are usually used in manufacturing high-resolution small displays [39]. These displays are made on Silicon substrates, therefore, they are not transparent. Consequently, the display has to work in reflective mode, where the light enters the crystal, becomes modulated, and is reflected towards the receiver, as shown in Figure 2.1c.

Due to their small form factor, complex modulation scheme, and difficult manufacturing, they are not a very suitable candidate when it comes to passive VLC. However, their application has been tried in one prior work [40], which will be introduced in Section 2.2.2.

## 2.2. RELATED WORK

The research questions posed in Chapter 1 cover a broad range from improving a link's properties (questions 1 and 2) to employing passive VLC in novel applications (question 3). To give structure to the thesis, we arrange the SoA in two main groups. **Group 1**, namely "SoA in physical layer", tackles the low-level, hardware aspects of a link: from increasing a link's data rate to the implementation of a Medium Access Control (MAC) layer. **Group 2**, called "SoA in novel applications", considers the adoption and integration of new LC-based applications, specifically LCD-to-camera communications. Each related work aims at improving one or several aspects of a passive VLC link, such as data rate, Bit Error Rate (BER), and range. However, there are other design choices affecting a link's performance. Therefore, we first mention some of these design choices in Section 2.2.1. Afterward, we describe the SoA related to **Groups 1** and **2** in Sections 2.2.2 and 2.2.3, respectively.

### 2.2.1. SOA EVALUATION ASPECTS

Each work differs in its design choices and improves particular areas. Besides data rate, BER, and range, which are common to all the SoA, we explain a few more dimensions by which these works can be compared.

1. **Transmitter's technology:** As mentioned in Section 2.1.1, there are various LC types that the SoA employ. In addition, DMDs have been explored in earlier papers. Expanding the definition of *transmitters*, there are also *static* tags used to convey messages in passive VLC. Although this last group might not qualify as a *real* transmitter, these tags have been used in the SoA for localization, data embedding, and making hidden *smart* surfaces.

2. **Receiver's bandwidth vs. spatial resolution:** This trade-off is a product of the different receiver's technology. As introduced in Section 1.1.3, photodiodes and analog color sensors have short response times, however, they usually have a low spatial resolution. On the other end, cameras have a lower speed while providing a high spatial resolution. Other devices, such as line sensors [41] and high-speed spectrometers, achieve an intermediate performance between speed and resolution. The choice of receiver affects a system's design requirements and methods. For instance, with cameras, Quick Response (QR) codes can be used instead of employing a single channel of '0's and '1's. Thanks to their higher spatial resolution, cameras can receive more information at once, compensating for their lower bandwidth, and hence, transferring more data.

3. **Transmitter's pixel count:** In some SoA studies, the transmitter only has one output surface for light, from which modulated light travels toward the receiver. We refer to this surface of light as a *pixel*. To increase the data rate, other works employ more than one pixel and place them side-by-side. These pixels can either be used to create parallel and independent data streams, or in the case of a single transmitter, increasing the number of communication symbols.

4. **Input-Output (I/O) configuration:** To have more data streams and a higher transmission rate, a study in the SoA, called RetroMUMIMO [27], implements multiple transmitters and receivers in parallel on the same channel. Using the RF terminology, we refer to this setup as Multiple-Input Multiple-Output (MIMO), where the *input* and *output* denote transmitters and receivers, respectively. A limitation of passive VLC is that most prior works implement SISO (SISO) links. It is important to emphasize that a multi-pixel link (as mentioned above) is not necessarily a MIMO one. For instance, some SoA studies use more pixels to create bigger constellations of communication symbols, while their system remains a SISO channel because it only works for a single transmitter and a single receiver.

In the next two sections, we summarize the advances of the most relevant prior works and their most notable design choices.

### 2.2.2. GROUP 1: SOA IN PHYSICAL LAYER

In this section, we iterate over the works relating to research questions 1 and 2, exploring the intricate physical properties of passive links.

#### RETRO-VLC

Retro-VLC [42] is a duplex SISO communication link. To make its *downlink*, an LED bulb is modulated to transmit messages towards a passive *tag*. The role of a tag is to form the

*uplink* by performing three functions: (1) receiving the signals from the LED bulb using a photodiode, (2) modulating the downlink's light once more to transmit its own data, and (3) send this modulated light back to the bulb to complete the uplink. Actions (2) and (3) are performed with the help of an LC cell mounted on a retroreflector– an optical surface that reflects the light back in its original incident direction, i.e. the bulb[5]. To complete the uplink, there is another photodiode at the bulb to receive signals from the tag. In both directions, light is modulated using ON-OFF Keying (OOK).

This work performs experiments in a dark, controlled environment, in addition to an office area. Based on their results for up to 1.5 m, the passive uplink has a Packet Loss Rate (PLR) below 3% in the dark room, and about 15% in their office experiments. The PLR of this system rises to more than 90% at 2.5 m. These results are obtained with their uplink working at 0.5 kbps.

This work takes its TN LC cell as is and does not tackle the disadvantage of its low bandwidth. Instead, they focus on designing a low power and batteryless tag by using solar panels to harvest the minimal energy needed. The reported power consumptions are 12 W for the active LED and 90 $\mu W$ for the passive tag.

#### PIXELATEDVLC

PixelatedVLC [43] tries to overcome the low switching speed of TN cells by increasing the number of communication symbols. It resorts to using a Pulse Amplitude Modulation (PAM) scheme, to make constellations of 4 and 8 symbols, which are distinguished by their amplitude. To achieve this scheme, it uses 2 cells (for 4-PAM) or 3 cells (for 8-PAM). Despite using multiple cells, the system still has a SISO configuration, as the cells do not operate independently.

This work does not report the BER of its prototype, however, it uses the BER equation to calculate the minimum SNR required to obtain a BER of 0.1%. This paper reports a bit rate of 600 bits per second (bps) at a distance of 2 m. The modulators they use have a switching speed of 200 bps, thus speed-up factors of 2× and 3× are obtained by using 4-PAM and 8-PAM, respectively.

Similar to Retro-VLC [42], the PixelatedVLC [43] tag includes a retroreflector and an energy harvester. The power consumption of the transmitter's tag is dominated by the microcontroller, which is about 200$\mu W$. PixelatedVLC [43] is a valuable contribution in addressing the low switching speed of LC cells in passive VLC, however, it does not provide a thorough practical evaluation and relies mostly on theoretical calculations.

#### PASSIVEVLC

PassiveVLC [33] uses the same platform as Retro-VLC [42], however, it introduces a novel (de)modulation scheme to allow for shorter communication symbols. As explained in Section 2.1, when a falling voltage is applied to the LC cells, they take a long time to reach their steady state. During this transition period, the cell shows a monotonic change in its opacity. Building upon this fact, PassiveVLC [33] implements *trend-based* modulation, where a symbol ('0' or '1') is represented by the slope of the LC's transmitted light. In contrast to OOK, this novel modulation allows for shorter switching times, enabling data rates that are 4 times faster.

[5]These surfaces are used in other papers as well, as they remove the difficulties of alignment in optical links.

*Trend-based* (de)modulation operates the LCs in their transient region and creates dependencies between consecutive bits. This problem is tackled by applying *Miller* encoding to the transmitted data, which allows the receiver to apply specific rules during the decoding process to recover unstable bits.



This system's uplink achieves 1 kbps with a PLR of 0% at a distance of 1 m. At this rate, it consumes a maximum of 152 $\mu W$. The significance of PassiveVLC [33] is that, to our knowledge, it is the first work to implement a successful link taking advantage of the *transient behavior* of LC cells. In Chapter 3, we will show that this transient region can open up potentials of speeding up the LCs as transmitters.

### LUXLINK

While a majority of the SoA focus on data rate, LuxLink [44] is the pioneer of improving three other properties of an LC-based link: (1) a lower visible flicker, (2) resiliency to ambient light change, and (3) a long transmitting distance. LuxLink modulates the light amplitude radiated by LC cells using Frequency Shift Keying (FSK) [6]. The platform chooses frequencies above human perception to eliminate the visible flicker of LCs. Furthermore, since the platform does not modulate in baseband, the system is less affected by ambient light variation, resulting in a more robust communication link.

These advantages come at the cost of the data rate. LuxLink [44] reports a data rate of 80 bps at a distance of 60 meters using natural sunlight, with a Packet Success Rate (PSR) of about 75%. The PSR gets closer to 100% at a distance of 50 meters. The authors report the power consumption in two parts: one for the circuitry of the transmitter, which is $23.8 mW$, and the other for the LCs alone, which amounts to $0.3 mW$.

In LuxLink, the LCs are modulated in their transient region, and they never reach their steady state. This paper is the main inspiration for the work in Chapter 3 of this thesis, where we show how an intrinsic characteristic of LCs helps to increase the low data rate reported by LuxLink [44].

### RETROI2V

RetroI2V [32] focuses on a long-range and flicker-free communication and showcases a real application. In their design, road signs are equipped with LC cells to backscatter useful data to a car's headlight. The configuration of their link is similar to PassiveVLC [33]. A car's headlamp is modulated to send data to a road sign, forming the downlink. Then, the LCs and retroreflectors placed on the road signs modulate the incoming light to transmit in the uplink, i.e. from the road sign to the car. Both the car and the road sign are equipped with photodiodes to decode data.

A unique feature of this work is that transmissions take advantage of two orthogonal channels to implement *differential modulation*. This novel approach is implemented by using two sets of LCs with perpendicular polarities and a synchronized modulation scheme, which is called Polarization-based Differential Reception (PDR). This approach is meant to increase the SNR, and not the data rate, since the two orthogonal channels transmit the same data, but in opposite polarities. This work also implements a MAC protocol to service multiple users (cars) simultaneously.

[6] It does not modulate light wavelengths, only the amplitude.

RetroI2V [32] employs 36 LCs and achieves a BER of less than 1% at a rate of 1 kbps and a distance of 80 meters. Despite employing many transmitting LCs, the link still falls in the category of SISO due to the (de)modulation type and dependency of the channels.

The authors report that the headlight's power consumption is set to a maximum of 30 W, however, the power for the LCs is not reported. Instead, using a link budget model, they calculate the energy consumption per bit to be a maximum of 19.19$\mu J$ per bit at a data rate of 1 kbps.



#### RETROTURBO

RetroTurbo [34] makes a significant improvement in data rate compared to all prior studies. This notable contribution is achieved by employing two concepts: (1) Delayed Superimposed Modulation (DSM) to account for the long falling time of LCs, and (2) Quadrature Amplitude Modulation (QAM) in the polarization domain, dubbed Polarized QAM (PQAM). In their implementation, they use an array of 64 cells. With DSM, when one cell is taking a long time to turn off, another cell is quickly turned on to make various patterns in light's intensity. Therefore, the long falling time of cells are used to generate a constellation of symbols, increasing the data rate. To implement PQAM, LC cells are divided in two groups with two different polarizer directions. These polarizations are chosen to form an orthogonal basis, i.e. the I and Q equivalents of RF. The orthogonal basis allow creating another constellation on top of DSM, increasing the data rate.

RetroTurbo [34] reaches an experimental data rate of 8 kbps, with a BER of 1% at a distance of about 8 meters. Given the complexity of the modulation scheme, they use an array of 64 LC cells. Despite this large number of transmitters, this link is still considered a SISO system, as all the cells are co-dependent and do not make parallel channels. Regarding the power consumption, the authors report that the LC cells consume a total of 800 $\mu W$ when the link works at a data rate of 8 kbps.

As a result of its advanced design and implementation, RetroTurbo [34] has achieved the highest data rate among the LC-based systems of its kind. In Chapter 5, we move towards similar data rates while proposing a less complex system.

#### RETROMUMIMO

RetroMUMIMO [27] is the first work prototyping a low-latency MIMO system. As a requirement in such MIMO link, a receiver must be able to separate data streams sent by different transmitters on the same medium. To achieve this, the authors exploit several features unique to each LC cell: (1) (dis)charging patterns, (2) positional variations, and (3) polarization differences. Feature (1) captures the fact that different LCs (even of the same type) have sufficiently different discharging curves. Feature (2) considers the difference between the response of two LC cells as a result of their different viewing angle and distance to the receiver. Finally, feature (3) shows that different LC responses can be obtained by orienting the transmitters in either 0 or 90 degrees. Additionally, this work designs a low-latency MAC protocol to manage the communication between different cells.

The experiments are done using a maximum of 8 concurrent transmitting tags. With a BER limit of 1%, a distance of 2.5 can be achieved with 8 tags transmitting at 500 bps. By reducing the number of tags to 4 (thus enabling a lower number of concurrent channels), the link can achieve a distance of 3.75 meters.

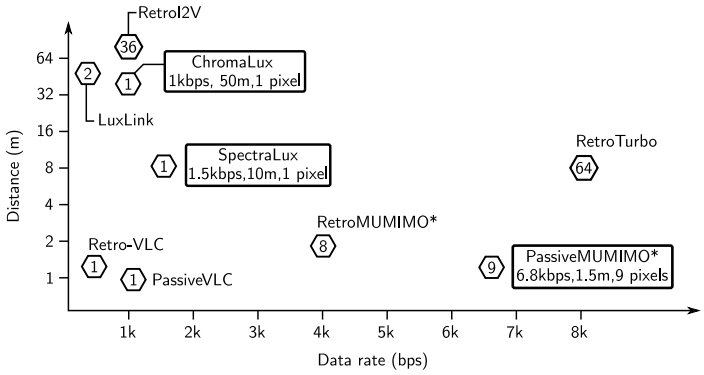


(a) Comparing absolute data rates.

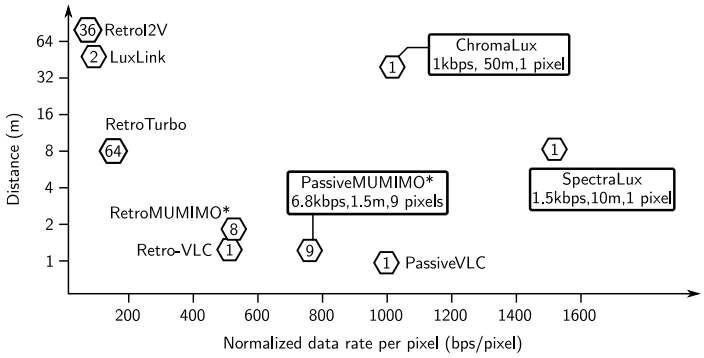


(b) Comparing normalized data rates by pixel count.

Figure 2.4: Summary of the SoA in physical layer. The only two MIMO works are marked with a star. The contributions of this thesis are also marked using a black border, with the number of pixels used by a transmitter in hexagons. (a) Measures the absolute data rate, (b) Shows the normalized data rate by the number of pixels.

RetroMUMIMO [27], despite being the first real MIMO platform, does not build upon reliable differences between LC cells, rather, it depends on random variations in their manufacturing process. In addition, the demodulation process uses a Singular Value Decomposition (SVD) method relying on numerous samples–43200 pulses–to extract pulse features. In Chapter 5, we propose another MIMO design taking advantage of polarization and color channels to achieve comparable results. Moreover, by building on a classical demodulation approach, the proposed method needs significantly fewer training samples.

### OTHER SOA

In the above section, we discussed the most relevant SoA to this thesis: links with LC-based transmitters and custom photosensitive receivers. In addition to this line of research, there are prior works implementing other technologies, as described in Section 2.2.1. For example, PIXEL [25] and POLI [23] use passive modulators to transmit data, however, they use a camera on the receiving end, instead of photodiodes or color

sensors.

In other application areas, there are platforms with transmitters other than LC cells. PassiveCom [45] reads custom *barcodes* on moving objects with a photosensor. PhotoLink [26] uses DMDs to modulate its incident light towards a photodiode. This work reports a data rate of 40 kbps at a distance of 2 meters. However, this system's power consumption has an upper bound of 50 mW, which is considerably higher than LC-based systems.

Finally, there are also platforms that do not transmit data *dynamically*. PolarTag [24] and RainbowLight [22] propose using static tags instead of a transmitter. They create invisible labels (using polarization variations) that can be retrieved by a camera behind a polarizer. RainbowLight [22] targets localization, and PolarTag [24] aims at hiding general purpose information in invisible matrices of tags.

#### BIG PICTURE OF THE RELATED WORK

As the main focus of this dissertation is on improving the hardware of LC-based transmitters, it is beneficial to show a big picture of where our contributions stand compared to the SoA. Figure 2.4 serves this purpose. There are two variations in this graph. Figure 2.4a shows the distance and data rate of prior works, as well as the contributions of this thesis. However, in some of those platforms, such as RetroTurbo [34], the pixel count is notably high, making for a complex system and requiring a larger surface area. Therefore, to make a more balanced comparison, we introduce Figure 2.4b, where the data rate is normalized by the number of pixels. From this new point-of-view, the works of this dissertation form the Pareto frontier of this figure.

### 2.2.3. GROUP 2: SOA IN NOVEL APPLICATIONS

As laid out in Chapter 1, our third research question is about the applications of passive VLC. For this research question, we consider passive LCDs, i.e. passive displays, which are transparent screens that take advantage of ambient light to display pictures. Nowadays, some of these novel displays, also known as smart windows [46], are being employed at large scale in buildings, airports, and other public places. Considering this new trend, an engaging application is to use smart windows as *passive transmitters* sending information to a user's phone in an unobtrusive manner, i.e. such that a viewer does not notice the transmission.

To our knowledge, Chapter 6 is the first to develop a passive screen-to-camera platform. However, our inspiration came from prior research on unobtrusive transmission in *active* screen-to-camera communications, since they consider encoding imperceptible data in videos as well. In the following sections, we present these inspirational studies.

#### INFRAME

The pioneering paper on embedding hidden data in a video is InFrame [47]. In this work, data is represented in *binary frames*. These frames are similar to QR codes: two-dimensional black-and-white patterns representing matrices of '0's and '1's. To hide the binary frames from a viewer, InFrame [47] takes advantage of the flicker fusion property of the eyes. Human eyes are in fact a *low-pass filter* of visual data, and if frames are played fast enough, a viewer perceives the average between two consecutive colors. To

implement this flicker-fusion approach, InFrame [47] embeds data in a complementary way: first, it duplicates each video frame, yielding $f^+$ and $f^-$. Then, based on the information embedded in the binary frame, it modulates a pixel $p$ in $f^+$, for instance, by increasing the luminance value of $p$ by $\Delta$. In the next step, it takes the pixel at the same location in $f^-$ and decreases its luminance by $\Delta$. This procedure results in pixels with values of $p+\Delta$ and $p-\Delta$. When these two pixels are played after one another, human eyes see the (original) average value of $p$.

InFrame [47] reports data rates from 5 to 7 kbps using real videos, and error rates from 9.5 to 20.9%. The authors also conduct user surveys to evaluate the flicker perception, where users report a relative reduction in flicker. To achieve the lowest flicker, they try to minimize the $\Delta$ value as to cause a minimal distortion to a video, however, they report that this method is not completely flicker-free. InFrame is followed by InFrame++ [48] to further reduce the amount of flicker.

#### INFRAME++

InFrame++ [48] addresses the remaining perceptible flicker issue in InFrame [47] and also increases the data rate. The prior work only explores the averaging property of the eyes in the time domain, i.e. a *temporal* flicker fusion. InFrame++ [48] states that there is a *spatial* fusion property as well–i.e. the human eye takes the average luminance of adjacent pixels[7]. To take advantage of this property, InFrame++ [48] implements a spatially complementary scheme, so that if a pixel's value is increased by $\Delta$, its adjacent pixels are decreased by the same amount.

Using both the temporal and the spatial properties at the same time, InFrame++ [48] reduces the flicker even further than its predecessor, as validated with a user survey. In addition to lowering flicker, the authors report a data rate of 150 to 240 kbps at a BER of 10 to 30%, depending on numerous configurations and encoding adjustments they use.

#### TEXTURECODE

TextureCode [49] advances prior work (mainly InFrame++ [48]) by analyzing the texture of videos. It builds on the premise that in parts of a video with a high *texture*, i.e. significant variation in pixel values, it is easier to hide modulations from a viewer's perspective. The authors employ texture analysis to find suitable regions in a video frame for data embedding.

Based on this novel approaches, the authors report that they can significantly reduce flickering. In addition, their results show a maximum data rate of 22 kbps with a BER below 15%.

#### CHROMACODE

Although TextureCode [49] improves the invisibility of the flickering effect, it sacrifices data rate, since it embeds data only in high-texture parts of a video. ChromaCode [50] builds upon the virtue of texture analysis to embed information not only in high-texture regions of a frame, but over the entire frame.

ChromaCode uses the perceptually uniform color space of CIELAB to predict the effect of changing luminance on human eyes. By using this color space, it modifies the

[7] An example of spatial flicker fusion is used in dithering by ink jet printers to give the illusion of colors other than basic R, G, and B

intensity domain $L^*$ of a pixel by $\Delta L^*$. In the next step, it scales down $\Delta L^*$ values in low-texture pixels. With these novel methods, the system beats its predecessors in data rate, BER, and invisibility. The authors report a raw throughput of more than 700 kbps and a goodput of 120 kbps with a BER of 5%. Thanks to its advancements over other SoA, we use this work as our stepping stone in Chapter 6 to develop an unobtrusive passive LCD transmitter.



### OTHER RELATED WORKS

Other papers explore different color spaces and domains to achieve invisibility in screen-to-camera communication. Deeplight [51] exclusively modifies the blue channel in the Blue Green Red (BGR) domain, as human eyes are less sensitive to blue light. It uses a Deep Neural Network (DNN) to decode the bits on the receiver side. Uber-In-Light [52] uses both blue and red channels to embed data, and modifies the green channel to compensate for the modulation on the other two color channels. AirCode [53] applies the same video encoding as ChromaCode [50], but utilizes an audio channel to embed and transmit metadata, which is less error-sensitive compared to the video channel.

Sunbox [40] is the first work to use an FLC-based micro-display to make a passive screen-to-camera link, which relies on sunlight to display images. The microdisplay presents a series of two-dimensional QR codes decoded in real-time by a smartphone camera. However, this platform is not designed to show any videos. Furthermore, the system requires placing the phone over a static holder and at a distance of just a few centimeters from the microdisplay. In Chapter 6, our system allows users to exploit considerably bigger window panels and there is no need to place the smartphone on static holders.

# 3

# ChromaLux

In Chapter 2, we mentioned the SoA that took valuable steps toward increasing data rate of LC-based passive links, however, they have been working under the assumption that LCs only provide a monotonic change in light intensity when they transition between their opaque and translucent states. That assumption has constrained the design space of researchers, limiting them to choose between using (i) the end states (opaque and translucent) to modulate light, providing high contrast but low bandwidth [25, 23], or (ii) intermediate points in the transient (monotonic) state, which provides a higher bandwidth but low contrast [33, 44].

Building upon the fundamental physical properties of LCs, we design single-pixel transmitters with a non-monotonic transient state. This non-monotonic property allows us to modulate light using symbols that have a high switching speed *and* good contrast. This key insight, depicted in Figure 3.1, allows us to increase the bandwidth of long-range links by an order of magnitude. Overall, our work, dubbed ChromaLux, makes the following contributions to the area of passive communication with visible light:

1. **Expose a yet unexploited transient state:** Based on the fundamental physical properties of LCs, we show that the modulation process does not need to be constrained to the simple monotonic function used in the state-of-the-art. By placing multiple cells in series, we uncover a broader modulation spectrum that contains a transient state with multiple peaks and valleys. The extremes in this transient state provide high contrast and fast switching, which we exploit to increase the channel capacity.

2. **Propose a constellation diagram for single-pixel transmitters:** Contrary to traditional VLC, where there is a well-established methodology to design LED transmitters, there is no theoretical framework for passive VLC. Based on first principles, we propose a constellation diagram to obtain foundational guidelines for the design of our single-pixel LC transmitter. Our framework allows us to theoretically substantiate the need (i) to use an optimal number of LCs to maximize the channel's performance and (ii) to use symbols on a particular region of the transient state.

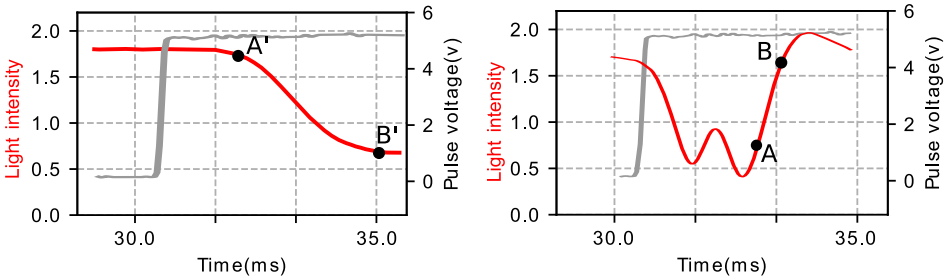


(a) State of the art

(b) ChromaLux

Figure 3.1: Key Insight: Existing studies assume that the transition between the end-states of liquid crystals is monotonic, which leads to symbols that have a high contrast, but a low bandwidth (like A' and B'), or the opposite trade-off. Based on first principles, ChromaLux exposes a transient state where symbols can have a high contrast *and* bandwidth (like A and B).

3. **Design a novel modulation scheme:** The transient state allows exploiting symbols with high contrast and switching speed, but it is unstable and standard modulation techniques based on amplitude, frequency or phase shift keying cannot be implemented. To enable a stable wireless link, we propose a novel duty-cycling method to modulate bits based on a 3-level voltage input.

4. **Evaluate our platform with artificial and natural ambient light:** We built a proof-of-concept platform and tested it with both artificial and natural ambient light. Our results show that we can achieve a 50-meter range with low sunlight conditions (3-6 klux) with a data rate of 1 kbps and a BER below 1%. Compared to other studies, we increased the range by a factor of 20 and the transmission speed by a factor of 10. More importantly, to showcase the general validity of our approach, we evaluate two different liquid crystals and demonstrate that both increase their bandwidth by an order of magnitude.

## 3.1. BACK TO THE BASICS

To squeeze the best performance (data rate, BER, range) out of readily available LC shutters, it is important to have a good understanding of the underlying physics.

### 3.1.1. AN OVERLOOKED FEATURE: BIREFRINGENCE

In Chapter 2, we provided an general description of how different types of LCs work. To scratch the surface, we need to go deeper than the simple abstraction of regarding an LC cell as a light switch. In this chapter, we focus on the role of changes in birefringence, an important LC property that has not been considered thus far for backscatter communication.

#### REFRACTION AND BIREFRINGENCE

The changes between translucent and opaque states is well-studied in backscatter communication, but the fact that these changes are related to birefringence has been largely

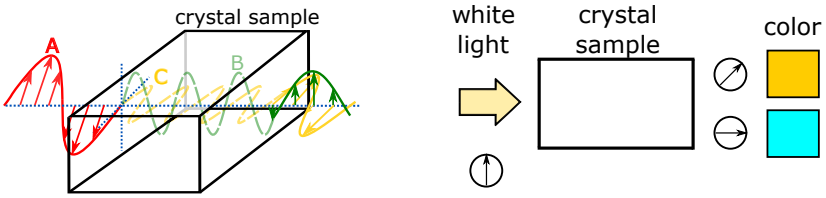


(a) Single frequency light

(b) White light

Figure 3.2: The effect of birefringence on crystals



overlooked, limiting the potential of LCs.

In transparent materials, light travels slower than in free space. The ratio of this reduced speed with respect to $c$ is called the *refractive index (n)*. Some materials, such as most crystals, have different different indices $n$ for different polarization angles of light [54]. The highest and lowest values of $n$ are important because they allow calculating the refraction index for any polarization angle. These materials are called birefringent because of these two values. An example is presented in Figure 3.2a. Upon entering the material, a polarized light ray (A–red) is divided into two orthogonal components along the axes of maximum and minimum of $n$, each traveling at a different speed, one fast (B–green) and the other slow (C–yellow). The birefringence parameter, denoted as $\Delta$n, is the difference between the refractive index of the fastest and the slowest axis of the material: $\Delta n = n_{fast} - n_{slow}$. Due to the different changes in speed, the two rays leave the crystal with a different phase. If instead of assuming a single-frequency ray (color), we consider polarized white light (all colors), each color will end up with a different change in phase. The naked human eye perceives these out-of-phase signals as white light, but if we use an analyzer, as in Figure 3.2b ,we will see different colors depending on its orientation. For ChromaLux, the various changes in phase caused by birefringence are key because they allow for fast transitions with high contrast.

### 3.1.2. BIREFRINGENCE IN LIQUID CRYSTALS

Material scientists have developed numerous methods to study the properties of crystals. Consider a *solid* crystal that is sandwiched between two orthogonal polarizers. When white light enters this structure, only a certain color exits, depending on the birefringence $b$ and thickness $d$ of the crystal [55]. These colors are captured by the so-called Michel-Lévy chart, shown in Figure 3.3. In this chart, a radial line corresponds to the birefringence of a crystal and a horizontal line to its thickness (measured in nm). Thus, for a solid crystal, the color output is captured by the intersection of a radial and horizontal line.

What sets *liquid* crystals apart is that their birefringence changes with an external electric field. Every voltage within their operational range leads to a different birefringence value. In the Michel-Lévy chart, an LC cell is represented by two radial lines and a horizontal line (thickness). The two radial lines represent the max and min birefringence of the crystal, and there is an inverse non-linear relation between the applied voltage and the birefringence. When the voltage is decreasing, the birefringence increases covering

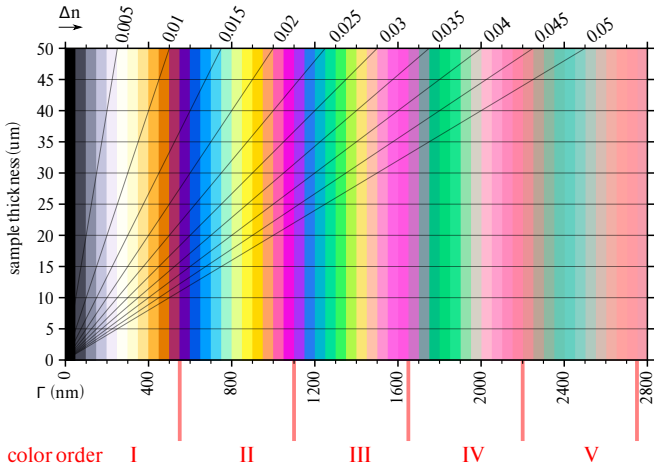


Figure 3.3: Michel-Levy chart [56]. The radial lines represent the birefringence values ($\Delta n$, numbers on the top), and the plot shows how the color (horizontal axis) varies with the width (vertical axis). By convention, each 550 nm of path difference is named *order* and ends with a shade of magenta.

all the spectrum within the two radial lines. That covered spectrum determines the LCs transient phase. For example, a crystal with a 25 $\mu m$ thickness and $\Delta n$'s of 0.005 and 0.015, would have a spectrum between gray and yellow.

PUTTING THE MICHEL-LÉVY CHART IN THE CONTEXT OF BACKSCATTER COMMUNICATION. The birefringence and thickness of typical LC shutters are chosen to cover only a narrow high-contrast region between a dark and a light color in the Michel-Lévy chart, and several studies exploited that region to modulate information (discussed in Chapter 2). To the best of our knowledge, no research prior to ChromaLux has connected the fundamental physical properties of LCs with backscatter communication. To formulate a theoretical framework, we build upon the equation used to create the Michel-Lévy chart, which expresses the fraction of light $L$ that leaves the analyzer for incoming light with wavelength $\lambda$:

$$L(\Gamma, \lambda) = sin^2(\frac{180° \times \Gamma}{\lambda}) \tag{3.1}$$

where Gamma ($\Gamma$) is known as the *path difference*, which combines the main properties of the crystal, birefringence ($\Delta n$) and thickness ($d$), on a single parameter.

$$\Gamma = \Delta n \times d \tag{3.2}$$

By summing over all frequencies in the visible light spectrum, one can obtain the resulting color coming out of the analyzer.

It is important to note that this equation only captures the most common LC configuration, where the angle between the polarizer and analyzer is 90°. For details on the more general equation, please refer to [57].

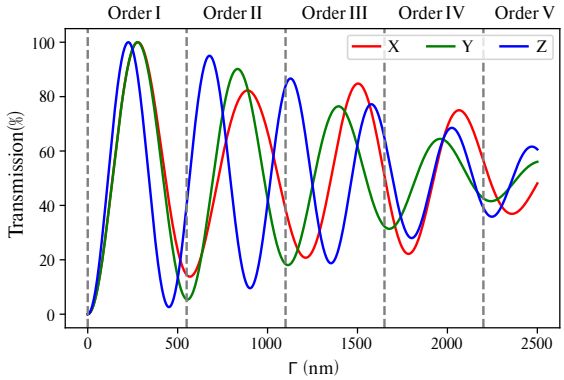


Figure 3.4: Theoretical color response of a liquid crystal.



COLOR SENSORS AND THE THEORETICAL RESPONSE OF LIQUID CRYSTALS.

ChromaLux's approach requires decomposing light into its color components. For this task, we utilize color sensors, which are simple single-pixel receivers. They can be seen as photodiodes with inexpensive color filters in front of them. There are multiple types of color sensors, and we decided to use a type called *true color* sensor because it mimics the human perception of color. The reason for that choice is that the Michel-Lévy chart is also designed to capture people's perception of colors, and hence, our sensor (empirical experiments) will be in agreement with the theoretical results (Equation 3.1). When referring to the output of a true-color sensor, we will follow the convention of using (X,Y,Z) coordinates, which are a transformation of the well-known (R,G,B) space.

Decomposing light into different color channels allows us to have a deeper look into the Michel-Lévy chart. Using Equation 3.1, we show a sample theoretical response in Figure 3.4, where the path difference ($\Gamma$) of a crystal gradually increases. To construct this plot, we generated ($\Gamma$, $\lambda$) tuples using Equation 3.1. $\Gamma$ values were selected from 0 to 2500 nm, and $\lambda$ values were selected from the visible light spectrum. Then, the amplitudes of wavelengths in the output light were converted to (X, Y, Z) values [57]. Initially, all channels start with zero intensity (black), then the channels increase their values in a rather synchronized manner up to the first peak (white). After that, the channels get out-of-phase, leading to the range of colors observed in the Michel-Lévy chart.

Note that the theoretical response is time-independent; it is a function of Gamma ($\Gamma$), which in turn is a function of the birefringence (Equation 3.2). In practice, we have to take into account the time-dependent characteristics of LC cells. Next, we analyze The empirical response of LCs and their ability to increase the bandwidth of the system.

## 3.2. SPECTRUM ANALYSIS

Based on the prior section, we know that LCs can be designed to oscillate between any two colors in the Michel-Levy chart. A designer only needs to select the appropriate birefringence values (radial lines) and thickness (horizontal line) for the liquid crystal layer. We designed a simple setup using a flashlight and a color sensor to measure the spec-

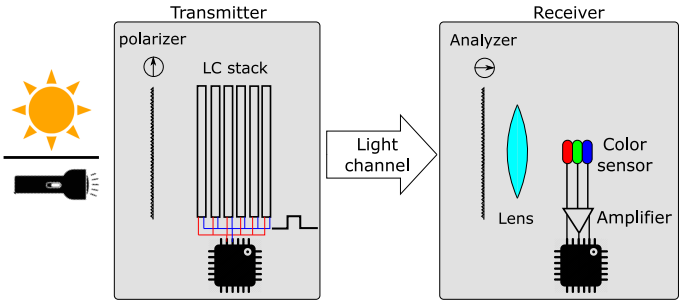


Figure 3.5: Setup to measure the color spectrum

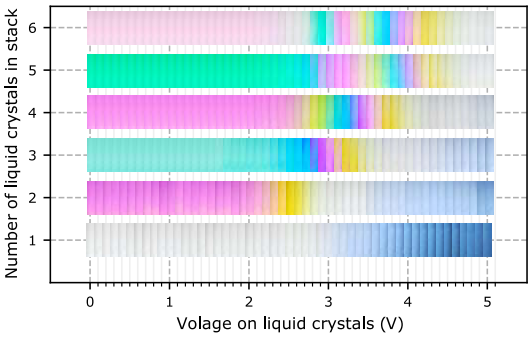


Figure 3.6: Color spectrum for different number of cells.

trum of single and multiple LC cells. The cells were placed in series between a polarizer and an analyzer with orthogonal directions, as shown in Figure 3.5, and different voltage levels were applied. It is important to highlight that off-the-shelf LCs available in the market do not provide data sheets with detailed optical characteristics, but a deep understanding of those characteristics is fundamental to define a complete design space.

The derivation of our framework (Section 3.2-3.4) focuses on a popular Twisted-Nematic crystal used for 3D glasses that has been explored in previous backscattering studies [58], but to demonstrate the generality of our approach, we also utilize our framework to improve the performance of a different LC shutter in Section 3.6.

### 3.2.1. THE SINGLE-CELL CASE

To see the color spectrum of an LC stack, we place from one to six cells between a polarizer and an analyzer and change the DC voltage on the stack. We sweep the DC voltage in steps of 0.1 volts and take pictures of the output light at each step to get Figure 3.6. The bottom row of that figure depicts the color spectrum for a single cell when different *static* DC voltage levels are applied. As expected, the spectrum covers the dark to white transition in the first order region of the Michel-Levy chart. *The important observation from this result is that while most backscattering studies exploited this spectrum, they overlooked the fact that this transition is due to the change in the cell's birefringence*

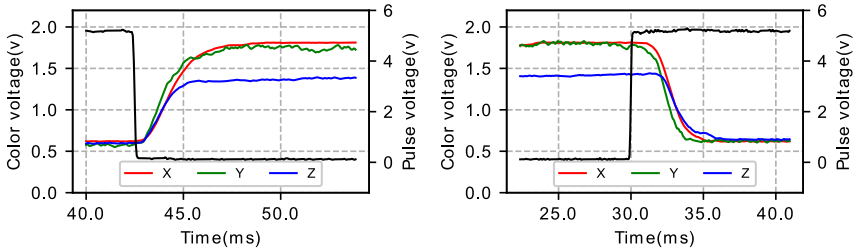


(a) Falling pulse

(b) Rising pulse

Figure 3.7: Transition state for a single cell.

*value*. If, instead of using *static* voltage values, we use *dynamic* voltage pulses, we obtain the time response of the cell. Figure 3.7 shows the time response of a single cell when we apply falling and rising pulses between 0 and 5 V. The fact that the three channels are in phase, and have the same intensities[1], is what causes the monotonic change in the spectrum. Given that the most popular application of LC cells is as light shutters, it makes sense to design cells whose only purpose is to oscillate between the translucent (white) and opaque (dark) states.

This monotonic behaviour has been exploited for backscatter communication in two main ways: (i) by using the end values in the steady states to encode data [25, 23], which maximizes the contrast (SNR) but at the cost of reducing the switching speed (bandwidth); or (ii) by using intermediate values, which has the opposite trade-off, lower contrast but higher switching speeds [33, 44].

The important take-away is that, to obtain that monotonically decreasing behaviour in the black/gray/white scale, manufacturers produce crystals with birefringence values and thicknesses that only cover a *very specific and narrow* portion of the theoretical response in Figure 3.4: the Gamma range between 0 and 250.

### 3.2.2. THE MULTI-CELL CASE

*To increase the modulation spectrum of an LC, we need to increase its thickness or use a broader range of birefringence values.* Unfortunately, the thickness and birefringence values of liquid crystals are fixed and determined during the manufacturing process. To expand the modulation spectrum, we stack multiple cells to increase the thickness of the crystal layer. In the Michel-Levy spectrum, our approach translates to using a higher horizontal line while maintaining the same radial lines.

The top five rows of Figure 3.6 depict the spectrum obtained with static voltages after stacking multiple cells. Since we are increasing the thickness, the color spectrum shifts to the right of the Michel-Levy chart. For example, the configuration with two LCs covers most of the first order, and the configuration with six LCs covers from the middle of the

[1] It is important to recall that the XYZ space has different ranges for each channel. For example, in the RGB space the range is the same for all channels [0,255], which means that white light is represented with all channels having the same values (255, 255, 255); but white light in the XYZ space is represented with non-homogeneous levels: (0.9642, 1.0000, 0.8252).

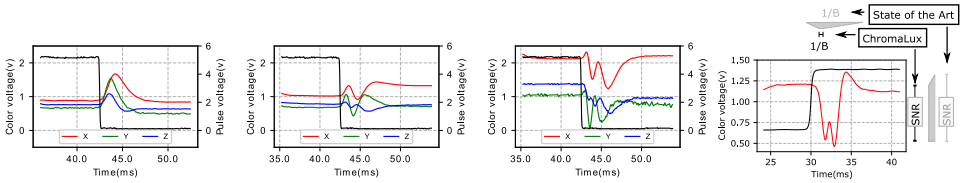


(a) 2 LCs (b) 4 LCs (c) 6 LCs (d) Capacity analysis.

Figure 3.8: Time responses for multiple LCs in series & capacity analysis.



first order until the third order. Note that at low voltages (below 2 V) there are no color transitions. This occurs because the minimum operating voltage of our cells is around 1.4 V. Below that voltage, the cell does not change its state. That minimum voltage is known as the Fréedericksz threshold [59].

Next, we will see why transient states with frequent color transitions are beneficial for ChromaLux. Figure 3.8 depicts the time response for falling pulses when we stack 2, 4, and 6 cells. We focus on the falling pulses because they are known to be the main bottleneck in backscatter communication, referring to Chapter 2. These time responses provide two important insights.

*First*, the increased spectrum exposes a non-monotonic *transient state* with considerable levels of contrast. When we increase the thickness of the crystal layer, we cover a wider range of Gamma values. For example, with two cells, we cover an approximate Gamma range of [150, 500], and with six cells, the range is around [300, 1500]. The numerous peaks and valleys present in the transient state imply that, in the multi-cell case, two nearby points can provide a much higher contrast (SNR) compared to the *same* two nearby points in the single-cell case.

*Second*, the duration of the transient state remains the same for any number of cells. Note that the period of the transient states in Figure 3.7 and Figure 3.8 is around 5 ms for all cases. It would not be helpful if the transient state exposed peaks and valleys at the cost of an increased transition period. Even though the morphology of the transient state changes with a different number of cells, *its period remains the same.* This occurs because we control the LCs in parallel. In principle, the thicker the cell, the longer the time required to switch between states. Thus, in terms of switching speed, it is better to increase the thickness by using $n$ cells (each with thickness $w$), instead of using a single (slower) cell with thickness $n \times w$.

***Key insight***: Increasing the thickness of the transmitter by stacking cells exposes a transient state where we can achieve a high switching speed between nearby points at a higher contrast compared to a single cell with the same modulation points.

### 3.2.3. ANALYZING THE CHANNEL'S CAPACITY

A fundamental goal for any wireless communication system is to increase its capacity. With LCs, the channel capacity is determined by their contrast and switching speed, but maximizing these two parameters represents opposing design goals. Thus, a crucial question is: if one has to choose, what is preferable in an LC, higher contrast or faster speed? Having a deep understanding of this trade-off is key to maximize the capacity of

ambient-light links.

We use the well-known Shannon–Hartley theorem to anchor our discussion, $C = B * \log_2(1+SNR)$. As shown in Figure 3.7, existing LCs are designed to maximize contrast (SNR) by covering the lowest valley (black) and the highest peak (white) in the theoretical response. This focus on contrast (SNR) as opposed to switching speed (B) makes sense for human-centric applications because human eyes have a slow frequency response. For wireless communication, however, preference must be given to the switching speed (B) because it increases the capacity linearly while the contrast (SNR) only gives a logarithmic improvement. Due to this reason, our focus will be on increasing the bandwidth of ChromaLux. As shown in Figure 3.8d, the key idea of ChromaLux is to trade a bit of SNR (using a single cell as the baseline) for a major gain in bandwidth.



## 3.3. A PRETZEL CONSTELLATION

As described in the prior section, adding LCs brings together more peaks and valleys within the transient state, which increases the bandwidth because the period between consecutive extremes is reduced. Thus, one may think that stacking as many LCs as possible would be the best approach to increase the bandwidth. But that is not the case. To understand the constraints of the transient state, we will first describe the differences between an ideal and a practical transmitter, and then propose a constellation to guide the selection of the number of cells and symbols.

*An ideal transmitter.* In theory, an ideal transmitter consisting of multiple LCs would cover a Gamma range from close-to-zero to a high value. The close-to-zero birefringence value (equivalent to an almost vertical radial line in the Michel Levy chart) would mean that the transient state includes the first valley and peak in the theoretical response, which provides the highest contrast (similar to using a single cell). The high birefringence value would allow us to compress multiple peaks and valleys inside the transient phase, reducing the switching speed amongst symbols (high bandwidth).

*A practical transmitter.* In practice, the minimum birefringence value in off-the-shelf cells is too high to include the first valley of the theoretical response once multiple cells are stacked, cf. Figure 3.6. Adding cells is beneficial, but for every cell we add, the spectrum moves further into the right side of the theoretical response (Figure 3.4), where the contrast of the signals decreases. In the next subsections, we provide a theoretical framework to guide the selection of (i) the number of cells that optimizes the morphology of the transient state, and (ii) the best region within the transient state to place our symbols.

### 3.3.1. OPTICAL DOMAIN

For traditional RF and VLC systems, there are established methods to design the symbol space. The most common approach is to use constellation diagrams that are independent of time. In order to create a time-independent constellation that connects theory with practice for ChromaLux, we plot the Z versus X channels for (i) the theoretical response, where the channels are a function of Gamma, and (ii) the empirical time responses, where the channels are a function of time[2].

[2] Note that in principle, the constellation should be a 3D space covering the XYZ dimensions, but that is hard to visualize. The XYZ color space has the nice property of projecting most colors onto the 2-D space captured

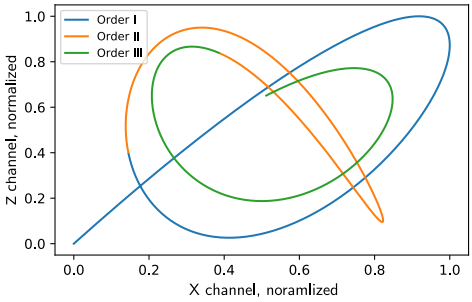


Figure 3.9: Theoretical constellation

The theoretical constellation is depicted in Figure 3.9, which looks like a pretzel. This graph is obtained by plotting the (X, Z)-pairs of the data underlying Figure 3.4. Within a constellation, the aim is to place symbols as far apart as possible from each other to maximize the signal-to-interference-plus-noise-ratio (SINR). However, contrary to the standard constellations used for RF or VLC, where symbols can be placed anywhere, we can *only* place symbols over the depicted curve. The constellation presented in Figure 3.9 is theoretical and *complete* up to the third order (plotting further orders would continue the trend inwards). In practice, ChromaLux will only see a subset of the constellation depending on how many cells we use. Figure 3.10 presents the partial constellation views obtained with 1 and 3 cells for falling and rising pulses. The rising pulses move in a counter-clockwise direction, and the falling pulses in a clockwise manner. Each one of these plots covers a subsection of the theoretical constellation, starting from the first order.

Our theoretical and empirical constellations provide an important design guideline regarding the number of cells that should be used. Adding too many cells pushes the constellation domain inwards, which would lead to tightly coupled symbols (low SINR). While adding cells, the designer should try to remain in the lowest possible order (most outward) to maintain a high SINR. In ChromaLux, we aim for the first intensity peak ($\Gamma$=250nm, see Figure 3.4) to be within the spectrum of our LC cell stack. By stacking cells, we move away from the first valley (black); hence, we should not miss the first peak (white) because that provides the second highest contrast in the theoretical response. In the next section, we will see that six cells is the optimal number for the type of LC we consider.

### 3.3.2. TIME DOMAIN

In traditional constellations, the amount of time required to move between any pair of symbols is the same. That is not the case for LCs. The ChromaLux constellation has two important differences. First, the time to move between points changes depending on the chosen pair. For example, moving between symbols at the edges of the transient state –the "start" and "end" points of the constellations in Figure 3.10– can be one order of magnitude longer than moving between symbols in consecutive extremes. Second,

by the X and Z channels. The Y channel is called the luminosity.

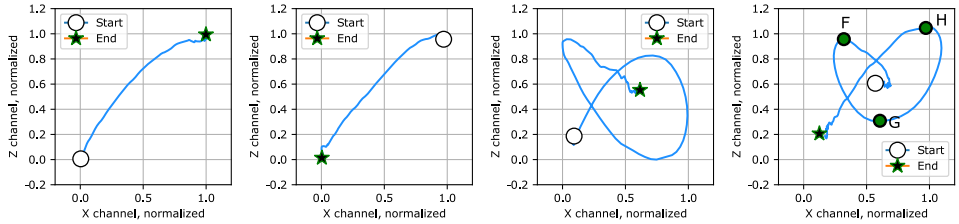


(a) 1 LC: Falling pulse (b) 1 LC: Rising pulse (c) 3 LC: Falling pulse (d) 3 LC: Rising pulse

Figure 3.10: Constellation diagrams for multiple LCs.

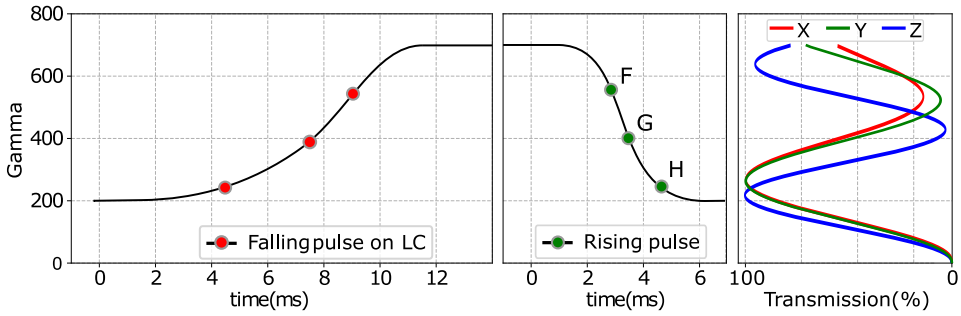


Figure 3.11: Gamma versus time

the direction of movement matters. Moving during a falling pulse is slower than moving on the opposite direction (rising pulse).

It is important to recall that LCs behave almost like capacitors. Discharging a capacitor follows an exponential decay in time ($e^{-t}$) and its charging follows a ($1-e^{-t}$) trend. To connect these equations with our constellation, let us define three symbols in Figure 3.10d and their (approximate) counterparts in Figure 3.9. The symbols in the empirical constellation can be mapped to time and the symbols in the theoretical constellation can be mapped to Gamma values. If we plot the Gamma versus time curves of those symbols, we obtain Figure 3.11. This plot shows that, from a bandwidth perspective, not all symbols are born equal in our constellation. Due to the exponential trends, the symbols that appear at the beginning of a pulse are preferred because they are more compact in time, but there is an undesirable trade-off: the slow symbols appearing at the tail of the falling pulse are the fastest symbols in the rising pulse and vice-versa. In the next section, we will analyze this trade-off further to select our final symbols.

The unique temporal properties of our constellation provide an important design guideline for the following scenario: If the system needs to transmit multiple symbols (4, 8, or more), is it better to use a single-pixel transmitter transmitting all symbols? or, a set of multi-pixel transmitters, with each pixel transmitting a pair of symbols? The answer is that it is better to implement a multi-pixel transmitter with two symbols per pixel. This is because a single-pixel transmitter has a key drawback: the bandwidth can be reduced significantly if multiple symbols are transmitted because the time taken to

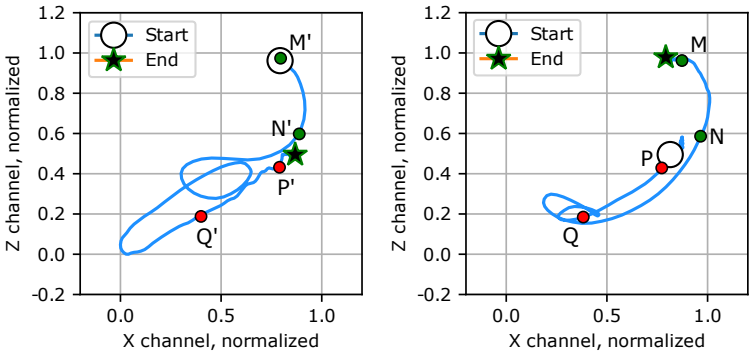


(a) 6 LCs: Falling pulse

(b) 6 LCs: Rising pulse

Figure 3.12: Constellations for six LCs

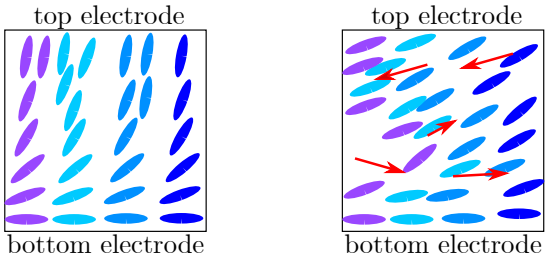


(a) Undistorted state

(b) Distorted state

Figure 3.13: The cross-section of an LC cell showing the backflow effect. The colors of the molecules are used to highlight their distorted displacement in the transient region, and the red arrows show the liquid flow directions. A more fine-grained analysis is presented in [60].

switch between different symbols at the extremities can be too long. For example, for the falling pulse in Figure 3.11, the time difference between symbols F and H is much longer than between symbols F and G. If we use a multi-pixel transmitter, each pixel can transmit one pair of *nearby* symbols, thereby increasing the system's bandwidth.

Given that our analysis in Section 3.2.3 shows that increasing bandwidth is more relevant than increasing the number of symbols, our focus will be on designing a fast single-pixel transmitter modulating two symbols.

## 3.4. COMMUNICATION SYSTEM

The idea behind faster modulation relies on the fact that by stacking liquid crystals, we can get a distinguishable contrast between on/off states without waiting for full transitions. In this section, we describe the approach we take to define the number of LCs, the symbols, and the modulation method.

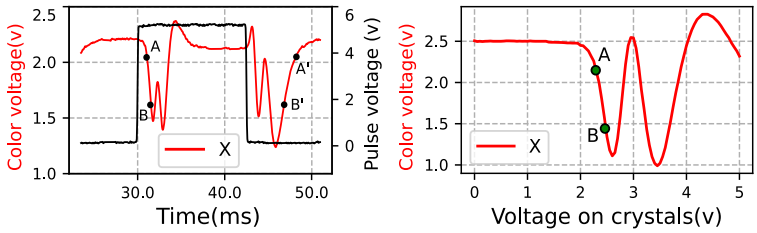


(a) Dynamic pulses.

(b) DC voltage

Figure 3.14: Communication symbols



### 3.4.1. NUMBER OF CELLS AND SYMBOL SELECTION

Selecting the right number of cells is a delicate balance between increasing the spectrum of the transient state and decreasing the contrast. As most of the LC cells available on the market lack important optical and electrical specifications, we first mention how to select symbols empirically and then theoretically in case the specifications are known.

*Empirical method.* In order to maximize the contrast, an important extremum to capture is the highest peak (white) in Figure 3.4, given that using multiple cells excludes the lowest valley. Figure 3.6 shows that using six cells allows us to achieve that balance. The spectrum starts around the white peak and continues to cover several orders. To select the best pair of symbols for this spectrum, we use the constellations shown in Figure 3.12. Notice that, for six cells, the empirical constellation is a highly distorted version of the theoretical one. Those major distortions start to appear when using four or more cells of this particular type. Note that when we use three cells, cf. Figure 3.10, the theoretical and empirical constellations have a closer resemblance. We hypothesize that this distortion is due to the "backflow effect" of liquid crystals [60]. When an electric field is applied, the LC molecules do *not* re-align in an orderly manner, as shown in Figure 3.13a. In fact, the electric field creates a temporary internal flow, similar to swirl, as depicted in Figure 3.13b. The more LC cells we use, the more visible this effect becomes due to the compounding effect of multiple backflows occurring in parallel.

The backflow effect is a transient phenomenon that dissipates close to the end states. Hence, the beginning and end of the constellations show a stronger symmetry, which is desirable for modulation. In Figure 3.12, those symmetric regions are present between points P/P'– Q/Q' and N/N' – M/M'. We decide to use symbols P/P' and Q/Q' because they provide a slightly better SINR. Each symbol maps to an (X,Y,Z) tuple in the time response in Figure 3.8c. We select channel X as our carrier, as there is not much difference between channels X and Y, and channel Z has a lower peak-to-valley difference. The final symbols A and B are shown in Figure 3.14a (channel X) on top of a sample rising and falling pulse.

*Theoretical method.* The approach presented in this paper is largely empirical because off-the-shelf LCs do not provide detailed optical and electrical parameters. A theoretical framework can be used to determine the system's symbols if the LC's datasheet specifies the following parameters: the cell's thickness $d$, the minimum and maximum birefringence values ($\Delta n_{min}$ and $\Delta n_{max}$), and the electric capacitance ($\mathscr{C}_e$). A theoretical

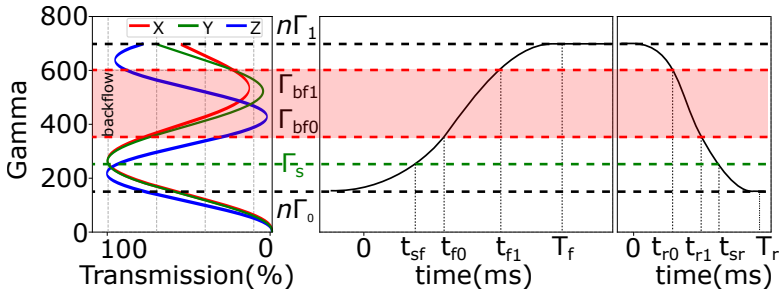


Figure 3.15: Theoretical Framework. The theoretical response (left plot) can be used to obtain the valid range of Gamma values, and the capacitance response (center and right plots) can be used to map the Gamma values to time values.



procedure consists of the following steps:

Step 1: Obtaining optimal number of cells ($n$). Following the path difference ($\Gamma$) defined in Equation 3.2 and denoting $\Gamma_0 = \Delta n_{min} \times d$ and $\Gamma_1 = \Delta n_{max} \times d$ in nm, the spectrum $[\Gamma_0, \Gamma_1]$ is covered by a single cell. If we stack $n$ cells, the new range of $\Gamma$ is $[n\Gamma_0, n\Gamma_1]$. The best value for $n$ is the highest number that still covers the first peak (because it provides the highest contrast). If $n$ grows beyond that value, we miss that important (white light) peak. A theoretical optimal range $[n\Gamma_0, n\Gamma_1]$ is depicted on the left side of Figure 3.15.

Step 2: Discarding the asymmetric backflow region. The range defined in Step 1 includes the distorted region caused by the backflow effect. To identify and avoid that region, methods such as those described in [60] can be used to simulate the rising (falling) pulse for time periods $t_r(t_f)$. That simulation would pinpoint the region where the distortions are so high that no symmetry is maintained in the constellation plots. The Gamma range capturing the undesirable backflow ($bf$) region $[\Gamma_{bf0}, \Gamma_{bf1}]$ is highlighted in red in Figure 3.15.

Step 3: Mapping Gamma values to time values. Until now, the theoretical framework has focused only on Gamma values (left plot in Figure 3.15). All these Gamma values can be mapped to time values using the time response defined by the electric capacitance $\mathscr{C}_e$ (center and right plots in Figure 3.15). For example, $\Gamma_s$, selected as our symbol, can be mapped to $t_{sf}$ and $t_{sr}$[3]. The experimental counterpart of the region between $\Gamma_{bf0}$ and $\Gamma_{bf1}$ is the line between Q and N (or Q' and N' equivalently) in Figure 3.12. Thus, we have to select symbols from the following set:

$$[n\Gamma_0\ ,\ \Gamma_{bf0}] \cup [\Gamma_{bf1}\ ,\ n\Gamma_1]$$

Due to the lack of specifications for our LC cells, we determined $t_{r1}$ and $t_{f0}$ empirically, using the pretzel graphs shown before. We will use this timing information in the next section to devise our modulation scheme.

[3] Note that the theoretical response and the time capacitance plots in Figure 3.15 are only dependants on the optical/electrical specifications of a single cell. Only the shift upwards in the theoretical response (left plot) depends on the number of cells.

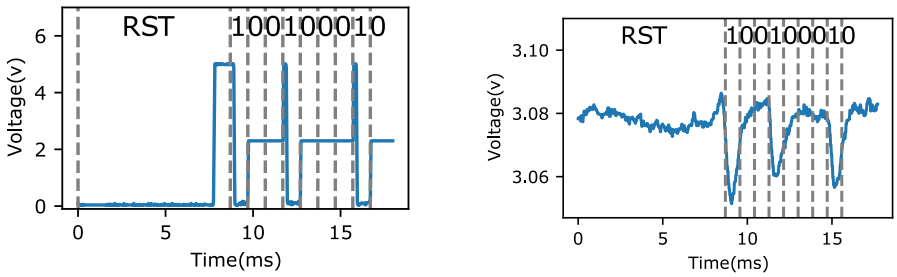


(a) Transmitted signal

(b) Received signal (channel X)

Figure 3.16: Sample signals at transmitter and receiver.



### 3.4.2. MODULATION

The unique properties of the transient state require a different modulation method compared to those found in the SoA. First, we will describe why existing methods based on two voltage levels do not work, and then, we present our three-voltage-level approach.

#### TWO VOLTAGE LEVELS.

The most common approach to modulate LCs is to map a voltage level to a symbol. Considering that the voltage controls the birefringence (and Gamma) values of LCs, one could use static DC voltage levels to keep the LC in state A or B. Figure 3.14b depicts the X channel values when we apply a DC voltage in steps of 0.1 from 0 to 5. This DC response is an undistorted, stable version of the dynamic rising and falling responses in Figure 3.14a. Symbols A and B are located at 2.2 V and 2.4 V, respectively. The problem of using a direct OOK modulation with those voltages is that the system would have slower transitions than when the voltage swing is 5 volts.

To overcome the slow (exponential) transitions between voltages, another option is to emulate the 2.2 V and 2.4 V via high-frequency pulses between 0 and 5 V. This broader voltage range provides faster transitions between the chosen symbols. An emulated DC value is equal to the maximum voltage (5 V) times the duty cycle of the pulse train. For our case, a 10 kHz signal would be sufficient to create the desired voltage levels. The drawback of this approach, compared to using the DC option, is that the high-frequency oscillations increase the noise level and power consumption.

#### THREE VOLTAGE LEVELS.

To combine the fast transitions of the [0,5] V range and the stability of DC voltages, we propose to use three voltage levels: 0, 2.2, and 5. A sample waveform of the transmitted and received signals are shown in Figure 3.16. To send bit 0, we use the 2.2 V to hold the LC in state A. The receiver will see bit 0 as a noisy 'flat' signal. To send bit 1, we generate the transition A-B-A by using a voltage sequence of 5-0. If these two voltages are kept for the proper duration, then the receiver will see bit 1 as a "V" shaped signal. The state machine of our transmitter is presented in Figure 3.17. Each state represents a tuple $(V, t)$, where $V$ denotes the voltage level and $t$ the amount of time spent in that state.

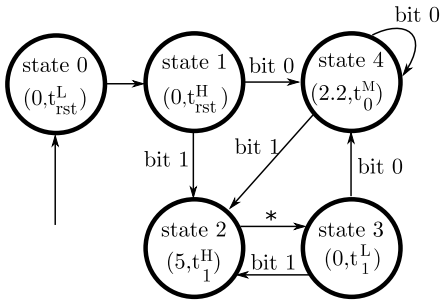


Figure 3.17: The state machine of the transmitter.

*State 0*: Considering that LCs (like capacitors) can have random charges stored on them when disconnected. At the start-up, we need to reset (RST) the voltage by keeping it at 0 for a period long enough to reach the steady-state: $t^L_{rst} = 8$ ms. This time has to be longer than $T_f$ shown in Figure 3.15.
*State 1*: The second part of the *reset* uses a 5 V signal for a period of $t^H_{rst}$= 0.9 ms. This duration can be measured from Figure 3.14a and represents the amount of time required to reach symbol A with a rising pulse. If we look at the theoretical graph in Figure 3.15, $t^H_{rst}$ is equal to $t_{sr}$, where the maximum of channel X occurs. At this point, the device can start transmitting bits.
*State 2*: If at the end of the reset state, the transmitter has to send a "1", a transition has to be made from point A to B. This transition represents the '\' part of the V shape seen in the receiver. A 5 V signal is applied for a duration of $t^H_1 = 0.2$ ms so the LCs can reach point B. In Figure 3.15, $t^H_1$ is equivalent to $T_r - t_{sr}$. After this period, the transition to State 3 is made automatically.
*State 3*: A 0 V is applied for the duration of $t^L_1 = 0.8$ ms. This duration is the time needed to get from B' to A', which is the '/' of the V shape for the symbol "1". In Figure 3.15, we have to apply a low pulse with the duration of $t_{sf}$. When the time for this step is up, the transmitter can send a new bit.
*State 4*: If the next bit to be sent is a 0, the only thing that the transmitter needs to do is to keep the LC at point A. To make this happen the middle voltage (2.2) is applied on the LC stack for a period $t^M_0 = 1$ ms.

### 3.4.3. DEMODULATION

To demodulate the received signal, we take the steps below. Our packet structure has a reset phase, a bit-1 for synchronization, and 84 bits of data after that.
*Step 1*: The receiver constantly measures the signal's mean and noise variance with a moving window of size 4 ms (equivalent to the length of four bits).
*Step 2*: If the variance changes by a factor of $X$ or more with respect to the noise variance measured during the idle period, the receiver enters a phase-lock phase.
*Step 3*: Given that the first bit after the reset phase is a "1", the receiver looks for the first minimum. This enables the receiver to lock onto the phase of the transmitter. After that, we start decoding data bits.
*Step 4*: If the variance of the received signal during a symbol period is lower than a

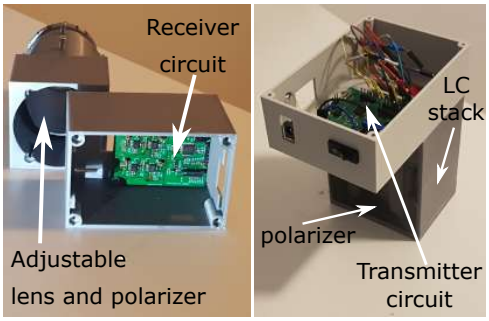


Figure 3.18: PCBs & enclosures: TX(left), RX(right)

threshold (determined by the noise floor of the LC, which is comparable to the channel noise), the symbol is demodulated as a "0". If the variance is higher than the threshold, we use the maximum and minimum values in the window to build a reference "V" shape, and a matched filter using Pearson correlation determines if the symbol is indeed a bit 1.

*Step 5*: Every time a symbol "1" is found in the incoming signal, the receiver's phase is corrected to account for small drifts and mismatch in symbol length, which are caused by the fact that LCs are operated in an unstable region. We cannot perform any such drift correction when a long series of "0" is received, but for the packet size we use (84 bits) no major synchronization issues surfaced.

## 3.5. PLATFORMS

We designed PCB and 3D-printed enclosures for the transmitter and receiver, both equipped with batteries.

### 3.5.1. TRANSMITTER

We use an STM32L031K6 microcontroller with four different voltage outputs. When using multiple cells, the output can act as a high capacitive load, which may render the circuit unstable. In our implementation, the maximum capacitance of the liquid crystal cells is 72 nF, which does not impose any problem. We use a basic op-amp (OPA2325) between the microcontroller output pins and the six commercial LC shutters. The transmitter's enclosure allows for both ambient and artificial light to be used. For artificial light, we use the flashlight of a smartphone, and for ambient light, a metal surface acts as a light reflector. We programmed the platform to send always the same packet: "HELLO WORLD\0".

### 3.5.2. RECEIVER

We use a MAZeT true color sensor. The response of this color sensor conforms to the CIE 1931 standard. An arbitrary number of amplifier stages can be used to get a desired amplitude for the signal; we use three stages. A transimpedance amplifier is used as the first stage (47 kOhm transimpedance resistor). We can change the amplification factor


(a) Transmitter's view (b) Receiver's view

Figure 3.19: Long range experiment setup

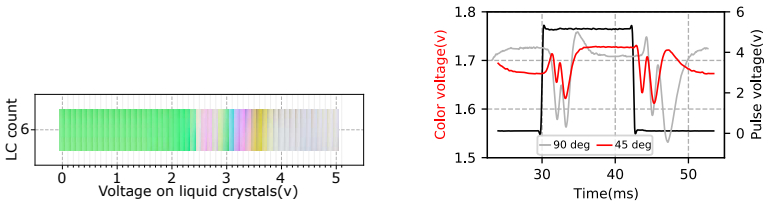


(a) Spectrum (b) Channel X response

Figure 3.20: 6 LCs: Rotation on roll axis at 45°

of the signal based on the distance to the transmitter, 31x gain for low range, and 143x for long-range. To make the platform able to communicate over long distances, we use a lens. The lens reduces the field of view, but it significantly increases the signal to noise ratio. The lens is adjustable, so the platform can be used from very short distances (~ 1 meter) to long distances (~ 50 meters). We make use of a well-known concept in optics called the "hyper-focal distance," which allows foreground and background to appear reasonably sharp. In our work, the position of the lens is fixed for any range beyond 15 m (approximately). That is, we do *not* need to adjust the lens for any range beyond that; we only calibrate the lens for ranges shorter than 15 m.

## 3.6. EVALUATION

To evaluate the platform, we look into two different scenarios. For natural light, we put our transmitter on a long aisle close to a window, as in Figure 3.19. During our evaluation, the light intensity was between 3 kLux (partly cloudy day) to 6 kLux (clearer day). For artificial light, we put our platform in a room and use a flashlight that radiates between 300 to 700 Lux depending on how close we place the flashlight to the transmitter. It is important to remark that our system does not cause any flickering effects. Similar to other studies [25, 23, 32, 34], our modulation is based on changes in polarization, which are not visible to the naked eye.

### 3.6.1. DATA RATE, RANGE, AND ROTATION

We use two different settings for the data rate: 1 kbps and 1.25 kbps. For each data rate, we send forty packets at each distance. A packet consists of 84 bits of data and one bit

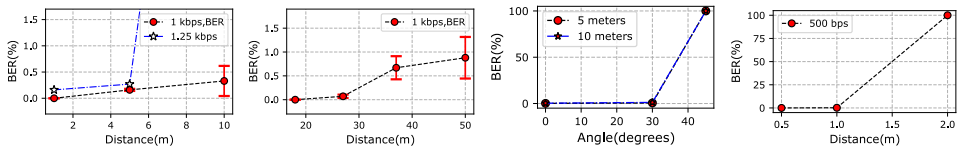


(a) Fast LCs: short range 300 to 700 Lux

(b) Fast LCs: long range, 3 kLux to 6 kLux

(c) Fast LCs: Rotations on roll axis

(d) Slow LCs: short range, 700 Lux

Figure 3.21: Evaluation results.



for synchronization. We will present the average and standard deviation of the measured BER of the total transmitted bits.

The 1 kbps data rate is obtained using the default A and B symbols shown in Figure 3.14a. For a data rate of 1.25 kbps, we bring those two symbols a little closer (modifying the corresponding voltages according to our modulation method), which increases the switching speed, but reduces the contrast.

Figure 3.21a presents the results with artificial light, where we obtain a range of up to 5 m with 1.25 kbps and 10 m with 1 kbps while maintaining the BER below 1%. An intensity of 300 to 700 lux is a relatively low value (standards suggest at least 500 lux for desk related work). Sunlight can provide values between a few klux (cloudy day) to several 10 klux (very sunny day). To test the performance of our system with natural light, we set it up in the hallway of our lab, see Figure 3.19. Figure 3.21b presents the results. We now achieve a 50 m range at 1 kbps with an average BER below 1%. Compared to the SoA, this range is 20 times longer than single-pixel systems providing a similar 1 kbps rate [33], and the data rate is 10 times higher than our prior single-pixel system that achieves a long range with sunlight (65m with 10k+ lux), but transmits only at 80 bps [44].

To test the resilience of our system to rotations around the roll axis, we modify the relative alignment of the analyzer from 0 to 45°. Figure 3.20a shows the color spectrum seen out of the six cells when the analyzer has a relative angle of 45°. Compared to Figure 3.6, the spectrum is shifted to the left. Figure 3.20b shows the X channel response for this configuration, where we can see that the response shifts in time. So long as the symbols A and B remain in the right slope, the system works, but if the shift is too far, the misalignment will break the link. Figure 3.21c shows the results with different rotation angles and two different ranges (under artificial lighting); beyond 30° the ChromaLux link breaks.

### 3.6.2. ENERGY CONSUMPTION

To measure the power consumption, we divide our system into two parts: the optical frontend (transmitter's LCs and receiver's color sensor) and the processing part (microcontroller for both). The power consumed by the LCs is so low (sub mW) that we could not measure it accurately. Thus, we use the well-known equation that considers their almost perfect resemblance to capacitors, assuming that the bit pattern consists of an equal number of zeros and ones: $P = CV^2 f$, where $f = \frac{\text{bit rate}}{2}$, $V$ is the weighted average of the middle voltage and 5V, and C is the capacitance of the LC stack (13 nF for our cells). The Tables 3.1 and 3.2 show the power consumption for our platform. Similar to all other

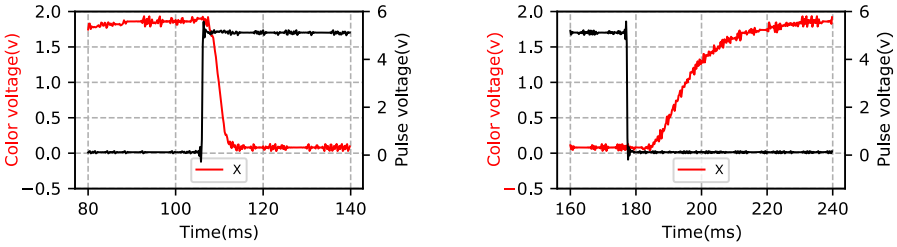


(a) 1 LC: Rising pulse

(b) 1 LC: Falling pulse

Figure 3.22: Empirical response for one slow LC

backscatter systems, the cost of the LCs is negligible. The bulk of the power is consumed by the processing and amplification at the receiver, a little over 100 mW in total.

| **Transmitter @ 1 kbps** | | |
|---|---|---|
| Component | Operating voltage | Power consumption |
| LC stack | 0, $V_{mid}$, 5 | 0.166 mW |
| Microcontroller | 3.3 | 27.3 mW |

Table 3.1: Transmitter power

| **Receiver** | | |
|---|---|---|
| Component | Operating votage | Power consumption |
| Sensor amplifiers | 3.3 | 72.6 mW |
| Microcontroller | 3.3 | 39.6 mW |

Table 3.2: Receiver power

### 3.6.3. GENERALITY OF THE SOLUTION

The method proposed in this paper can be applied to any type of TN liquid crystal cell, which is the most well-known and inexpensive type). To show that, we use our framework on another LC, which has a bigger surface area [61], and thus, is inherently slower. We utilize our constellation analysis (Section 3.3) to define the optimal number of cells (four in this case) and the optimal position of symbols, then to adjust the modulation accordingly, we utilize the methods presented in Section 3.4.

Figure 3.22 shows the temporal response for one cell. The rising and falling times are around 6 and 40 ms, significantly slower than the ones used for our first LC at 3 and 4 ms, respectively (Figure 3.7). Figure 3.23 shows the responses for the optimal number of slow cells (four). Note that the transient state exposes peaks and valleys with high contrast, but they do not look like mirror images of each other, which was the case for the first LCs (Figure 3.14a). This asymmetry is due to the bigger difference between the falling and rising times. This high asymmetry requires a careful analysis of the constellations

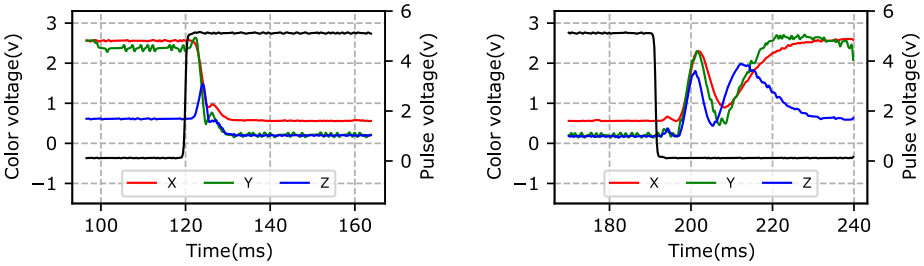


(a) 4 LC: Rising pulse

(b) 4 LC: Falling pulse

Figure 3.23: Empirical response for four slow LCs

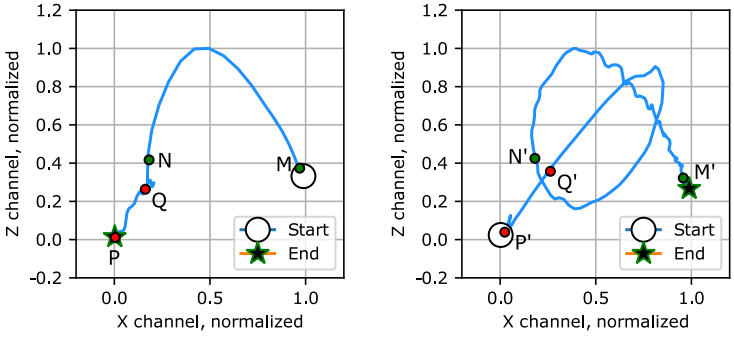


(a) Rising pulse

(b) Falling pulse

Figure 3.24: Constellations for four slow LCs

for this setup, shown in Figures 3.24. Considering the backflow effect of LCs, only two regions are suitable for modulation; one is between points M and N (and respectively M' and N' in the falling response), and the other is between points P and Q. As we are using channel X to transmit data, points M and N have a higher SINR, compared to points P and Q, and thus, we use them.

After fixing the middle voltage, for bit 0, the modulation and demodulation remain the same for the other type of liquid crystals. Figure 3.21d shows the results with artificial light (short-range with 700 lux). Observe that even though the total response time (falling + rising time) for a single cell is around 50 ms (~20 bps with basic OOK), ChromaLux obtains a 25× higher data rate (500 bps). It is important to note that studies like PassiveVLC [33] and LuxLink [44] do not use such slow LCs, but faster ones similar to the ones in our first batch of experiments. Thus, ChromaLux shows that it can improve the performance of LCs that have not even been considered in the backscatter community for being too slow.

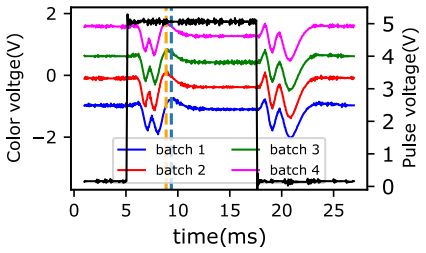


Figure 3.25: Characterization of different LC batches.

## 3.7. DISCUSSION

In this section, we elaborate on some difficulties that arise as a result of stacking LC cells in series.

### 3.7.1. CARRIER SIGNAL ATTENUATION

In ChromaLux, we stack off-the-shelf LC cells because we cannot manufacture a cell with the desired optical properties. The main disadvantage of stacking LCs is that instead of using two glass electrodes, we use $2 \times n$. To calculate the attenuation, we can do the following numerical analysis. The glasses used in LC cells are coated with Indium-Tin-Oxide (ITO), which is a transparent conductor. Some ITO layers can transmit a maximum of 90% of visible light [62]. Hence, the transmission factor caused by the six cells is about $0.3$. We measured the transmission factor of our cells and found that six cells lead to a value of 0.37, which is a little bit better than the theoretical result. This attenuation reduces the range by approximately 40% [63]. That is, instead of reaching 50 m, designing a custom cell with only two glass electrodes could reach a distance of 80 m.

### 3.7.2. VARIATION OF LC CELLS

Due to inaccuracies in the manufacturing process, it is possible for LCs to have different optical responses, and these differences could distort the modulation of symbols. To evaluate this aspect, we test four batches of six LC cells each. The six cells are different combinations taken out of a set of eleven cells.

The results are shown in Figure 3.25, which captures the optical responses in the X channel for a 40 Hz pulse. We can observe that, except for batch 1, all the other batches have a strong alignment. Batch 1 has a delay of around 0.5 milliseconds. This delay would not affect the modulation of the 'flat' bit 0, but it could distort the shape of the bit 1. Instead of a $\bigvee$ shape, the bit 1 would have a $\curlyvee$ shape. The system would still be able to demodulate the bit 1, but if the delay increases further, the $\curlyvee$ shape may start becoming a flat line, rendering the demodulation futile. If instead of a delay, the signal would come ahead of time. The $\bigvee$ shape would turn into a $W$ shape. The system would still be able to decode a bit 1; however, the corrected phase would be off by one-forth of the symbol length. If the signal keeps on starting earlier, the modulation of the bit 1 would be done inside the backflow region, which may create undecodable distortions. To overcome this problem, a feedback loop can be created at the transmitter to fine-tune the modulation

parameters (timers) in order to adjust to the observed delays.

## 3.8. CONCLUSION

In this work, we looked into a fundamental assumption made on backscatter communication: the idea that changes in light intensity between the end states of LCs follow a monotonic function. Based on first principles, we showed that LC-based transmitters can be designed to have non-monotonic transient states that can be exploited to increase the link's capacity. Compared to existing single-pixel systems, ChromaLux achieves simultaneously a long range (50 m) and a high data rate (1 kbps). The most important contribution of ChromaLux, however, is that it provides an initial framework for a principled design of ambient backscattering.

# 4

# SPECTRALUX

A key observation about the passive VLC systems proposed so far is that they do not exploit the vast bandwidth of 400 THz in the visible light spectrum (ranging from 375-780 nm). While RF communication, as well as optical fiber systems, make extensive use of sub-band modulation (e.g., OFDM), most passive VLC systems treat all incoming light as a single band, restricting themselves to amplitude- [33, 44, 32] and time-based modulation schemes [34]. Figure 4.1 shows an incoming spectrum on the left side. That spectrum is composed of many wavelengths that –in theory– could be modulated individually, which would allow for encoding many bits in a single light ray. This is important as commodity LC shutters have not been designed for switching at high speeds, following the description of Chapter 1.

We conjecture that the lack of spectrum-aware modulation in passive VLC is due to a limited understanding of the physical properties of LC cells. Chapter 3 has shed some light on how LCs behave with voltage, allowing them to reduce the switching times by toggling between two intermediate *colored* states instead of pure opaque (black) and translucent (white) [64]. In this chapter, we explore the possibilities of utilizing the broader spectrum provided by a stack of LCs. The main challenge is that, in contrast to RF communication where the availability of band-pass filters with high Q factors enables transmitting and receiving individual sub-bands, LCs cannot be driven in such a fine-grained and orthogonal way. Yet, the voltage-driven spectrum emitted by LC shutters is rich and diverse, allowing for modulation schemes that consider properties other than the intensity of light, as depicted in Figure 4.1. Overall, our contributions can be summarized as follows:

1. **A theoretical model for using crystals as transmitters in the spectrum domain:** By investigating the physical properties of LCs, in Section 4.1, we show that these devices can generate different spectrum patterns. Contrary to traditional modulation methods, where only the intensity of the whole spectrum is used to carry information, we increase the link's capacity by creating multiple symbols.

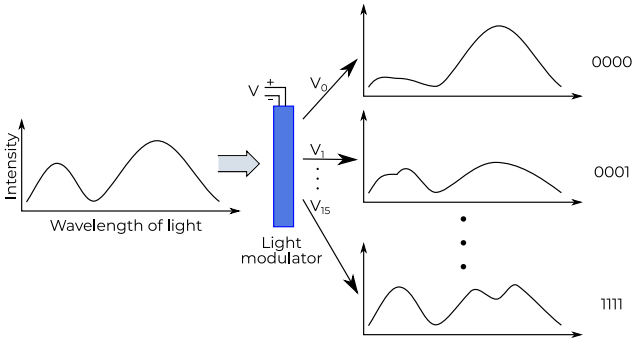


Figure 4.1: Main concept. The spectrum of a light source (left) is controlled with a liquid crystal through changes in voltage. Communication symbols are mapped to different spectra (right). A receiver measures the spectrum to decode the data.



2. **A novel (de)modulation method to apply our theoretical model to off-the-shelf LCs:** In Section 4.2, we select symbols in the spectrum domain to transmit data. We will show that the received signals resemble spectrograms, and we decode symbols using machine learning algorithms.

3. **A prototype for test and evaluation:** We build a transmitter based on LC cells and use a spectrometer in the receiver. To show the effect of the different light spectra, we test our link using different light sources, and compare the range and bit error rates (BER) of the system in various scenarios.

## 4.1. SPECTRUM-AWARE PASSIVE VLC

To increase the bandwidth of our VLC platforms, we investigate spectrum modulation. When perceived by human eyes, different bands of light translate into colors. However, thinking in terms of color is too limiting; the visible light spectrum is much richer than the canonical 3-dimensional Red, Green, and Blue (RGB) color space. To reveal this potential, we employ a spectrometer capturing 256 bands (15 nm wide) of light, providing more room for multi-symbol coding. In addition to a spectrometer being used as a VLC receiver, we have to find a way to modulate sub-bands of light. This is easily achieved in active VLC, as light sources allow for fine-grained control over light wavelengths. However, we need novel to achieve this in passive VLC. We show that LCs can perform this task, despite the fact that a typical LC shutter has been manufactured to do just one thing well: switch between opaque (black) and translucent (white), as mentioned in Section 2.1.

In Chapter 3, we have shown that commercial off-the-shelf LCs can produce “colors” when stacked. We used this insight to make a faster OOK modulation by selecting two symbols from the RGB color space. In this section, we deepen our understanding of how LCs operate on light’s spectrum, which helps us to design and implement the platform of this chapter, dubbed SpectraLux.

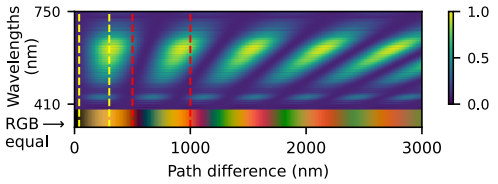


Figure 4.2: Modeled impact of path difference on flashlight spectrum per wavelength. The color on the bottom shows the combined effect of the wavelengths in the column above.

### 4.1.1. LC'S AS SPECTRUM MODULATORS

In Section 3.1, we showed the *color* modulation property of LC cells. Following Equation 3.1, when polarized, multi-chromatic (white) light enters a crystal, each wavelength will have a different attenuation of $L$. The different levels of attenuation faced by every wavelength is what allow us to change (modulate) the spectrum. Due to its importance, this equation is repeated below:

$$L(\Gamma,\lambda) = sin^2(\frac{180^\circ \times \Gamma}{\lambda}) \tag{4.1}$$

To compute the modulating effect on a specific ambient light source (e.g., a flashlight or sunlight), we need to account for the amplitude of the various wavelengths in its spectrum as follows:

$$A_o(\Gamma,\lambda) = A_i(\lambda) \times L(\Gamma,\lambda) \tag{4.2}$$

where $A_i$ is the amplitude of the input light for wavelength $\lambda$, $\Gamma$ is the path difference of the LC cell, and $A_o$ the amplitude of the light ray at the output of the analyzer. Taking all wavelengths into account will lead to the final color of the light exiting the LC shutter.

#### MODIFYING THE SPECTRUM

With the basic model captured in Equations 3.2, 4.1, and 4.2 we can study the impact of the path difference, controlled by the LC voltage, on the spectrum formed after the analyzer. This analysis is important as we need to select spectra that differ enough to serve as communication symbols. Figure 4.2 shows the effect of LCs (emulated with the above equations) on the spectrum of a phone's flashlight when increasing $\Gamma$ from 0 to 3,000 nm. In the spectrogram, yellow denotes the maximum received intensity, i.e. 1, and the dark blue denotes 0. Besides, to get a feeling of the spectrum, we show the colors perceived by human eyes[1] below the spectrogram. Once again, note that the human eyes reduce the visible light spectrum to only three RGB dimensions, and hence, color sensors or cameras provide only limited information.

Most off-the-shelf LC cells are made to operate between the darkest ($\Gamma = 0$), and the first light region ($\Gamma = 70$), shown by the dashed yellow lines in Figure 4.2. Although some gray and yellow tones can be obtained in between, richer spectra are present for higher path differences. Since the path difference can be increased with the crystal thickness $d$

[1] using the CIE-1931 standard

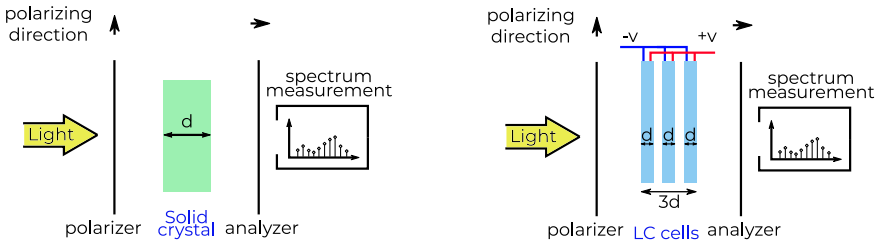


(a) Using a solid crystal

(b) Using multiple LCs

Figure 4.3: Stacking LC cells as an alternative to thick cells.

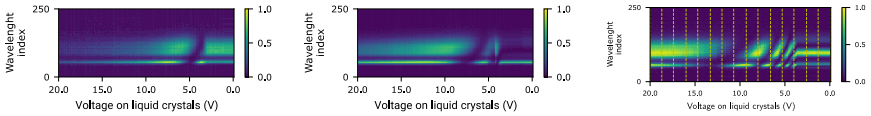


(a) 1 LC

(b) 2 LCs

(c) 4 LCs

Figure 4.4: The effects of varying the driving voltage on the spectrum of a phone's flashlight when passing through a stack of LCs. The voltages are plotted from high to low to match the corresponding theoretical results in Figure 4.2.

(using Equation 3.2), stacking multiple LC cells and driving them with the same voltage, as depicted in Figure 4.3, allows reaching the richer spectra [64]. For example, if we stack two LCs together, we can cover the spectrum within the red dashed lines in Figure 4.2.

### 4.1.2. USING LCS IN COMMUNICATION

LCs have typically been used in passive-VLC by toggling them between transparent and opaque, which makes sense when using a photodiode as a receiver. With a spectrometer, however, we can select many more symbols (vertical lines in Figure 4.2) provided that their signatures (intensities at various wavelengths) differ enough. As stated before, stacking multiple cells increases the thickness (of the combined) crystal, enabling richer spectra. However, adding too many LCs has downsides. The first disadvantage is the attenuation of light caused by the glass panels used for each LC cell (discussed in Section 4.6). A more severe problem is assuming that all LCs are switched at the same time with high precision, which is unlikely. As the number of LCs increases, the resulting spectra become less predictable or require long switching (stabilization) times. Consequently, the best approach is to use the fewest possible LCs that allows for sufficiently long inter-symbol distances.

To choose the optimum number of LCs, we need the $\Gamma$ value, but most off-the-helf manufacturers do not provide this parameter. Thus, for the pi cells used in this paper, which are manufactured by Liquid Crystal Technologies [65], we perform empirical measurements to obtain the effect of path differences on the spectrum patterns. We use the setup in Figure 4.3b, with a phone's flashlight as the input source, and a driving voltage sweeping from 0 to 20 V. This voltage is higher than the canonical 5 V used for driving typical LC shutters; in return, the pi cells switch faster: 400 vs. 150 Hz. Figure 4.4 shows

the spectrogram for different numbers of LCs stacked together. When increasing the number of LCs, more patterns start appearing that resemble the trends of the theoretical model, cf. Figure 4.2. One noticeable difference is that, in reality, the changes in the spectrum start taking place at a voltage higher than 0 V; operating LCs below this voltage has no effect.

The main takeaway of our analysis is that it is indeed possible to use the driving voltage of LCs to control –to some degree– the output spectra. Based on our empirical results, we will be working with 4 pi cells from now on.

## 4.2. MODULATION

Modulation with LCs is more involved than just selecting a few symbols (columns) from the spectrogram in Figure 4.4; timing needs to be considered as well. LCs have a slow response, of a few hundred hertz. To provide enough time for the LCs to reach a steady state, in Figure 4.4, the measurements maintain the voltage level at the LC for 1 second. In a real link, the system cannot wait for such a long time, as the data rate would reduce dramatically. In this section, we provide a framework to increase the modulation speed.



### 4.2.1. VOLTAGE ANALYSIS: BORDERS VS. TRANSITIONS

Following the characterization of the LC stack shown in Figure 4.4c, an intuitive approach to selecting communication symbols is to map each symbol to a unique voltage, as shown by the vertical yellow lines in the figure. But as stated before, we do not want to wait too long to reach a given voltage (symbol)[2].

Instead of waiting to reach the desired symbol, we propose to use the transition between symbols. As can be seen in the spectrograms, switching between two voltages causes a continuous variance in the light spectrum. In our experiments, we found that the variation pattern is *unique* for each pair of start and end voltages. And with this transient pattern, we can predict the end voltage without waiting until it is reached. For example, if we have a transition between a starting voltage $V_s$ and an end voltage $V_e$, we can infer that $V_e$ is the intended symbol, simply by using the first part of the transition $V_s \rightarrow V_e$. We call the voltages *borders* to differentiate them from transitions. In Section 4.5, we will show that this early decoding approach is valuable in reducing the symbol duration, and hence, increasing the data rate.

The trade-off for using transitions is higher decoding complexity. Instead of using a list of $n$ voltages, the system needs to keep a list of $n^2$ transitions, this process is explained in Section 4.3. Next, we provide a deeper analysis of transition times in LCs.

### 4.2.2. SETTLING TIME

Considering that transitions occur between any pair of voltages, we are interested in identifying what range of voltages provides the fastest transitions.

From a *materials' science* perspective, some prior studies have looked into the dynamic behavior of pi cells. To measure how fast a cell can be switched, the *settling time*

[2] Following Shannon's equation, $C = B \times log(1 + SNR)$, which states that bandwidth increases the capacity linearly, as opposed to the SNR which only provides a logarithmic improvement, we prioritize reducing the symbol period (increasing the bandwidth) over maximizing the inter-symbol distance (increasing the SNR).

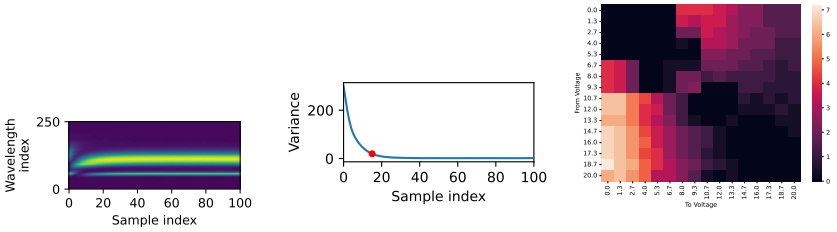


(a) Spectrogram of a transition (b) Variance of the Spectrogram (c) Settling time heatmap for all transitions

Figure 4.5: Settling time measurement steps and results.



is defined as the time needed to achieve the optical transition when the cell is switched from a start ($V_s$) to an end ($V_e$) voltage. In [66], the dynamic behavior of pi cells is modeled using the hydrodynamic equations of Ericksen-Leslie. The associated simulations show a high variance in switching times between the same $V_s$, and two different $V_e$ voltages.

From a *wireless communication* perspective, the high variability in switching times poses a key challenge: the symbol duration is not constant. Communication systems avoid variable-length symbols because the receiver is unable to use a fixed period to determine the boundary between symbols. To overcome this limitation, our approach follows two steps to define a *constant* symbol period:

- First, we measure the settling time in various regions of the spectrum in order to identify the region with the shortest switching times.
- Second, we select symbols in this *'fast-transitioning region'* and define the symbol period as the slowest transition among these symbols.

Our two-step approach can be done with the help of simulations, however, to do so, one needs the physical properties of the pi cells, which are not provided by our supplier. Thus, we perform empirical measurements to analyze the fastest settling times.

### SETTLING TIME MEASUREMENT

To analyze the settling times, we select sixteen equidistant points (voltages) in the spectrogram defined for a stack of 4 LCs, as shown in Figure 4.4. After that, we measure the optical transitions between these voltages. Each transition is measured for 50 ms. The goal of this experiment is to find what region of the spectrum is the *fastest*, in terms of switching time between voltages. An example of a spectrogram transitioning between the 3rd (4 V) and 2nd (2.7 V) voltage levels is shown in Figure 4.5a. Notice that, after an initial *transitional* region, the spectrum remains rather constant. To calculate the settling time, a moving window is run along the horizontal axis, and the variance within the window is calculated for each wavelength (vertical axis). Then, we average the variance across all wavelengths for each vertical point, as depicted in Figure 4.5b. The settling time is defined as the point when the variance decays below a predetermined threshold, set to 20in our case (red dot in Figure 4.5b). Following these steps, we generate the set-

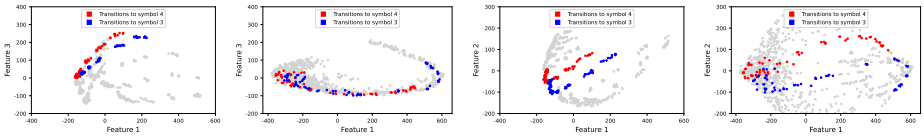


(a) Features 1-3, slow & broad

(b) Features 1-3, fast & narrow

(c) Features 1-2, slow & broad

(d) Features 1-2, fast & narrow

Figure 4.6: Constellations of eight voltages (symbols) with the slow & broad spectrum (left) and the fast & narrow spectrum (right). In total, the system observes 64 transitions between voltages, and each symbol is represented by eight of those transitions. The features are obtained using Principal Component Analysis (PCA).

tling time matrix shown in Figure 4.5c, where the vertical axis represents the start voltage $V_s$ and the horizontal axis represents the end voltage $V_e$.

#### ANALYSIS OF THE SETTLING TIME MATRIX

By looking at the matrix in Figure 4.5c, we get the following insights: *a) The matrix is not symmetric.* For many voltage pairs, going from high to low voltages takes longer than the reverse transition. The reason is that during a rising pulse, i.e. $V_e > V_s$, the liquid crystal changes under the influence of an electric field, whereas when $V_e < V_s$, the molecules rely on inertial forces to realign themselves. The force applied by the electric field is stronger than the inertial forces, and hence, rising pulses make faster transitions. *b) The settling time increases sharply when $V_e$ is below the fourth voltage level* (equal to 5.3 volts). This occurs because the LC approaches its critical voltage $V_c$. This observation matches measurements done by Chen et. al. showing that when LCs operate around their critical voltage the relaxation times start to increase [67].

Overall, the settling time matrix indicates that symbols should be selected from the bottom right corner (darker region) because all transitions take ~2.5 ms in both directions. Utilizing the entire matrix would entail considering settling times as high as 8 ms, reducing the data rate by a factor of ×3.2. The trade-off for choosing this *fast* region is that we do not exploit the entire spectrum provided by the LCs. The fast, but narrower, region reduces the signal-to-noise-to-interference ratio (SNIR) and leads to a more condensed symbol constellation, i.e the distance between symbols is shorter.

**Key design takeaway.** Given that the channel's capacity grows *linearly* with bandwidth (shorter symbol period) but only *logarithmically* with the SNR–as stated by the Shannon equation–, our design prioritizes bandwidth over SNR, and thus, we choose a *few fast symbols* (from the bottom-right part of the matrix) instead of selecting *many slow symbols* (from the entire matrix).

### 4.2.3. CONSTELLATIONS

In the previous subsection, we mention that if all symbols (voltages) are selected from the darker region of the matrix in Figure 4.5c, the data rate can be higher than when symbols are spaced out over the entire range. This raises the concern that symbols might get too close leading to overlapping decision regions, which prevents their reliable detection. To investigate the relation between the overlap of decision regions and the width of

the spectrum, we perform an experiment using the deployment presented in Figure 4.3b. The light source is a flashlight and the distance between the transmitter and receiver is 1 m. With that deployment, we consider two setups.

*Setup 1, broad spectrum*: Eight symbols are selected from the entire voltage range (0 to 20 V).

*Setup 2, narrow spectrum*: Eight symbols are selected only from the fast region in Figure 4.5c (10.7 to 20 V).

For each setup, we transmit one hundred messages containing all 64 transitions. Every transition is captured as a matrix, as shown in Figure 4.5a, where the rows are the wavelengths measured by the spectrometer and the columns are the number of samples. In Section 4.3, we show that the information contained in the transition matrix can be compressed to 12 features while keeping more than 99 % of the information in the whole transition. In Figure 4.6, we use three of these features to give an idea of the effect of the spectrum width on symbol overlap. Figures 4.6a and 4.6c are from *Setup 1*, and figures 4.6b and 4.6d from *Setup 2*. Each dot is a transition and there are 64 transition clusters on each figure. Given that a symbol (end voltage) is a collection of eight transitions, those eight clusters belong to the same class. For clarity, the figures only highlight two contiguous symbol classes (red and blue) and leave the other six symbols in light gray.

The important observation from these plots is that reducing the spectrum width (left vs. right), reduces the distance between the symbols (as expected), which is most visible for the narrow spectrum in the top-right plot (Figure 4.6b), where the clusters of red and blue symbols largely overlap. Yet, even these seemingly "too narrow" and overlapping symbols can be decoded as other features (top vs. bottom) do separate them much more clearly as shown in Figures 4.6c and 4.6d, where the overlap is minimal for both spectra, broad and narrow. In general, the broader the spectrum, the more separation among the various PCA features, but since we will be using 12 PCA features to disentangle the symbols, there will be further dimensions to minimize the chance of complete overlap.

The point of this experiment is to provide an initial observation about the possibility of decoding symbols with a fast, but narrow spectrum. For a complete answer, we need to tackle two important points: (i) consider all transitions and features, and (ii) utilize a mechanism that can draw complex boundaries in the feature space to cope with the nonlinear patterns of our constellations. Next, we propose a demodulation method based on machine learning algorithms to tackle these two challenges.

## 4.3. DEMODULATION

At the receiver, a spectrometer captures the wavelengths of the light coming from the transmitter. A sample packet signal is shown at the top of Figure 4.7a. We can see that different patterns are generated when the voltage applied on the LC stack changes over time. The receiver captures the spectrogram as a $w \times m$ matrix where $w$ is the number of wavelengths at the receiver and $m$ is the number of samples captured.

### 4.3.1. SYMBOL EXTRACTION

The communication link requires extracting the symbols from the spectrograms. To achieve this goal we perform three steps: parameter setting, preamble detection & clock recovery, and the actual symbol extraction as described below.

#### PARAMETER SETTING

A vital consideration in our approach is to minimize drift effects (accumulation of errors due to inexact measurements of the symbol period). If the transmitter's frequency and the receiver's sampling rate are not defined well, the number of samples per symbol varies. For example, the matrix of one symbol may have $c$ columns and the next symbol may have $c+1$ columns. These variations may seem small but they can cause severe detrimental effects in the machine learning process.

To avoid this problem, we make sure that the receiver captures an equal number of samples per symbol by setting the transmitter's symbol duration $r_t$ as an *integer multiple* of the receiver's sampling period $r_s$: $r_t = n \times r_s$, where $n \in \mathbb{N}$.



#### PREAMBLE DETECTION & CLOCK RECOVERY

The receiver does not know the length of the transmitter's symbol period $r_t$, it only knows that it is set as an integer multiple of its sampling period. To identify the symbol's period, we design a preamble that causes abrupt changes in the spectrogram, so it can be easily detected. The packet's preamble is designed to serve two purposes: a) recovering the transmitter's clock, i.e. identifying the value of $n$ in $r_t = n \times r_s$, and b) marking the start of the payload. To detect the changes in the preamble, we consider the fact that the time response of LCs follows an exponential trend, similar to that of a capacitor: when the voltage switches from one symbol to another, the spectrogram changes with the highest gradient at the beginning, and the rate of change decreases as the LC reaches its final state.

To reveal the beginning of symbols, we run a Sobel filter along the horizontal axis of a spectrogram. The Sobel filter is a 1-D (row-wise) derivative in image processing used to measure gradients. The output of this filter is a matrix with the same size as the original image, as shown in the middle of Figure 4.7a. By summing this matrix along each column, we get the curve D(n) shown at the bottom of Figure 4.7a. The peaks in D(n) denote the times when the voltage on the LCs is switched, i.e. when the capacitance model exhibits the fastest change. To maximize the likelihood of detecting the peaks in the preamble, we use the two most-extreme symbols in the constellation. The transmitter sends 6 consecutive transitions between those two extreme symbols as shown by the first six peaks at the bottom of Figure 4.7a.

#### SYMBOL EXTRACTION

In theory, every transition between symbols should be detected in the Sobel plot. In practice, not all the beginnings of symbols generate a clear peak. This occurs mainly when similar or very close symbols are sent consecutively. Such an example is shown Figure 4.7a at around 54 ms where the payload contains two identical symbols back-to-back.

In this case, we estimate the beginning of the symbols based on the clock information obtained in the previous step. Whenever the distance between two peaks in the Sobel

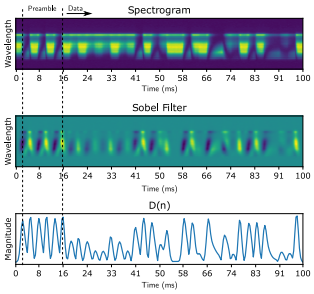


(a) Spectrogram with Sobel filter and D(n) of a sample packet containing a preamble (first 6symbols) and a payload.

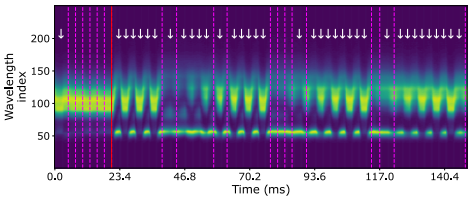


(b) Symbol transitions. Red: start of the preamble. White arrows: symbol borders obtained with D(n), and magenta lines: inferred from the clock cycle.

Figure 4.7: Symbol detection processing steps

plot is greater than one clock cycle (which is extracted from the preamble), we divide that period into smaller components equal to the clock duration.

To test the validity of this method, we use a "helper wire" between the transmitter and receiver, signaling the start of packets and symbols. The estimated symbol borders turned out to be exactly the same as the ground truth. Figure 4.7b shows the results of our peak finding approach. The red line marks the beginning of a packet, the white arrows mark the symbol transitions detected by the Sobel plot (i.e. clear peaks), and the magenta dashed lines mark the transitions detected through the use of the inferred clock (i.e. unclear peaks).

### 4.3.2. FEATURE EXTRACTION

With the borders found in the previous step, the spectrogram is split into smaller matrices (slices) for each symbol. The size of each matrix is $w \times n$, where $w = 250$ (number of wavelengths) and $n = 7$ (number of samples). The number of samples follows from the settling time and sampling rate of the spectrometer. Some examples of "transition slices" can be seen in Figure 4.7b.

The problem with these matrices is that they are big ($250 \times 7 = 1750$ inputs), increasing the complexity of the overall system. To reduce this size, while retaining the most important information for each symbol, we apply a PCA algorithm as mentioned before. PCA dramatically reduces the dimension of the original dataset[3]. Figure 4.8a depicts the information captured by the most relevant components. We use the 12 most relevant dimensions, which reduce the input size by more than x100 and preserves more than 99 % of the original variance in the data. In our evaluation, we show that using 12 features provides links with a BER of 0%. Using fewer than 12 features dramatically reduces performance, while only marginally improving computational overhead.

[3]The PCA implementation is obtained from scikit-learn [68].

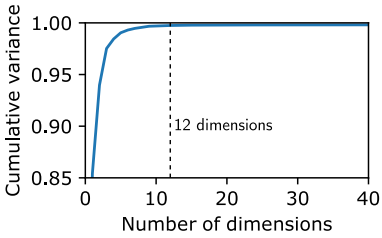


(a) Cumulative variance of PCA dimensions.

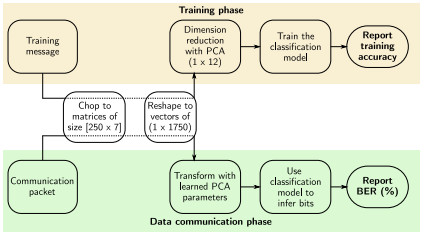


(b) Flowchart of the training and demodulation processes.

Figure 4.8: Cumulative variance as a function of PCA dimensions (a), and the system flowchart (b).

### 4.3.3. CLASSIFICATION: TRAINING AND TESTING

Our system requires sending first training packets. These training packets contain all $n^2$ transitions, so the receiver can obtain the required PCA features to decode the subsequent data packets. Figure 4.8b provides an overview of the entire communication process, including both training and actual packet transmissions.

There are various machine learning methods that can be used to classify the features obtained from the PCA results. As described in Section 4.2.3, our symbol constellations require methods able to draw complex boundary conditions. After some preliminary investigations using different machine learning methods, we chose Neural Networks for this purpose, as they can adapt well to the needs of our demodulation process. Some Deep Learning techniques like Convolutional Neural Networks (CNNs) are also well suited to such tasks. However, CNNs have a deep network with a large number of neurons requiring more memory and much more training data to avoid over-fitting. Therefore, in our approach, we use a simple fully connected neural network with 2 hidden layers of 64 and 32 neurons each, and an output layer of 8, or 16 neurons depending on the number of symbols chosen[4]. The model uses categorical cross-entropy for the loss function, and the Adam optimizer with a learning rate of 0.001. The training is carried out for 25 epochs.

For the link to work well, we need to provide the Neural Network with enough training data to successfully classify the $n^2$ transitions. Exactly how much training data needs to be collected is not clear a priori and will be studied in Section 4.5.

## 4.4. PLATFORMS

To evaluate the multi-symbol communication link, we build prototypes for the transmitter and receiver using commercially available devices. Next, we describe the systems, cost, and power analysis.

### 4.4.1. TRANSMITTER

As mentioned before, in order to expand the spectral coverage, we stack 4 pi cells and connect their pins in parallel, as shown in Figure 4.3b. All these ports are actuated with

[4]We use an implementation from Keras [69]

a signal generator to create communication packets. Figure 4.9a shows our prototype transmitter. Non-polarized light enters through the polarizer, is modulated using the pi cells, and exits through the analyzer towards the receiver. The LCs we use could be modulated with very high voltages, up to 100 volts, however, due to the limits of the signal generator, the maximum actuation voltage that can be generated is 20 volts. Working at higher voltages has the advantage of increasing the modulation speed, and hence, increasing the data rate. At the same time, it consumes more power. Since our goal is to explore the use of the spectrum, using lower voltages does not change the proof-of-concept, and can be left as a design choice.

### 4.4.2. RECEIVER

The design of our receiver has to fulfill three requirements:



1. Measure the light spectrum with enough precision
2. Have at least twice the sampling speed of the communication link to satisfy the Nyquist requirement.
3. Be embeddable in a custom electronic system.

We considered three options: a low-end (AS7265X), a medium-level (Hamamatsu C12880), and a high-end (Thorlabs) spectrometer. The low-end option does not satisfy requirements (1) and (2) and the high-end does not satisfy requirement (3). For the final design, we choose the C12880 Hamamatsu spectrometer. This sensor operates as a 1-dimensional camera, where each pixel measures a small range of wavelengths, and all the wavelengths are read sequentially. This sensor has two important metrics, one is its pixel clock, and the other is the line (sampling) rate. The wavelength sensitivity of this sensor is from 380 nm to 850 nm, and the maximum line rate is 5 kilo lines per second. The prototype of our receiver is shown in Figure 4.9b. We design and build a driver PCB for the spectrometer, and record the intensity at each light wavelength. The driver circuit has the main task of generating clock pulses and converting the sensor values using an Analog-to-Digital converter (ADC). To focus the receiver on the area covered by the LC cells, we place a lens in front of the sensor. In this version of our receiver, the embedded microcontroller does not demodulate the information. The spectral data is forwarded to an external PC, which runs the classification algorithms and decodes the information.

### 4.4.3. COSTS AND POWER CONSUMPTION

Cost and power consumption are two important factors when evaluating embedded systems, specifically for passive-VLC, where being low-power is key. In this section, we focus on these two parameters.

#### COST

Table 4.1 shows the cost of the main components for the transmitter and receiver. As far as we know, this is the first work using a spectrometer as the receiver for passive VLC. To have a precise view of the phenomena, we chose the best integrated spectrometer we could find, however, with some engineering effort, accurate but cheaper receivers can also be made using analog spectrometers [70] and high-speed image sensors [41].

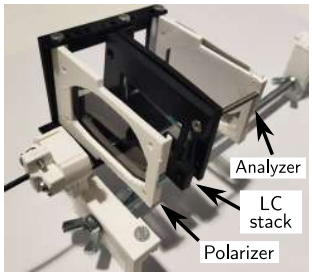


(a) Transmitter

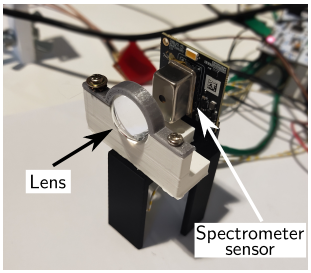


(b) Receiver

Figure 4.9: Pictures of the transmitter and the receiver.



| List of key components | | | |
|---|---|---|---|
| Component | Tx or Rx | count | Price per item |
| STM32 microcontroller | both | 2 | 12 euros |
| Spectrometer | Rx | 1 | 290 euros |
| Lens | Rx | 1 | 5 to 25 euros |
| Pi cell | Tx | 4 | 15 euros |

Table 4.1: Device costs

### LCs' POWER CONSUMPTION

The speed of the transmitter is the key factor determining its power consumption. If an LC is modeled as a capacitor, its power consumption can be estimated by the following equation:

$$P = CV^2 f$$

where C is the LC's capacitance, V is the voltage swing on the capacitor, and f is the frequency of the voltage V. Our measurements show that each pi cell has a capacitance of about 6.7 nF. Following the modulation method explained in Section 4.2, a 1 kHz pulse is put on 4 pi cells. With V peaking at 20 volts, the total power consumption is shown in Table 4.2.

| Component | Operating voltage | Power consumption |
|---|---|---|
| Pi cells | 2 V to 20 V | 0.7 mW |

Table 4.2: LCs' Power consumption @ 1.3 kbps

This sub-milliwatt consumption of LC cells is in agreement with the values reported by other passive VLC studies [33, 64].

### SPECTROMETER'S POWER CONSUMPTION

In the receiver, the power consumption depends mainly on the clock frequency of the spectrometer. In our case, the spectrometer is clocked at 2.4 Mhz. Following the information in the datasheet of the spectrometer, its power consumption is summarized in Table 4.3.

| Component | Operating voltage | Power consumption |
|---|---|---|
| C12880 Hamamatsu | 5 V | 0.166 mW |

Table 4.3: Spectrometer's power consumption

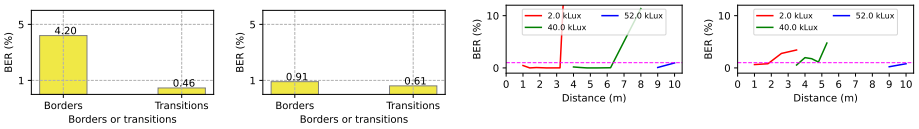


(a) Symbol duration 2.6 ms (b) Symbol duration 3.4 ms (c) 1.1 kbps using 8 symbols (d) 1.5 kbps using 16 symbols

Figure 4.10: Comparison between using transitions versus borders (a) and (b), and BER performance at different distances (c) and (d).

## 4.5. EVALUATION

In this section, we evaluate the performance of our system in terms of data rate, range, and bit error rate (BER). We explore various scenarios considering different numbers of symbols, ranges, light sources, and ambient lighting conditions. First, we evaluate one of the main insights of our study, which is that using *early* transitions to decode symbols is a plausible alternative, as opposed to waiting until the spectrum of the end voltage is reached. Then, we expose our system to different working conditions. And in the last part, we address the training cost of the machine learning models used for classification.

### 4.5.1. BORDERS VERSUS TRANSITIONS

During the demodulation, we use the initial part of the transition between two voltages (symbols) for the classification task. However, this increases the required training data quadratically. Due to this trade-off, we need to evaluate both methods to verify the advantage of using transitions. The following experiment reveals that when transitions are used, the minimum symbol duration with acceptable BERs is 2.6 ms. On the contrary, when using borders, the system needs to wait longer for a transition to settle: 3.4 ms.

Basic setup: To have a controlled environment, we set the experiments in a dark room with a light source placed directly behind the LCs. In this way, we minimize errors due to external sources and capture only the performance of the modulation technique. Additionally, the transmitter is kept within the line of sight of the receiver, with angle deviations of less than 10 degrees.

With this basic setup, we set the transmitter and receiver at a 1 m distance and send a constellation of $n = 8$ symbols, so 3 bits/symbol. Each packet has 78 symbols, 6 symbols for the preamble, and 72 symbols to accommodate all 64 transitions. The transmission delay of each packet is between 0.2 s and 0.3 s, depending on the symbol period used, 2.6 ms or 3.4 ms, respectively. The sequence of transitions in the training packets is fixed and known, but to prevent over-fitting the neural network model, the data packets contain random sequences. For all the experiments done in this section (with different ranges, light sources and light intensities), we transmit 60 packets to train the Neural Network model, and then, 60 data packets to demodulate information.

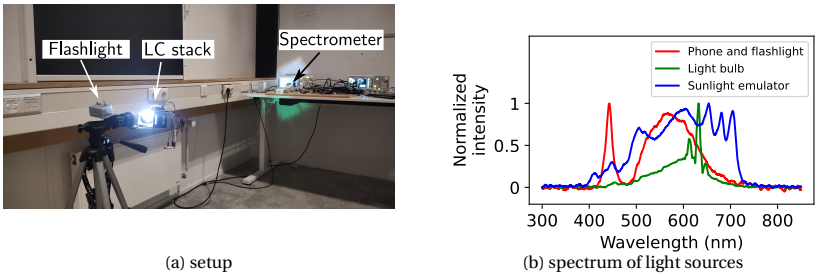


(a) setup (b) spectrum of light sources

Figure 4.11: Evaluation setup and light sources



Figures 4.10a and 4.10b show the results of the borders vs. transitions experiment. While the method using transitions achieves a BER below 1% for both symbol periods, the performance using borders degrades significantly when the symbol period decreases, increasing the BER from 0.9% to 4.2%. Considering that in passive-VLC the single-most-important bottleneck is data rate, many studies trade off complexity to increase the link's speed. We follow the same principle, and hence, despite the heavier computational requirement, we use transitions for our system. In Section 4.6, we discuss some possible solutions to reduce the training overhead.

### 4.5.2. COMMUNICATION AT DIFFERENT RANGES

Now, we will compare the performance of SpectraLux at different ranges. For this purpose, we use the same *basic setup* as the prior section, but we change the distance from 1 to 10 meters. A picture of our test setup is shown in Figure 4.11a.

We test three different light intensities at the transmitter: 2 kLux, 40 kLux and 52 kLux. Each one of these light intensities has a minimum and a maximum range. The minimum range is due to saturation effects. Similar to photodiodes and cameras, spectrometers can saturate if the incoming luminous flux is too high. Hence, for each light intensity at the transmitter, we first identify the minimum range that prevents saturation, and then, we increase the range until the BER goes above 1%. In all the experiments we have two settings for the link's data rate: one with 8 symbols, leading to a data rate of 1.13 kbps, and the other with 16 symbols, leading to a data rate of 1.5 kbps. Following the analysis of Section 4.5.1, the symbol period is always kept at 2.6 ms. The packet with $n = 8$ symbols is the same as in the experiment in the previous part. The packet with $n = 16$ symbols contains 278 transitions, including the preamble.

The results for the low and high data rate setups are shown in Figures 4.10c and 4.10d. In passive-VLC, an acceptable BER limit is 1%, which is shown by the horizontal magenta line. To put the light intensities in perspective, a 2 kLux is the illumination observed in well-lit indoor environments, while several tens of thousands lux are more similar to the illumination observed on a clear sunny day. Overall, these results indicate that SpectraLux can achieve acceptable BERs at a few meters range indoors.

### 4.5.3. DIFFERENT LIGHT SOURCES

In these experiments, we consider different light sources: a regular light bulb placed a few meters from the transmitter, and light coming from a sunlight emulator (a complex array of LEDs that emulate the spectrum of the sun). The normalized spectra of these light sources are shown in Figure 4.11b. In all previous experiments, a flashlight was used, whose spectrum is shown in red in Figure 4.11b. For these experiments, we only test the configuration with 8 symbols at 1.13 kbps, and consider three distances: 20 cm, 40 cm and 80 cm. The results are presented in Table 4.4. The most important lesson of this evaluation is that the performance of the system not only depends on the strength of the light intensity (the higher the better) and the width of the spectrum (the wider the better), but also on the radiation pattern of the light source.



| Bit Error Rate (%) | | | | | |
|---|---|---|---|---|---|
| **Light source** | **Lux** | **Pattern** | **20cm** | **40cm** | **80cm** |
| Phone flashlight | 700 | semi-direct | 0.07 | 0.89 | 0.32 |
| Light bulb | 50 | semi-direct | 0.88 | 0.85 | 1.66 |
| Sunlight emulator | 10k | diffused | 0.00 | 0.53 | – |

Table 4.4: BER for different conditions

For any given light intensity, the more collimated (directional & parallel) the light rays are, the longer the range because the luminous flux is contained within a narrower beam [26]. For example, the phone flashlight has a high degree of directionality, and hence, it shows the best performance, with BERs below 1% for all ranges. The light bulb also has a high degree of directionality but due to the lower Lux, it has a higher BER at all distances. The sunlight emulator has the best performance at 20 cm (due to its wide spectrum) but the worst performance at 80 cm[5] because –in spite of providing the highest Lux among the tested light sources– the emulator provides diffused light, which scatters rays in all directions and only a small fraction is picked up by the spectrometer. The same phenomenon is reported in [26], which states that diffused light is the least ideal condition for their passive-VLC platform. With real sunlight on a sunny day, the rays would be highly directional, and hence, we hypothesize that if, similarly to the setup used in [64], we place a mirror at the transmitter (to direct sunlight in a specific direction), the range increases.

### 4.5.4. VARIATION IN LIGHT INTENSITY

In all previous experiments, the light intensity is kept constant during the training and demodulating phases. When using ambient light indoors, we can assume that the intensity does not change significantly, so both the training and communication phases are carried out using the same illumination. *However, this assumption does not hold true in all scenarios.* Under varying lighting conditions, an important question is to assess if the training done with one light intensity is valid to demodulate data at a different light intensity. To test this effect, we select five decreasing intensity levels, labeling them from L1 to L5, and experiment with three different scenarios:

[5] There was no signal present in the link due the diffusion of light.

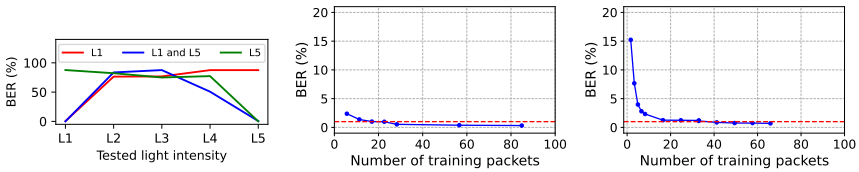


(a) Varying light intensity at 1 meter (b) 1.13 kbps (8 symbols) (c) 1.5 kbps (16 symbols)

Figure 4.12: Amount of data required to train the ML model.

1) We train our model using a combination of L1 and L5, and test it on all light intensities.

2) We repeat experiment (1), but train our model only with the highest intensity (L1).

3) We repeat experiment (1), but train our model only with the lowest intensity (L5).

The result of these experiments is shown in Figure 4.12a. The main outcome of this evaluation is that the training and testing phases have to be done with the same light intensity. When training is done with L1 (red curve), only the testing done at that light intensity has a low BER. When both, L1 and L5 are used for training (blue curve), only those two intensities provide a low BER. This indicates that under different Lux, the wavelengths in the spectrum change in a non-linear manner. Thus, in order to have a reliable link, *the training has to be redone whenever the received light intensity changes.* Hence, we analyze the cost of training the model in the next part.

### 4.5.5. TRAINING OVERHEAD

Until now, we have been using 60 packets to train our model. However, due to the need for retraining, as a result of changing light intensities, it is important to identify the minimum number of training packets required to achieve a low BER during the demodulation process. The effect of the amount of training data on the BER can be seen in Table 4.5. In this experiment, we transmit at a distance of 20 cm with the *basic setup.* The amount of training required for each constellation is summarized in Table 4.5.

| Data rate | Time or Packets | Neural Network |
|---|---|---|
| 1.1 kbps | Packets required | 17 |
| | Time required (s) | 3.4 |
| 1.5 kbps | Packets required | 37 |
| | Time required (s) | 27.2 |

Table 4.5: Training time for BER < 1%

We observe that the convergence time varies with the constellation size (number of symbols). For eight symbols, the system requires 3.4 seconds to transmit 17 training packets, while for 16 symbols, the number of packets and time increase to 37 and 27.2 s respectively. Overall, indoors, the amount of training would not be a major issue because ambient light remains relatively constant.

## 4.6. DISCUSSION

To the best of our knowledge, this work is the first to exploit the spectrum of ambient light for passive communication. By and large, the main challenge in passive-VLC is to increase the data rate. Due to the slow response of LCs, most SoA studies improve the link speed by increasing the complexity of the hardware and/or the modulation method, but while still using the entire spectrum in a monolithic manner. Our approach provides a new perspective to exploit the broad light spectrum. Except for RetroTurbo [34], which uses a large surface with 64 LCs (*multi-pixel* transmitter) and an advanced QAM technique to achieve 8 kbps, all the other *single-pixel* transmitters [42, 32, 44, 64] reach a maximum data rate around 1 kbps. SpectraLux moves the needle for data rates with single-pixel transmitters, but there are several issues to resolve, as discussed next.



### 4.6.1. METHODOLOGY

SpectraLux's methodology has two important points that need to be improved: reducing the complexity of the channel estimation (training phase) and optimizing the symbol selection.

*Channel estimation.* As described in Section 4.3.3, the amount of time required for channel estimation grows quadratically with the number of symbols because if we have $n$ borders (symbols), we need to send $n^2$ transitions during the training phase. If those transitions could be generated via simulations, the training phase would not have to be done in real-time.

To achieve an 'emulated' training system, we want to combine the *static* spectrogram derived in Section 4.1, and the timing properties of the capacitance model, discussed in Section 4.2. The spectral characterization shown in Figure 4.4 captures the portion of the spectrum covered between any two symbols (transitions), but it does not consider that the capacitance effect warps this signal, as depicted in Figures 4.5a and 4.5b. The capacitance model, on the other hand, captures the speed at which this portion is traversed (initially fast and later slow). By combining the static spectrogram and the dynamic capacitance model, we could emulate the required transitions and eliminate the need for transmitting the training packets. The only parameters that we would need are the spectrum of the light source, and the dynamic model of the LC.

We tried this hypothesis with slower types of LCs, called Twisted Nematic (TN) cells, using a second-order constant capacitance model. Figure 4.13a shows the results of this emulation along with the real measurement of the symbol. Visually, the real and empirical transitions look similar, but when SpectraLux decodes packets using the emulated training, the BER increases from less than 2% to 83% (for 8 symbols). This occurs because the constant capacitive approach is not a precise way of modeling LCs. As mentioned in [66, 67], there are more accurate differential equations to describe the transient behavior of LCs. An important next step is to build upon those models to create more precise representations of the transitions.

*Symbol selection.* In Section 4.2, the selection of symbols is equidistant due to the piece-wise linear trends present in parts of the spectrogram. This heuristic, however, is not guaranteed to be optimal. Obtaining the optimal symbols would require an exhaustive search over the entire spectrogram, but we are investigating alternatives to attain near-optimal solutions. Figure 4.13b depicts a symbol selection process using an

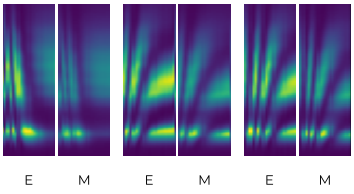


(a) Emulated (E) vs. measured (M) symbols.

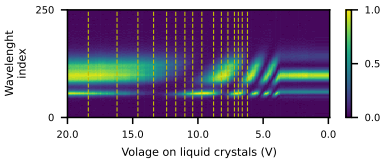


(b) Selected symbols based on K-means clustering.

Figure 4.13: Potential methods of (a) reducing the training overhead using symbol emulation, and (b) optimizing the symbol selection process.

unsupervised K-means clustering algorithm. This approach automatically clusters all the columns in the spectrogram into sixteen different classes and selects the centroid of each class as the representative symbol. We found out, however, that this particular alternative results in a much lower accuracy. For a 16-symbol experiment, the equidistant method provides 98% accuracy, while the clustering approach provides 8%. The poorer performance is due to the fact that the clustering approach does not take the dynamic LC behavior into account.

Overall, we believe that the research community working on passive VLC requires a deeper collaboration with material scientists to understand the transient state of LC cells. Several studies, including ours, exploit in one way or another the transient state of LC cells [33, 32, 44, 64], but without considering in detail the mathematical models and properties reported by the LC research community.

### 4.6.2. TRANSMITTER

Our transmitter requires placing multiple cells in series. This design causes a high level of attenuation that could be avoided if we could design our own cells. To cover a wide spectrum, we need specific values for thickness and birefringence for the LC layer, and this layer would need to be placed between two *glass* electrodes. In our case, we attain the required thickness and birefringence by placing multiple cells together. This means that, instead of using a single pair of glass electrodes, our design has multiple glass panels that attenuate (unnecessarily) the signal intensity. After measuring the attenuation of our LC cells, including the glass and crystal layers, we saw that four cells reduce the light intensity by a factor of 4.4, compared to a factor of 1.1 with a single cell. A custom-made cell would eliminate the attenuation of the redundant glass panels. In addition to decreasing the attenuation, designing a cell enables the transmitter to include a more diverse spectrum, allowing for more symbols and an increase in the SNR.

Another important question is if the communication is affected by slight manufacturing variations among the same model of LC cells. To investigate this, we use 2 different stacks of pi-cells in addition to what was used in Section 4.5. We repeat the spectrum characterization and the communication experiments at 1 m using all three stacks. The results of the characterization are shown in Figure 4.14, and except for the slight variations in the unstable region of low voltages, the patterns look the same. In addition, the BER in all these experiments remained consistent at 0%. This resilience occurs because, even if there are slight manufacturing differences among stacks, they can be accounted

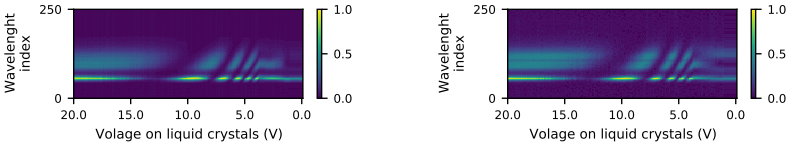


(a) Stack 2

(b) Stack 3

Figure 4.14: Characterization of different stacks of LCs. Apart from the unstable region in low voltages, the patterns are the same.

for during the training period. Thus, replacing LCs of the same model does not pose any problems to the link.

### 4.6.3. RECEIVER REQUIREMENTS

In this paper, the training and demodulation are done on a PC. In case a fully embedded receiver is required, the right microcontroller has to be chosen. The microcontroller should have sufficient clock frequency and RAM to run the decoding operations. Regarding the former, a 2 MHz clock is needed for the spectrometer, as well as an ADC capable of sampling at this rate. This condition is satisfied by most microcontrollers. However, the bottleneck for the demodulation is the available RAM. To determine the memory requirements of the testing (decoding) phase[6], we list the operations in Table 4.6, assuming that all variables are 8-bit integers.

| Operation | Memory (lower-bound) | Size(B) |
|---|---|---|
| Input stream | 250 × 7 (pixels) × 6 (symbols) | 10500 |
| Sobel filter output | Same as input stream | 10500 |
| D(n) signal | 6 (symbols) × 7 (samples) | 42 |
| PCA matrix | 250 × 7 (pixels) × 12 (features) | 21000 |
| NN (input to layer 1) | 12 × 64 (matrix) + 64 (bias) | 832 |
| NN (layer 1 to layer 2) | 64 × 32 (matrix) + 32 (bias) | 2080 |
| NN (layer 2 to output) | 32 × 8 (matrix) + 8 (bias) | 264 |
| Total | | 45218 |

Table 4.6: Memory requirements

We can observe that at least 46 kB of RAM is needed for the demodulation pipeline, without including the code, libraries, and middleware overhead. This amount of memory is available only in middle- to high-end microcontrollers. Hence, it will be important to choose the right low-power microcontroller considering memory limitations or to allow for the addition of off-chip RAM to the receiver's circuitry.

[6]The training phase is done offline

## 4.7. CONCLUSION

In this work, we explored an overlooked property of liquid crystal cells used in passive VLC systems: the idea that these devices can be used as controllable light filters in the spectrum domain. We present a theoretical framework to analyze this property and propose modulation and demodulation methods to create a multi-symbol communication link. By means of exploiting the transitions between symbols, instead of using the symbols themselves, we manage to surpass basic intensity modulation relying on a machine learning approach. Yet limited, this work sheds some light on methods to control ambient light wavelengths, and introduces a novel alternative to the passive VLC community, paving the way towards a more efficient use of the ultra-wide bandwidth of the visible light spectrum with available off-the-shelf devices.

# 5

# PASSIVE MUMIMO

As we saw before, the spectral efficiency of passive VLC is still low. While active transmitters achieve speeds of Mbps and Gbps, LC-based platforms deliver between a few hundred bps [33] up to 8 kbps [34]. Some LCs can reach switching speeds in the order of tens of microseconds [71], however, they are very expensive and not readily available. Most passive transmitters rely on inexpensive LCs with switching speeds between 4 ms and 8 ms, which leads to wireless carriers between 125 Hz and 250 Hz. In Chapters 3 and 4, we proposed two related schemes to increase the data rate of passive platforms. In both of these works, we increased the spectral efficiency of the LC transmitters. Nevertheless, in addition to taking advantage of the complex physics of LCs, it is proven that data rate can be increased by employing MIMO methods, specifically MUMIMO. However, except for a single study that proposes a novel feature space [27], MIMO has not been the technique used to increase the data rate of passive systems. This is a missed opportunity, as a unique advantage of MIMO is multiplying the capacity of a link without requiring more spectrum or faster modulators.

In passive VLC, the use of MIMO is relevant, thanks to the interplay between the *massive amounts of ambient light* in our environments and the *size of light modulating surfaces*. From this perspective, every object that reflects light (e.g. a road sign) or lets the light through (e.g. a window) is a potential transmitter. Considering the small sizes of passive VLC antennas (e.g. photodiodes which are in the order of millimeters), the large reflective and transmissive surfaces in our environments could accommodate massive amounts of antennas to increase their capacity. As shown in Figure 5.1, such MIMO systems could enhance applications proposed in the SoA. For example, for transmissive systems [64], enabling a single channel per LC could allow for windows divided into multiple cells communicating with an indoor device. On the other hand, for reflective systems, bigger road surfaces could be used to obtain more information [32], or the facade of buildings could be transformed into wireless transmitters.

To realize the vast potential of the ambient light in our environments, we need a solid understanding of MIMO. This chapter provides a powerful tool that is still missing in passive-VLC: a principled approach for a MIMO design. Here, we provide a list of the

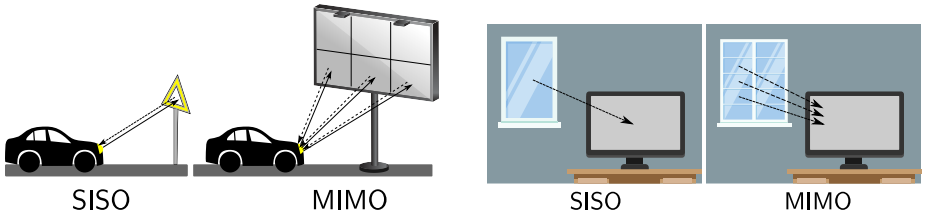


(a) Reflective case (b) Transmissive case

Figure 5.1: Enabling MIMO for passive-VLC would allow the creation of parallel channels. Our framework exploits polarization and color to explore this opportunity.

main contributions of this chapter:

1. **A general MIMO framework for passive-VLC:** In contrast to traditional RF and VLC systems, where MIMO is well-established, there is no such theoretical formulation for passive-VLC. We adapt those principles to suit the unique characteristics of LCs. Our approach has three desirable properties: (i) does not assume orthogonality of the individual channels (overcomes co-channel interference); (ii) can exploit multiple properties of light (polarization and color), and (iii) is agnostic to LC parameters (on which many studies rely).

2. **Efficient multiplexing for different light properties:** Our MIMO system can be used with color, polarization, or both; and the complexity of the channel estimation depends on how these two properties are combined. We develop *flat* and *hierarchical* schemes to optimize the channel estimation and recovery of the signals.

3. **Design of platforms and evaluation:** We build a MIMO platform, where we show that the link capacity increases almost linearly even with co-channel interference. We test our mathematical approach with two types of LCs. Using the simplest modulation method in the SoA and LCs with switching speeds comparable to other platforms, our system achieves up to 6.8 kbps with 9 cells.

## 5.1. THEORETICAL MODEL

Our framework builds upon the basics of MIMO, which is widely used in RF. Here, we adapt it to the particular characteristics of passive VLC. We first start with a simple SISO model and then extend it to MIMO.

### 5.1.1. SINGLE TRANSMITTER AND RECEIVER

To begin with the simplest case, we discuss an LC-based SISO link consisting of one transmitter and one receiver. In Section 2.1, we showed the light-switching property of LC cells, and how they change from opaque to transparent based on their voltage. To ease building our argument, we abstract this property with a transfer function $S(t)$. $S(t)$ represents how much a cell attenuates the light when the voltage on the LC cells (v(t))

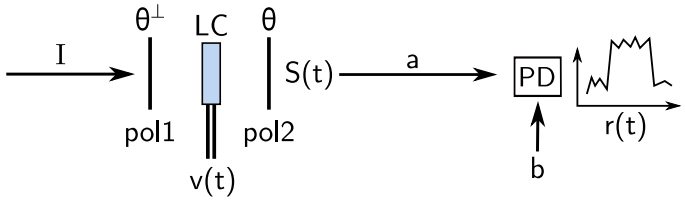


Figure 5.2: The basic SISO link with two polarizers.

changes, as shown in Figure 5.2. In rigorous terms, $S$ is a function of v(t), however, we denoted as $S(t)$ to facilitate the notation.

In a SISO link, the transmitted data is embedded into the optical signal $S(t)$, and the aim of the link is to recover the transmitted bits from it. To model how $S(t)$ looks in the receiver, we recap the effects of each LC component, as described in Section 2.1:

1. **First polarizer (pol1) with the angle $\theta^{\perp}$:** Following Malus' law[1], the intensity of *unpolarized* light is halved after passing through a polarizer, regardless of the polarizer's angle. In addition, the polarization of the light exiting this layer is equal to $\theta^{\perp}$. So, if the input light is unpolarized with intensity I, the exiting light will be $\theta^{\perp}$-polarized with intensity 0.5I.

2. **Liquid crystal layer:** The LC layer changes the polarization of the input light as a function of the voltage v(t). We model this polarization change with $\Theta(v(t))$. In off-the-shelf cells, the range of $\Theta(v(t))$ is [0°,90°]. After this LC layer, the polarization angle of the light is $\theta^{\perp}+\Theta(v(t))$. In a SISO link, the transmitter modulates v(t), and in turn, the light's polarization is modulated to carry the information bits. Keeping this in mind, we omit v(.) from our notation and use $\Theta(t)$ for brevity.

3. **Effect of the analyzer (pol2) with the angle $\theta^{\perp}=\theta+90°$:** This polarizer sits in the light path after the LC layer, and is perpendicular to the first polarizer. Malus' law states that the light undergoes an attenuation of $\cos^2(\theta^{\perp}+\Theta(t)-\theta)$ after crossing the second polarizer. Also, $\theta^{\perp}-\theta$ is equal to 90°, so, this expression reduces to $\sin^2(\Theta(t))$.

To summarize the steps above, the two polarizers and liquid crystal layer attenuate an incoming light with the transfer function shown below:

$$S(t) = 0.5\ \sin^2(\Theta(t)) \tag{5.1}$$

In addition, this attenuated light is $\theta$-polarized.

As the signal $I\ S(t)$ travels towards the receiver, it is further attenuated by a factor $a$ due to its travelling distance. Then, the receiver detects this signal plus some bias from other sources denoted by $b$. The received signal $r(t)$ is given by:

$$r(t) = I\ a\ S(t) + b \tag{5.2}$$

[1] Malus' law states that the amount of polarized light passing through a polarizer is dictated by the following cosine rule $I_o = I_i Cos^2(\Delta\theta)$, where $I_i$ is the incoming light, $I_o$ is the outgoing light, and $\Delta\theta$ is the angle difference between the polarizer and the polarized light.

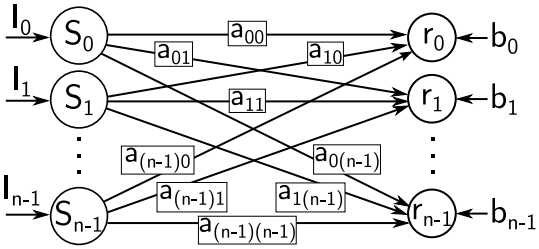


Figure 5.3: A MIMO configuration.

The final aim is to retrieve $S(t)$. In a SISO link, $S(t)$ is found by solving Equation 5.2. However, with MIMO sub-channels, new terms will appear in this equation due to the interference from other transmitters. In the next section, we generalize this configuration to have multiple transmitters, and after that, we describe novel methods to reduce the inter-channel interference to obtain an operational MIMO system.

5

### 5.1.2. MULTIPLE TRANSMITTERS AND RECEIVERS

As a corollary to Figure 5.2, we introduce the configuration in Figure 5.3, where there are an equal number of $n$ transmitters and receivers. The transmitter $i$ modulates the intensity of its input light ($I_i$) with the transfer function $S_i(t)$. In addition, the attenuation of the light going from transmitter $i$ to receiver $j$ is $a_{ij}$. For brevity, we replace $I_i\ a_{ij}$ with $\hat{a}_{ij}$. Thus, in Figure 5.3, the signal at the $i$*th* receiver is calculated by:

$$r_j = \sum_{i=0}^{n-1} \hat{a}_{ij} S_i + b_j \tag{5.3}$$

or in a matrix form for all receivers:

$$\begin{bmatrix} r_0 \\ r_1 \\ \dots \\ r_{n-1} \end{bmatrix} = \begin{bmatrix} \hat{a}_{00} & \dots & \hat{a}_{n-1,0} \\ \hat{a}_{01} & \dots & \hat{a}_{n-1,1} \\ \dots & & \\ \hat{a}_{0,n-1} & \dots & \hat{a}_{n-1,n-1} \end{bmatrix} \begin{bmatrix} S_0 \\ S_1 \\ \dots \\ S_{n-1} \end{bmatrix} + \begin{bmatrix} b_0 \\ b_1 \\ \dots \\ b_{n-1} \end{bmatrix} \tag{5.4}$$

This model captures a system of linear equations, where the rectangular matrix is called the channel matrix, and the aim is to solve for the vector $S$.

*This system has a unique solution only if the channel matrix is non-singular, but creating a non-singular channel matrix is an open challenge in passive-VLC.* With *radio* backscattering (passive RF), the precise control of amplitude, frequency, and phase enables orthogonal (perfect non-overlapping) channels using various domains, such as frequency and coding [72, 73, 74]. LCs, on the other hand, only have a coarse non-linear output between two states, preventing them from employing these techniques.

There is only one passive-VLC study performing MIMO [27], which motivates our work and exposes the above challenge. However, it does not provide mathematical guarantees for a solution, nor does it try to tune the channel to obtain a non-singular matrix. As a result, it employs a MIMO system with high interference, resulting in rank-deficient channel matrices. Hence, *the key questions are whether it is possible to design a passive*

*MIMO system with non-singular matrices, and if so, what is the best way to do it?* In the following subsections, we investigate these questions.

### 5.1.3. PASSIVE-VLC AND MIMO

To make the channel matrix non-singular, we need a careful analysis of its coefficients to reduce interference. To achieve that, we exploit two properties of light: polarization and color. Understanding the relation between these parameters and the coefficients is key to designing a MIMO channel. Here, we explain this relation, and in Section 5.3, we investigate practical steps for their implementation.

#### POLARIZATION

Following Section 5.1.1, the LCs in our model radiate $\theta$-polarized light. *A key insight of our work is to show that, in addition to the default two polarizers mentioned before, adding a third polarizer to each receiver reduces sub-channel interference significantly.* In this part, we explain this concept by showing the effect of the third polarizer in three cases: *a)* in a SISO channel, to demonstrate how the third polarizer affects the signal attenuation; *b)* in a MIMO channel with two sub-channels, and *c)* with several sub-channels, to demonstrate how the signals can be recovered despite interference. Overall, our approach provides a simple and effective solution to achieve MIMO with polarization.

***a) A SISO channel:*** Consider the setup in Figure 5.4 with three polarizers, the light coming out of the second polarizer (pol2) has an intensity of $\hat{a}S(t)$ and a polarization of $\theta$. If the third polarizer (pol3) is placed at angle $\beta$, the light faces a new attenuation factor equal to $cos^2(\theta-\beta)$. In total, the signal reaching the photodiode becomes:

$$r(t) = \hat{a}\ S(t)\cos^2(\theta-\beta) + b \tag{5.5}$$

where $\hat{a} = I\ a$, and $b$ includes the effective DC bias and interference measured by the receiver. If the transmitter and receiver are aligned, i.e. $\theta = \beta$, the signal strength is maximized. In this case, the SNR is higher than the case with 2 polarizers, as the intensity of other interference sources ($b$) is lowered by 0.5x thanks to the third polarizer. The expert reader could argue that there is no advantage in adding a third polarizer, instead, the second polarizer could have been removed from the LC and placed on the receiver's PD, as was done by some previous works [64, 27]. However, we will see that the benefit appears when multiple transmitters are used.

***b) A MIMO link with two orthogonal sub-channels:*** Suppose there are two channels indexed 0 and 1, both having the configuration shown in Figure 5.4, but with different polarization angles. Channel 0 has the polarizations $pol2 = pol3 = \gamma$, and channel 1 has $pol2 = pol3 = \gamma^{\perp}$ (perpendicular to $\gamma$). The light reaching each receiver is the sum of the lights from both transmitters. So, the received signal in channel 0 is:

$$\begin{aligned} r_0^{3pol}(t) &= \hat{a}_{00}\ S_0(t)\cos^2(\gamma-\gamma) + \\ &\quad \hat{a}_{10}\ S_1(t)\cos^2(\gamma^{\perp}-\gamma)\ + b_0 \\ &= \hat{a}_{00}\ S_0(t) + b \end{aligned} \tag{5.6}$$

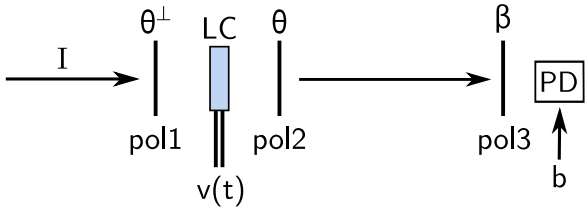


Figure 5.4: A SISO link with three polarizers

It turns out that $r_0$ only captures transmitter 0, and vice versa. This occurs because the first cosine term maintains the intended signal, as in the SISO case, but the second cosine term eliminates the interference of $S_1$. Note that *using a third polarizer creates two orthogonal channels*, with the SNR of each MIMO sub-channel being *at least* equal to the SISO channel[2] (Equation 5.2). If each sub-channel used only two polarizers, pol1 and pol2, the signal received by channel 0 would still contain the interference from channel 1.

$$r_i^{2pol}(t) = \hat{a}_{00}\, S_0(t) + \hat{a}_{10}\, S_1(t) + b$$

Intuitively, our approach creates two independent channels by forcing single polarization directions that are orthogonal. Next, we generalize this concept for more channels and expose its limitations.

***c) A MIMO link with several sub-channels:*** Having more than two sub-channels means that the polarization angles can no longer be mutually orthogonal. That is, there will be interference. However, using *pol3* allows for reducing the interference, which leads to non-singular matrices if carefully designed. The key intuition in the most general case is as follows: without *pol3*, the received signals are shown by Equation 5.3, and adding pol3 multiplies the receiver signal by $cos^2(\theta_k - \beta_i)$. Considering the signals from all $n$ transmitters to receiver $i$, the effect of *pol3* leads to

$$r_i = \sum_{k=0}^{n-1} \hat{a}_{ki} S_k(t) cos^2(\theta_k - \beta_i) + b_i \tag{5.7}$$

These new cosine terms will also appear in the channel matrix of Equation 5.4, resulting in a new degree of freedom that affects the channel matrix and its non-singularity. Two important questions are how to determine the maximum number of separable channels, and how the selection of $\theta$s and $\beta$s affects the link. We tackle these questions in the next section.

### COLOR

Ambient light contains multiple colors. The most relevant study in this domain uses multiple LCs in series to send different colors as symbols and decodes the information with a spectrometer [75]. This approach, however, uses the entire bandwidth as a single multi-color channel instead of decomposing it into multiple parallel channels, limiting

[2]We state 'at least' as the noise and other ambient interference is lowered by 0.5 by the third polarizer.

the data rate to around 1 kbps after using a demanding training process with machine learning methods.

For MIMO, we can partition the spectrum using color filters. Placing different color filters in front of each LC and PD can result in an invertible channel matrix if the colors are *properly* chosen. In the sections, we provide a thorough analysis of color filters. Similar to polarization multiplexing, we do not assume a full separation between color bands, i.e. the color channels can overlap. In addition, we will show that the *polarization* and *color* approaches can be combined in a hierarchical manner, allowing for even more multiplexed channels without substantially increasing the interference.

### 5.1.4. SIGNAL QUALITY

Up to here, we have looked into methods that can make the channel matrix invertible to guarantee a solution for Equation 5.4. However, this does not promise a *good enough* separation between sub-channels. To have a metric showing the signal separation among transmitters, we use the *condition number* of the MIMO channel, as is used in traditional RF communications. The condition number is defined by the equation below:

$$\text{cond} = |\frac{\lambda_{max}}{\lambda_{min}}| \tag{5.8}$$

where $\lambda_{max}$ and $\lambda_{min}$ are the maximum and minimum eigenvalues of the channel matrix. A condition number ranges from 1 to infinity, with lower numbers showing less interference between the channels. In the Section 5.2, we discuss how polarization and color affect the channel's condition number, as well as ways to select the *best* combination of parameters to obtain a low condition number.

## 5.2. PASSIVE MIMO CHANNEL

After formalizing a model for a passive MIMO link, we now tackle the implementation challenges by answering two questions: first, how can the passive MIMO channel be practically estimated? second, what are the conditions, performance, and limitations of using polarization and color to make multiplexed channels?

### 5.2.1. CHANNEL ESTIMATION

In the MIMO system of Figure 5.3, the photodiodes measure superimposed and attenuated signals coming out of each transmitter ($S_i$). These signals can be recovered from $r_i$s only if the receiver knows the channel matrix as well as the bias values $b_i$. In this section, we present a way to obtain those parameters. To achieve that, a custom-designed preamble is sent by the transmitters to perform the channel estimation process. Below, it is explained how to form such preamble.

#### A PREAMBLE FOR CHANNEL ESTIMATION

The channel matrix has $n^2$ variables $\hat{a}_{ij}$ and $n$ variables $b_i$. To solve this system, we send a known preamble of length $n$+2. A sample preamble is shown in Figure 5.5, where $S_i = 1$ means that the $i$th transmitter is set to its transparent state, and vice versa. Following the figure's timeline, the steps taken to form the preamble are:

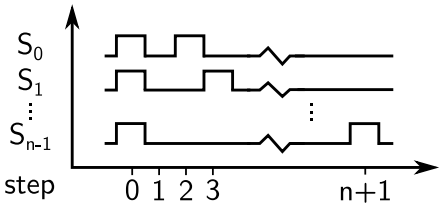


Figure 5.5: The preamble of our MIMO system.

step 0: all $S_i$s are set to 1. This is used only to mark the start of a preamble. It has no significance in the channel estimation.

step 1: all $S_i$s are set to 0. Following Equation 5.4, the values of $b_i$s are calculated in this step by setting $b_i = r_i$.

steps 2 to n+1: in each of these steps, only one of the transmitters is set to 1, and all other $S_i$s are set to 0. In addition, no transmitter is set to 1 more than once. Each step results in $n$ equations, and since there are n steps (2 to n+1), there are $n^2$ equations to solve the channel matrix.

5

After solving Equation 5.4, we have to make sure that the channel matrix is non-singular. We also need a low-condition number to maintain enough distance between channels. Next, we describe how an arrangement of polarization and color filters defines the channel matrix, and we investigate the conditions to have a recoverable MIMO channel.

### 5.2.2. POLARIZATION MULTIPLEXING

Our approach using three polarizers enables more parallel channels, but there is an upper limit to the number of channels that can be multiplexed. We first find this upper limit, and then, we run a simulation based on our model to find the configuration with the lowest condition numbers.

Considering transmitter $i$ and receiver $j$ in a multi-channel platform, let us denote $p_{ij}$ as the attenuation caused by the third polarizer at the receiver (pol3 of Figure 5.4), that is $p_{ij} = \cos^2(\theta_i - \beta_j)$. As a result, the channel matrix has to be updated to:

$$H = \begin{bmatrix} \hat{a}_{00}\,p_{00} & \cdots & \hat{a}_{(n-1)0}\,p_{(n-1)0} \\ \hat{a}_{01}\,p_{01} & \cdots & \hat{a}_{(n-1)1}\,p_{(n-1)1} \\ \cdots & & \\ \hat{a}_{0(n-1)}\,p_{0(n-1)} & \cdots & \hat{a}_{(n-1)(n-1)}\,p_{(n-1)(n-1)} \end{bmatrix} \tag{5.9}$$

In addition, in our scenario where MIMO is used to increase the data rate, we can assume that all sub-channels come from adjacent transmitters (a single transmitter with multiple LCs), resulting in all $a_{ij}$s (the attenuation due to distance) to have the same value of $a$. In this case, elements of column $i$ will be of the form $I_i\ a\ p_{ij}$. Thus, the matrix

above can be written as:

$$H = a^{n^2} \begin{bmatrix} I_0 p_{00} & \dots & I_{n-1} p_{(n-1)0} \\ \dots & & \\ I_0 p_{0(n-1)} & \dots & I_{n-1} p_{(n-1)(n-1)} \end{bmatrix} \tag{5.10}$$

To see if this matrix is invertible, we have to find its determinant. One can prove that for $n \geq 4$ the determinant is zero[3] regardless of the values of $\theta$ and $\beta$. This means that with this approach, a maximum of 3 channels can be polarization-multiplexed without making the channel matrix singular. In addition, for $n \leq 3$, the matrix is invertible even if $\theta_i$ (at the transmitter) and the corresponding $\beta_i$ (at the receiver) are different. In Section 5.1.3, $\theta_i$ and $\beta_i$ were set to the same angle for the 2-channel example to clarify the idea. In practice, this is not necessary, which has a strong advantage in a real implementation because it means that the polarizers at the transmitter and receiver do not need to be perfectly aligned. The only condition to guarantee that the matrix is invertible is that no two $\theta_i$s or two $\beta_j$s are the same.

### MAXIMIZING CHANNEL SEPARATION

Non-singularity is a necessary but not sufficient condition to have a working MIMO channel. The channel matrix must also have a sufficiently low condition number to reduce inter-channel interference. To identify the angles that minimize the *condition number*, we resort to numerical analysis. The analysis has two steps, first, we identify the lowest condition number for two channels and then, we minimize the condition number once the third transmitter is added.

For two transmitters, setting one set of angles to 0° ($\theta_0 = \beta_0 = 0°$) and the other set to 90° ($\theta_1 = \beta_1 = 90°$) leads to the following diagonal channel matrix, i.e. a (perfect) orthogonal channel:

$$H = a^2 \begin{bmatrix} I_0 & 0 \\ 0 & I_1 \end{bmatrix} \tag{5.11}$$

In this case, the condition number is $\frac{max(I_0,I_1)}{min(I_0,I_1)}$, which has the lowest possible value of 1 if $I_0 = I_1$. This analysis proves the derivation given in Section 5.1.3 for the (perfect) orthogonality of the dual channel with three polarizers.

For 3 transmitters and receivers, we keep the 0° and 90° angles, and add a third angle $\theta_2 = \beta_2 = x$. The variable $x$ is swept from 0° to 90°, and the resulting condition number of the 3×3 channel matrix is shown in Figure 5.6a. In this Figure, the minimum condition number (5.83) happens when x = 45°. Hence, for a 3-channel MIMO, the angles need to be 0, 45 and 90 degrees. To put the condition number in perspective, we found that in our system, values below 10 lead to a tolerable amount of interference. Such reduction of interference has a major impact on modulation: compared to the SoA studies, which have proposed increasingly complex modulation methods to increase the data rate, our quasi-orthogonal channels allow the use of the simplest modulation method (OOK) in a reliable manner, and the only trade-off is adding inexpensive (few cents) polarizing sheets and more photodiodes to the receivers.

[3] We used Wolfram Alpha for the proof.

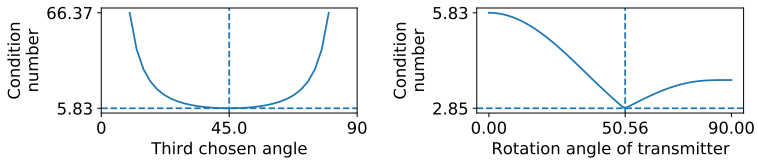


(a) When three LCs are used: two fixed at 0° and 90°, and the third angle sweeps from 0° to 90°.

(b) When there are three channels (0°, 45°, 90°) and the roll angle sweeps from 0° to 90°.

Figure 5.6: Analysis of condition numbers

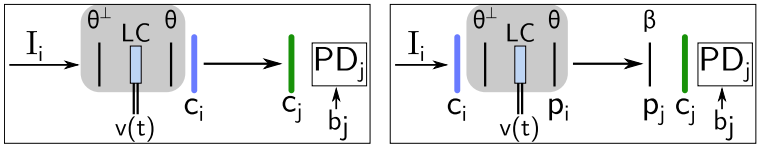


(a) A Tx-Rx pair using only color

(b) A Tx-Rx pair using both polarization and color.

Figure 5.7: Tx-Rx models using color and polarization.

5

#### ROLL ROTATIONS AND CONDITION NUMBER

In the method above, we assume that the transmitters and receivers are aligned, that is, there is no rotation in the roll axis. However, in real scenarios, the receiver may not always be placed in a position that is aligned with the transmitter, so we have to investigate the sensitivity of the link to rotations. To find this out, we add an offset $\beta_r$ to the polarizers in the receiver. So, the polarizing angles of the transmitter are $\theta_0 = 0°$, $\theta_1 = 45°$, and $\theta_2 = 90°$, and the angles of the receiver are $\beta_0 = \beta_r$, $\beta_0 = 45° + \beta_r$, and $\beta_0 = 90° + \beta_r$. Next, we sweep $\beta_r$ from 0° to 90°, and the condition numbers are calculated at each step. The result of this analysis is shown in Figure 5.6b, which shows that roll rotations have no detrimental effects, as the condition number always stays below 5.83. In fact, a roll of about 50° provides the best performance. In our evaluation, we observed that with condition numbers below 5, we can obtain links with zero or close to zero bit-error rate (BER), thus, a misalignment in the roll axis does not impact our system.

### 5.2.3. COLOR MULTIPLEXING

As stated before, the bandwidth of visible light is wide. To use the bandwidth more efficiently, we can multiplex channels using color filters. In that case, the same principle applies as with polarization: the color channels do not need to be orthogonal, and can have an overlap as long as the channel matrix has a sufficiently small condition number. To analyze the color domain, we follow the same procedure as with polarization, and find the best color filters for MIMO.

#### CHANNEL DERIVATION

We have shown that channel multiplexing requires adjusting the elements of the channel matrix. To describe our approach with colors, let us consider the Tx-Rx pair shown in Figure 5.7a. The transmitter consists of an LC cell, shown by the gray box, and a color filter afterward. The LC attenuates the input light by a factor of S(t) (Equation 5.1) and the

| 2-color | 3-color | 4-color |
|---|---|---|
| (r,b):1.13 | (r,g,b):4.79 | (b,g,lp,dp):14.91 |
| (r,c):1.85 | (b,g,dp):5.88 | (r,g,v,lp):16.93 |
| (r,g):1.88 | (r,g,v):7.10 | (r,g,b,lp):19.08 |

Table 5.1: Condition numbers for "n" color filters (r:red, b:blue, c:cyan, g:green, v:violet, lp:light pink, dp:dark pink)

color filter exerts an attenuation $c_i$, which is dependent on the filter's spectrum. Next, the signal travels to the receiver, where it encounters another color filter (green) with attenuation factor $c_j$. If the spectrum of the filters at the transmitter and receiver match, then $c_j = 1$. Combining the effects of the color filters, the signal is attenuated by the factor $c_{ij}$. This means that each pair of color filters makes for a unique attenuation factor, and this characteristic makes it possible to build a MIMO channel. Contrary to the polarization case, where the transfer function $S(t)$ is attenuated by the cosine functions; for the color case, $S(t)$ is attenuated by the factor $c_{ij}$, which leads to the following channel matrix:

$$H = \begin{bmatrix} \hat{a}_{00}c_{00} & \dots & \hat{a}_{(n-1)0}c_{(n-1)0} \\ \dots & \dots & \dots \\ \hat{a}_{0(n-1)}c_{0(n-1)} & \dots & \hat{a}_{(n-1)(n-1)}c_{(n-1)(n-1)} \end{bmatrix} \tag{5.12}$$

In the next part, we analyze these coefficients for different color filters to identify the best combination.

### COLOR SELECTION

The color selection could be done with a numerical analysis, similar to the polarization case, but this requires knowing the spectral response of the color filters. The filters that we use, however, are inexpensive, a few cents per receiver, and they do not have a datasheet. Hence, we pursue the following empirical approach.

*1) Benchmark all color filters*: We use a set of 10 filters: red, green, blue, cyan, light pink, dark pink, orange, lime, yellow, violet. First, we build a testbed with 10 LCs and 10 photodiodes, each channel masked with a different color filter. Then, we follow the preamble mechanism presented in Section 5.2.1, where each transmitter is activated only once, while the others remain off. This approach permits obtaining the elements $c_{ij}$ for all pair-wise color combinations, and hence, building a complete channel matrix.

*2) Iterate the design space:* Based on the channel matrix, we can build sub-matrices to obtain any $m$-combination of colors, with $m$ ranging from 2 to 10. For each combination, we use the columns and rows corresponding to the selected colors.

*3) Find the optimum solution*: We calculate the condition numbers for all the combinations to identify the maximum number of channels we can obtain and the best filters to use.

Following the above steps, we identify that using 4 color channels already provides condition numbers close to 15 or higher, which means that the maximum number of channels that we can reliably use is three. Table 5.1 shows that the best color combination for two channels is red and blue; this mixture provides an almost orthogonal channel with a condition number of 1.13. For a 3-color channel, the best combination is red,

green, and blue, providing a condition number of 4.8, which is close to the condition number using three polarization-multiplexed channels.

Overall, our polarization and color analysis show that we can use three reliable channels in each domain. In the next section, we show how these two domains can be combined.

## 5.3. DESIGNING A PRACTICAL CHANNEL

In this section, we propose practical modulation methods using the derivations of the previous sections. We will show that, depending on the configuration of the transmitter, two modulation methods can be applied: *flat* or *hierarchical*.

### 5.3.1. A MULTI-LAYERED CHANNEL

Polarization and color are independent characteristics of light, which hints at the possibility of their simultaneous use to increase channel capacity. A platform with $m$ colors and $n$ polarizations can multiplex $m \times n$ channels. One Tx-Rx pair of such channel is shown in Figure 5.7b, where the (color, polarization) pair for the transmitter is denoted as $(c_i, p_i)$, and for the receiver as $(c_j, p_j)$. Following the analysis of Section 5.2, we consider 3 polarizations (0°, 45°, 90°), and 3 colors (red, green, and blue) to build a maximum of 9 channels.

To make a MIMO channel with the mentioned properties, we propose two approaches: *flat*, and *hierarchical*. The latter results in better channel separation, but it can only be used if both color and polarization are used. To avoid over-complicating our example, we will discuss the case of 2 polarizations ($p_0$ and $p_1$) and 2 colors ($c_0$ and $c_1$), although we can extend it to a higher number of colors and polarizations.

### 5.3.2. COMMUNICATION SYSTEM

In our example with four transmitters and receivers, each Tx-Rx pair has a unique $p_{ij}c_{ij}$ combination, as shown in Figure 5.8a. To estimate the channel matrix, proper preambles have to be designed. Next, we explain the difference between the *flat* and *hierarchical* preambles.

#### "FLAT" MODULATION

In this approach, the preamble is constructed in the same way as the case with only polarization or color multiplexing, which was explained in Section 5.2.1. Here, we quickly recap the steps. As shown in Figure 5.8b, first, all the transmitters send a '1' (to mark the start), then, all transmit a '0' (to obtain the bias $b_i$), and finally, each transmitter sends a '1' in a round-robin fashion to solve the $n \times n$ channel matrix (in this case $n = 4$).

#### "HIERARCHICAL" MODULATION

When colors and polarizations are used jointly, the channel can be demultiplexed in two steps. First, the channel is considered to be only color-multiplexed, and then, only polarization-multiplexed. This approach has several advantages compared to the *flat* mode, as we discuss later. But before that, we modify the mathematics of Section 5.1 to model the hierarchical approach.

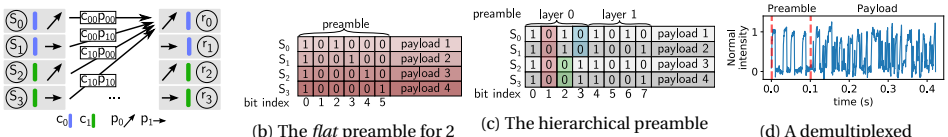


(a) Setup combining colors and polarizers.

(b) The *flat* preamble for 2 polarizations and 2 colors

(c) The hierarchical preamble for Figure 5.8a. Red shows when all $S'_i$s are zero, green when $S'_1 = S'_3 = 0$, and blue when $S'_0 = S'_2 = 0$.

(d) A demultiplexed sub-channel from 9 Tx-Rx pairs. The symbol periods of the preamble and payload are 10 and 1 ms.

Figure 5.8: Combination of polarization and color: setup and preambles

Considering the example of two polarizations and two colors in Figure 5.8a, the equations obtained for the receivers are:

$$\begin{aligned} r_0 &= c_{00}(S_0 p_{00} + S_1 p_{10}) + c_{10}(S_2 p_{00} + S_3 p_{10}) + b_0 \\ r_1 &= c_{00}(S_0 p_{01} + S_1 p_{11}) + c_{10}(S_2 p_{01} + S_3 p_{11}) + b_1 \end{aligned} \tag{5.13}$$

and

$$\begin{aligned} r_2 &= c_{01}(S_0 p_{00} + S_1 p_{10}) + c_{11}(S_2 p_{00} + S_3 p_{10}) + b_2 \\ r_3 &= c_{01}(S_0 p_{01} + S_1 p_{11}) + c_{11}(S_2 p_{01} + S_3 p_{11}) + b_3 \end{aligned} \tag{5.14}$$

If we rename the expressions inside the parentheses to

$$\begin{aligned} S'_0 &= S_0 p_{00} + S_1 p_{10} \qquad & S'_1 &= S_2 p_{00} + S_3 p_{10} \\ S'_2 &= S_0 p_{01} + S_1 p_{11} \qquad & S'_3 &= S_2 p_{01} + S_3 p_{11} \end{aligned} \tag{5.15}$$

We observe that the *polarization matrix* $\begin{bmatrix} p_{00} & p_{10} \\ p_{01} & p_{11} \end{bmatrix}$ is the only one appearing, but solving it requires knowing the values of $S'_i$. To obtain those values, we can re-arrange the receivers in Equation 5.13 Equation 5.14 to:

$$\begin{aligned} r_0 &= c_{00} S'_0 + c_{10} S'_1 + b_0 \qquad & r_1 &= c_{00} S'_2 + c_{10} S'_3 + b_1 \\ r_2 &= c_{01} S'_0 + c_{11} S'_1 + b_2 \qquad & r_3 &= c_{01} S'_2 + c_{11} S'_3 + b_3 \end{aligned} \tag{5.16}$$

This formulation only exposes the *color matrix* $\begin{bmatrix} c_{00} & c_{10} \\ c_{01} & c_{11} \end{bmatrix}$. If the transmitter activates only $S'_0$ and $S'_2$ in one cycle (blue filter), and only $S'_1$ and $S'_3$ in the next cycle (green filter), the system can obtain all of the color coefficients $c_{ij}$, and in turn all $S'_i$s. Then, with the values of $S'_i$s, the system could first activate only one polarization direction ($S_0$ and $S_2$), and then other direction ($S_1$ and $S_3$) to obtain all the coefficients $p_{ij}$. This approach would result in solving two *flat* 2×2 matrices instead of solving a 4×4 matrix. Next we explain how we design a preamble to activate the $S'_i$ variables as desired.

### FORMING A HIERARCHICAL PREAMBLE

Considering the example with two polarizations and colors, the corresponding hierarchical preamble is shown in Figure 5.8c. Below, we describe how it is generated.

*step 1 & 2)* Similar to the flat case, first, all transmitters send '1' to mark the beginning. Then, all transmitters send '0' to obtain the bias $b_i$.

*step 3)* To obtain the coefficients of the first hierarchical layer (color in our example), we need to generate the signals $S'_i$ in Equation 5.16 that turn on one color channel at a time. To achieve that, we first set $S_2$ and $S_3$ to 0 to turn off the green channel (highlighted in Figure 5.8c), and then we set $S_0$ and $S_1$ to 0 to turn off the blue channel. This operation leads to a *flat* 2×2 matrix where the $c_{ij}$ coefficients can be derived.
*step 4)* To mark the beginning of the second layer, we repeat steps 1 and 2 (all Tx are first on and then off).
*step 5)* To obtain the polarization coefficients, we need to generate the $S'_i$s that turn on one polarization direction at a time in Equation 5.15. To achieve that, we first turn off $S_1$ and $S_3$, and then we turn off $S_0$ and $S_2$. This operation leads to a *flat* 2x2 matrix where the $p_{ij}$ coefficients can be derived.

#### COMPARING THE HIERARCHICAL AND FLAT APPROACHES

The advantages of the hierarchical configuration are discussed in three domains: preamble length, computational complexity, and SNR. Our comparison below assumes $m$ polarizations and $n$ colors, resulting in $m \times n$ parallel channels.

***1) Preamble lengths:*** In a flat approach, the preamble has a length equal to the number of parallel channels plus two signaling bits, which leads to $m \times n + 2$ bits. In the hierarchical approach, the preamble has a length of $m + n + 4$ bits, thanks to the grouping of channels and their parallel calculations. Hence, the hierarchical approach is more efficient in terms of its preamble length.

***2) Computational intensity:*** In both methods, the computation-intensive operations are matrix inversion and multiplication. In the flat approach, we need the inverse of an $m \times n$ matrix, which takes $(mn)^3$ operations. In addition, a matrix-vector multiplication is needed for each data sample, which is proportional to $(nm)^2$ operations. On the other hand, in a hierarchical setup, there are two steps. In the first step, there is an $m \times m$ matrix, and in the next step an $n \times n$ matrix (or vice versa, depending on the design). This results in a total of $m^3 + n^3$ operations for matrix inversion. In addition, for matrix multiplications the system needs $m \times n^2 + n \times m^2 = mn(m+n)$ operations. If $m = n$, we see that the hierarchical approach (with complexity $4m^3$) is significantly more efficient that the flat approach (with complexity $m^6 + m^4$).

***3) Signal quality:*** With the hierarchical approach, fewer number of parallel channels have to be considered at each demultiplexing step. In Section 5.5, we will empirically show that the hierarchical approach yields a lower condition number, resulting in a higher SNR.

### 5.3.3. MODULATION & DEMODULATION

Up to here, we only considered the demultiplexing of sub-channels. In addition to being multiplexed, the signals have to be modulated before transmission, which is explained below.

### MODULATION

Each transmitted packet has only two fields, preamble and payload, and they are modulated in different ways:

**Preamble:** In the preamble, the most important requirement is to obtain accurate coefficients for polarization and color. Due to this reason, when an LC cell changes its state, we let it run until it reaches its plateau. An example is shown in Figure 5.8d, which shows one of the sub-channels in a MIMO system with 9 sub-channels. For this LC, we wait 10 ms for each preamble bit, so that both the slow behaviour of LCs and the triggering jitter between different LCs are overcome. For this link with 9 sub-channels, the total preamble time is 100 ms (there are 10 bits in the preamble: 3 colors, 3 polarizations, plus 4 bits of '1' and '0').

It is important to note that the preamble does not need to be transmitted again for different light intensities. Our demultiplexing method uses relative values of the preamble, so, when the light intensity changes, it is similar to multiplying the channel matrix by a fixed factor, which causes the demultiplexed data to be scaled and shifted by a constant value. If a link is designed without sending the full preamble before every packet, it still has to send the preamble's first bit (all LCs on) for two reasons: a) to mark the start of a payload, and b) to provide a reference to normalize the payload signal after demultiplexing. This normalization allows the use of demodulation thresholds obtained with preambles at different light intensities.



**Payload:** Once the preamble is sent, the requirement of the system changes to increasing the data rate. The transmitter does not need to wait for a full contrast (plateau); so long as a signal is above a given threshold, the symbol can be deemed a '1'. Since our framework reduces co-channel interference significantly, we can rely on this basic thresholding strategy, and use it with the simple modulation method of OOK. For the LC in Figure 5.8d, which has a fall time of 0.7 ms and a rise time of 2.5 ms, a bit period of 1 ms (1 kbps) was enough to provide signals with sufficient peak height.

**Clock transmission.** As seen above, the duration of bits in the preamble (10 ms) are longer than the bits in the payload (1 ms). This means that if the payload is not long enough, the data rate drops due to the significant time allocated to the preamble. Hence, the payload's length must be long to amortize the preamble's effect. Thus, in our evaluation, we fit from 300 to 1000 bits in one payload. This poses another risk: since OOK does not have embedded synchronization, as the payload gets longer, the demodulation becomes susceptible to clock recovery failures. Using an encoding mechanism such as Manchester is not favourable either, as it reduces the data rate by a factor of 0.5. To overcome this, we used channel 0 to transmit the data clock. This channel has repetitive data, thus reaches a steady state very fast. In that manner, the clock peaks are at the same height, and can be found with a simple peak-finding algorithm. Using a channel for clock transmission is a simple technique but it was not used in any prior passive-VLC study. In our case, this design makes sense because we have nine channels and it is not a significant overhead to use one of them as a clock.

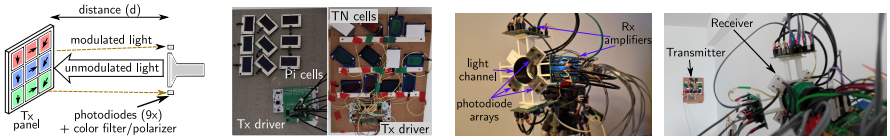


(a) Link's configuration (b) Transmitters (c) Receiver (d) Communication link

Figure 5.9: Platforms: configuration, transmitters, and receivers.

### 5.3.4. DEMODULATION

The demodulation follows simple steps.

*step 1:* We apply a 3rd degree low-pass Butterworth filter with a bandwidth higher than the clock frequency of the payload. This filter removes most of high frequency noise.

*step 2:* The preamble is located by detecting the first strong peak in the signal, and then, the entire preamble (between the red bars in Figure 5.8d) is used to obtain the channel matrix.

*step 3:* The clock signal is extracted from the 'payload' of the first channel, and used to determine the location of data bits in all other channels.

*step 4:* Decoding the payload requires a threshold. Anything above the threshold is considered a '1', and otherwise a '0'. The threshold depends on the LC cell's bandwidth and modulation period. For the LC in Figure 5.8d, a full switching cycle takes more than 3 ms, but to increase the data rate we use a period of 1 ms. For that period, we found empirically that a threshold of 0.2 (normalized with respect to the maximum signal strength in the preamble) is reliable to decode data.

Overall, we observe that a solid theoretical foundation enables the design of simple (de)modulation processes, compared to the SoA, which relies on heuristics to develop complex modulation schemes.

## 5.4. PLATFORMS

We tested our theoretical framework by developing a backscattering communication link. The link's configuration is shown in Figure 5.9a. Our setup assumes the standard backscattering scenarios in the SoA, where *objects* with lights –such as ceiling luminaires, desk lamps or car lights– gather data from nearby *surfaces*. In our prototype, the light radiated by the object is not modulated itself,however, upon reaching a surface with LCs and retroreflectors, this light is modulated and backscattered to the object, which has photodiodes to decode the passive link. The details of our prototype are explained below.

### 5.4.1. TRANSMITTER (SURFACES)

In our MIMO transmitter, we do experiments with two types of liquid crystals: a) Twisted Nematic (TN) cells, and b) Pi cells. TN cells are cheaper, easier to drive, and more power efficient, however, most commercial TN cells have limited bandwidth. We used TN cells with a bandwidth of about 125 Hz (2 ms charging time and 8 ms discharging time), and Pi cells with a bandwidth of about 400 Hz (0.7 ms charging time and 2.5 ms discharging time). To drive these cells, we use off-the-shelf STM32 microcontrollers combined with

| | Component | Pi cell Tx | TN cell Tx |
|---|---|---|---|
| Transmitter | LC cell | 9 × 15 USD | 9 × 4 USD |
| | Nucleo board | 17 USD | 17 USD |
| | Power consumption | 450 mW | 0.37 mW |
| Receiver | Photodiodes | 9 × 0.5 USD | |
| | Receiver boards | 9 × 7 USD | |
| | Power consumption | 150 mW | |

Table 5.2: Costs and power consumption

amplifying circuits.

For both TN and Pi cells, we build a panel of 3 × 3 LCs, with 3 different polarizations and 3 different colors. All cells are mounted on retroreflectors, as done in the SoA [32, 42, 34], to send the modulated light back to the object. Using retroreflectors does not degrade the communication link, as these devices preserve both polarization and color of the light. The transmitters with TN and Pi cells are shown in Figure 5.9b.



### 5.4.2. RECEIVER (OBJECT)

Our receiver consists of 9 photodiodes (PDs) mounted on a 3D stand. The light source is a 13 W flashlight, which is similar to the 12 W lamp used in Retro-VLC [42]. The color filters and polarizers of the transmitting LCs are also placed in front of each PD. In our evaluations, we use the same number of PDs as the number of transmitting channels. The receiver as well as the flashlight on which it is mounted are shown in Figure 5.9c.

### 5.4.3. COST AND ENERGY CONSUMPTION

The cost and power consumption of the platforms are shown in Table 5.2. Contrary to the TN cells, the Pi cells add the most cost as a trade-off with their higher speed: a combination of their transmitters and receiver array costs around 250 USD.

We tried selecting LCs with responses similar to the ones reported in the SoA. The response of the TN cell is close to the ones used in [32], and the Pi cell's response is close to the ones used in [34, 75]. We, however, did not optimize the hardware to obtain a sub-milliWatt power consumption. Between the two types of cells, we found that the Pi cells are faster but they consume more energy because they require higher frequency pulses (2 kHz) oscillating at amplitudes of ±10V for the opaque state, and ±5V for the transparent state. On the other hand, the TN cells only require 0V and 4V to oscillate between the two states at frequencies below 400 Hz. *We can state that making platforms with the fast but low-power cells reported in [34], as well as optimizing the driving circuits, would be the best combination of our work and the SoA.*

## 5.5. EVALUATION

In this section, we assess the system's performance in several aspects such as BER, distance, and condition number.

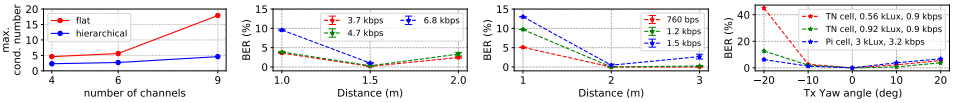


(a) Comparison of flat and hierarchical approaches.

(b) BER using Pi cells.

(c) BER using TN cells.

(d) BER at different yaw angles

Figure 5.10: Evaluation results.

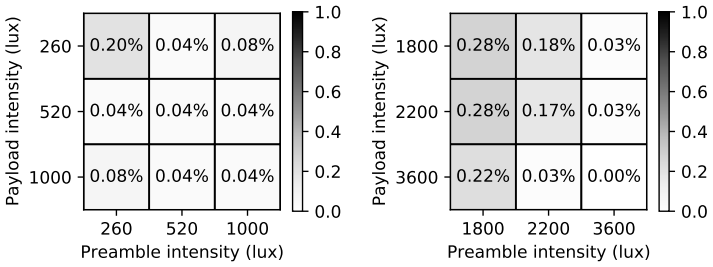


(a) TN cell, 0.9 kbps

(b) PI cell, 3.2 kbps

Figure 5.11: BER when the preamble and the payload are captured under different light intensities.

### 5.5.1. FLAT VERSUS HIERARCHICAL MODULATION

In Section 5.3, we stated that there are three advantages when it comes to hierarchical modulation: a lighter preamble, lower computational complexity, and better performance. We already showed the first two advantages analytically, and we left the third to an empirical evaluation. To do this comparison, we run experiments with our basic setup described below:

***Experimental setup:*** To implement the multiplexed link, we have our setup in a low light office environment of about 100 Lux. We maximize the receiver's gain such that it stays below saturation considering the ambient light and transmitted signal. The link is shown in Figure 5.9d. In this Figure, the transmitter is 3 meters away from the receiver, however, we change this distance in different experiments.

To compare the two modulation approaches, we do experiments in which 4, 6, and 9 channels are multiplexed at a distance of 2 m. For the *flat* approach, we report the condition number of the channel matrix, and for the *hierarchical* approach, first, we calculate the condition numbers for color and polarization separately, and report the bigger of the two, as this determines the overall quality of the channel separation. The results are shown in Figure 5.10a. As is evident, the *hierarchical* approach outperforms the *flat* one, specifically for 9 channels, in which the *flat* approach is almost non-recoverable. Also, in all experiments, the *hierarchical* condition number stays below 5, guaranteeing a *good* demultiplexing of the channels.

### 5.5.2. BIT ERROR RATE

Using the *experimental setup* described before, we evaluate the two transmitter types: Pi cells and TN cells. For each type of cell, we run experiments with constant and varying light. Below, we describe each scenario separately.

#### PI CELLS

To evaluate these cells, we conduct experiments at 1, 1.5 and 2 meters, operating all of the 9 parallel channels. For the three distances above, the light intensity at the transmitter is 3.5, 1.3, and 0.9 kLux, respectively. Following Section 5.3.3, we set the preamble's bit duration to 10 ms, and for the payload's period, we use three settings of 1, 1.5, and 2 ms per channel. Also, as stated in Section 5.3, we assign one channel to clock transmission, thus, the effective data rates –considering the longer preamble and that one LC is used as clock– are 6.8, 4.7, and 3.7 kbps. In our tests, we send packets of 500 or 1000 randomly generated bits, and calculate the BER. These results are shown in Figure 5.10b. At 1.5 meter, the BER for 3.7 and 4.7 kbps is almost 0, and for 6.8 kbps stays below 1%. However, as the distance increases, the BER of the low and mid rates increases to about 3 to 4%, and the link with the highest rate is not recoverable.

At 1 meter, the results might seem counter-intuitive: we expect to see lower BERs after decreasing the distance. However, at this distance, some of the transmitters go out of the field-of-view of the receivers. Thus, the high BER is due to the demultiplexing, and not the demodulation. This issue could be solved by using a more compact transmitter putting all of the LCs in the FoV of the photodiodes.

#### TN CELLS

These cells are inherently slower than Pi cells: their maximum bandwidth for a full contrast is 125 Hz. Here, we experiment at three distances: 1, 2, and 3 meters, using a preamble clock of 15 ms and three payload clocks: 5, 6, and 10 ms. Similar to the Pi cells, we dedicate one channel as clock, hence, the effective data rates are 1.5, 1.2, and 0.7 kbps. In these tests, the payloads consist of 300 random bits. The BER results are shown in Figure 5.10c. At 2 meters, the BER stays at 0.0% for 0.76 and 1.2 kbps, and at 3 meters, it is still 0 for the slower setting, and stays under 1% for the mid data rate. For the faster setting, the BER is close to 1% at 2 m. Similar to the Pi cells, at 1 meter, there is an increase in the BER. However, this increase is more substantial compared to Pi cells. This is because the TN cells are bigger and more distant to each other. Thus, the transmitters go out of the FoV of the receivers faster, resulting in a poorer demultiplexing at the same distance. As stated before, a more compact design of the transmitter would solve this limitation.

We see that the TN cells reach a lower BER despite being modulated at 1.6× their bandwidth and longer distances. We attribute this to the following reasons:
*reason 1:* The TN cells have a larger surface area to reflect back more light. Hence, they will show a higher SNR.
*reason 2:* When both TN and Pi cells are in the 'on' state, the TN cells let more light through, making for a bigger contrast between their dark and light state.

#### EFFECT OF YAW ROTATIONS

As stated earlier, our system is resilient to roll rotations, but evaluating yaw rotations is important too. In all previous experiments, the LCs are facing the receiver, i.e. an approximate yaw angle of 0°. To test how the link performs with yaw offsets, we rotate the panel by -20, -10, 10, and 20 degrees. The BER of both TN and Pi cells are shown in Figure 5.10d. We can observe that the measurements are different for negative and positive offsets. This is because of the non-symmetrical arrangement of the cells. As the Pi cell transmitter is more compact and regular, it results in a more uniform increase in BER in both directions. Overall, we observe that the platform has some resilience to yaw offsets up to $-10°$, maintaining a BER below 1% for both types of cells at higher light intensities. However, this performance can be improved further with more compact and symmetric designs.

#### VARYING LIGHT INTENSITY

In Section 5.3.3, we stated that a re-transmission of the preamble is not necessary if the light intensity changes. That is, the preamble gathered at light intensity X can be used to decode payloads obtained at light intensity Y. We test this property with both cells at 2 m. In each experiment, we transmit packets at three different light intensities: 260, 520, and 1000 Lux for TN cells, and 1.8, 2.2, and 3.6 kLux for Pi cells. Then the payloads are separated from the preambles, and the channel matrices obtained from each light intensity are used to decode all the payloads. The results are shown in Figure 5.11. For both types of cells, the BER remains below 0.3%. This implies that the preambles do not need to be re-transmitted when the intensity changes, which means that in the long term, Pi and TN cells could reach 8 kbps and 1.6 kbps, respectively.

The BER matrices also show that preambles with higher SNRs (1 kLux for TN cells and 3.6 kLux for Pi cells) lead to slightly better results, as the channel parameters are obtained in a more robust manner. As stated before, the resilience to changes in light intensity is obtained because: (i) at the preamble, channel matrices scale inherently to changes in intensity, and (ii) at the payload, our decoding process normalizes the signal with respect to its own *local* maxima.

## 5.6. CONCLUSION

To increase the data rate and concurrency in passive-VLC, we looked into the powerful, but not well explored method of MIMO. We revisited its theoretical framework and adapted it to passive-VLC properties considering the most popular optical modulator: liquid crystal (LC) cells. We also designed a hierarchical multiplexing method resulting in better channel separation. Our methods and prototypes show that the system's data rate increases almost linearly with the number of LCs. Also, as there are no assumptions on the individual sub-channels, we hypothesize that other SoA systems could implement our framework to increase their data rate.

# 6

# PASSIVECAM

In previous chapters, we considered improvements to the bare physical layer of passive VLC. However, these enhancements are not by themselves appealing to a majority of users. To introduce this new field, it is always helpful to develop real-world applications. Therefore, in this chapter, we build a potential scenario where passive VLC is combined with an emerging field called screen-to-camera communications.

In screen-to-camera communications, data is embedded into videos in a way to be invisible to viewers, but not to cameras. This opens up opportunities to increase communication capacity, as well as embedding advertisement and other useful information unobtrusively into videos. In addition, this technology relies on visible light and not the overly-congested and expensive radio spectrum, making it suitable for pervasive deployment. Motivated by these advantages, there are several studies in screen-to-camera communications [53, 50, 47, 48, 49], whose focus is on increasing the PSR without affecting the viewer's experience.

The research community has achieved large feats in screen-to-camera communication, but the main downside is the power cost. As an example, a regular LCD monitor uses at least 26 Watts[1]. The culprit is its backlight, which consumes more than 80 % of the total power. Following the design paradigm of passive VLC, a new generation of transparent screens are removing that power cost by using ambient light instead of LEDs. The image quality is not as sharp as in traditional screens, however, they consume much less energy, which is a major advancement in designing novel screens with a low ecological footprint.

Transparent screens are already being deployed in buses, airports and offices despite being a novel technology. They are transforming the facades of different environments to transmit relevant information on demand. For example, smart windows facing the runway of airports display advertisements to the passengers, as shown in Figure 6.1. However, displaying plain pictures and videos on these monitors is not exploiting their potential. In other words, what if the transparent screen transmitted more information?

[1] Based on measurements on a LG LM215WF4-TLE7

Figure 6.1: An application of passive displays: a video is shown in an airport using ambient light. The display remains transparent and does not block the outside's view. Image from [46].

For instance, while showing an enticing holiday destination, some users may want more information on discounted hotels or restaurants in that specific location. To achieve that, a user could point her smartphone's camera towards the video and obtain that *embedded and invisible* information.

Inspired by advances in screen-to-camera communication, in this chapter, we present PassiveCam, a system that enables the first wireless link between transparent screens and smartphones. While being advantageous in terms of power consumption, designing this new link introduces two main challenges. First, compared to the original backlight of a display, ambient light is weaker and variable, resulting in lower image quality, which in turn makes the communication link more error-prone. Second, most SoA works do not consider proper human-computer-interaction designs. Some studies do not evaluate the effect of a user's camera movements, evaluating their work only with their camera on a tripod; other studies do not process the videos in real time; and a few systems rely on visual markers, either static or dynamic, to delineate the borders of their transmitting area, affecting the system's aesthetics.

To overcome the limitations mentioned above, we propose a novel communication system with a passive screen acting as transmitter and a smartphone (App) acting as a receiver. In general, PassiveCam provides the following contributions:

***1) A passive screen transmitter.*** Passive screens are not off-the-shelf components yet, but we test two transparent screens: one obtained from a specialized vendor [46] and the other created by us. We describe how to remove the back-light of normal displays, in order for the interested researchers to create their own passive screen. Our modified screen reduces the power consumption by 80 %. Regarding the modulation process, we build on top of the SoA, however, we improve their encoding with three steps: Gaussian kernels, step encoding, and an optimization of texture analysis.

***2) A reliable real-time receiver.*** Our receiver, running on a custom Android App, tackles two important points to facilitate a seamless user experience. First, unlike many prior studies where a static phone on a tripod is used, we implement a simple hand motion filter so that users can hold the phone. Second, to attain a real time response, we propose a new method to detect the Region of Interest (ROI) and discard invalid frames.

***3) A new application:*** As far as we know, the use of passive screens for communication (commercial or modified) has not been explored before. We evaluate the link's relia-

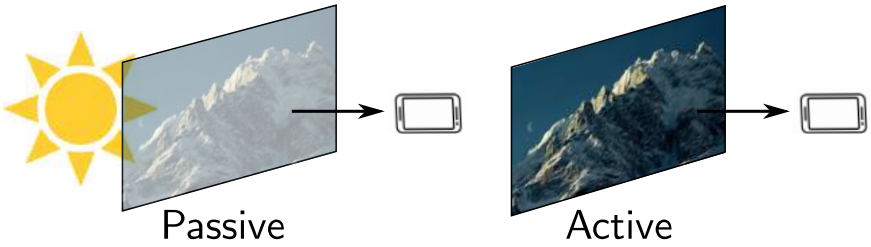


Figure 6.2: In passive displays, the backlight is provided by sunlight. In standard (active) displays, the backlight is provided by LEDs. If data is embedded in the frames, a smartphone can decode information with screen-to-camera communication.

bility and delay with controlled experiments, but we also propose a novel application. Together with personnel of a company, we target the following scenario. Considering the massive windows (passive screens) at airports, multiple types of videos could be displayed (music, tourism, news, etc) and users may want to listen to one of those streams. To do so, they could point their phone toward the desired video, and our passive link would decode the video ID and the exact time of the frame to provide its synchronized audio. A prototype of such application is shown in two anonymous videos: one in black-and-white [76] and the other in color [77]. Overall, PassiveCam has an offline code success rate of close to 90%. Besides, our real-time Android application acquires synchronization within 530 ms when mounted on a tripod and 1071 ms when hand-held.



## 6.1. A PASSIVE TRANSMITTER

In order for a display to qualify as "passive", it requires using ambient light, in contrast to *normal* LCDs emitting light by themselves. Figure 6.2 shows the difference between active and passive screens. Transparent screens are not widely sold in the consumer market except by few select companies. Therefore, we will first describe how a passive screen can be obtained from a normal screen, and then, we will explain the modulation process.

### 6.1.1. PASSIVE DISPLAYS

To understand how a passive screen can be made, first, we need to explain the structure of a typical display. LCDs are made of several components as shown in Figure 6.3. ① is an array of LEDs or a fluorescent lamp emitting the monitor's backlight. Layer ② is an acrylic sheet, dispersing the light uniformly across the monitor. The dispersive layer scatters light to both the back and front, but the light that goes into the back side of the monitor is wasted. Therefore, a reflective layer (③) is used to recover this light and send it towards the viewer. At the end, layer ④ is a transparent glass layer containing pixels and displays the image to the user.

Based on our measurements, the screen's backlight consumes more than 80% of the total LCD's power. Thus, to make a passive screen, we need to remove all components except layer ④. It is important to note that the interface that controls the display is only connected to layer ④, which contains the pixels. Thus, it can still show pictures and

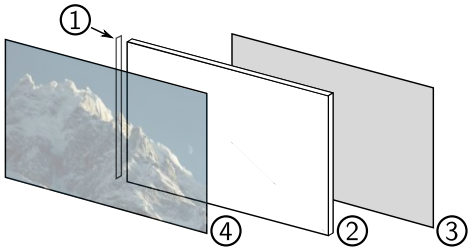


Figure 6.3: Layers and components inside an off-the-shelf monitor: ① an LED or lamp, ② a light dispersion layer, ③ metallic reflective layer, ④ a transparent LCD glass containing pixels

videos. The process required to disassemble a screen is not complex and can be done with any LCD, however, it has to be done carefully to avoid damaging the glass layer. An example of our passive screen, placed over a window, is shown in the videos of [76] and [77].

Another type of passive display we use is a "smart window" [46]. Smart windows have similar operating principles to the layer ④ of a monitor. Nevertheless, they are optimized to cause *less attenuation* to the light, resulting in more transparency and a *higher contrast*. This lower attenuation of light comes at a cost: smart windows only provide black-and-white images. To show colored pictures, normal monitors have color filters on their pixels, which dissipate light excessively. As a result, a smart window is made without these color filters. On the contrary, a modified LCD *looks* darker than a smart window, providing in a lower SNR when used as a transmitter.

Overall, a smart window is optimized to operate as a black-and-white transparent screen, however, they are not easily accessible yet. Therefore, we evaluate both types of displays. Besides, we develop our final application on a modified display to show that a passive link can also be made without a high-end smart window.

### 6.1.2. DATA EMBEDDING

Embedding data into videos has been considered by several works [47, 48, 53, 50], all of which use active screens. In this section, we first present the basic principles of data embedding, and then, we describe how we build upon these SoA.

#### BASIC PRINCIPLES

Data embedding exploits the slow response of human eyes. If a sequence of colored pixels are shown fast enough, the human eyes would perceive the average color. Based on this principle, we present a general encoding algorithm that reduces visual effects to human eyes.

An algorithm that embeds data takes two main inputs: a video with frames indexed by $f_0, ...f_n$, and the *data* that has to be encoded in those frames. In visual communications, data is represented by *binary frames*. A binary frame is similar to a QR code showing a checkerboard pattern. To take advantage of the *basic principle* above, the data encoding algorithm works as follows. First, every frame in the original video is duplicated. Then, a modulation value of $\Delta$ is calculated for each pixel. The pixel at location (x,y)–denoted by $f_i(x, y)$–in the first frame is then increased by its respective $\Delta(x, y)$, i.e.

$f_i^+(x,y) = f_i(x,y) + \Delta(x,y)$. In the other frame, the modulation values are subtracted, i.e. $f_i^-(x,y) = f_i(x,y) - \Delta(x,y)$. The resulting $f_i^+$ and $f_i^-$ are called complementary frames, and if played fast enough, the viewer's eyes shall average them to see the frame $f_i$, although modulated frames are being displayed.

Regarding the creation of binary frames, the SoA proposes custom procedures, however, we opt for QR codes for two reasons: (1) They are mature and well-developed, thus can be easily integrated into an application, and (2) The implementations are already optimized and tested, hence reducing the overhead of designing a receiver pipeline.

### LIGHTNESS MODULATION

The binary frame indicates the location of the pixels that need to be modulated, but it does not state how to derive $\Delta(x,y)$. For this, the SoA proposes various modulation schemes [47, 48, 53, 50]. We build upon schemes that modulate *lightness* instead of *color*, as our smart window only operates in black-and-white.

Several approaches use color spaces to guide the modulation process. The CIELAB standard divides the color space into two main dimensions: lightness ($L^*$) and color ($a^*, b^*$). In our case, to modulate a given pixel, the lightness is changed by $\Delta L^*$. Following the complementary modulation above, if a pixel falls in a white region of the QR code, we set the its $\Delta(x,y)$ to $+\Delta L^*$. Otherwise, it is set to $-\Delta L^*$. Therefore, for each frame, we two complementary modulated frames are generated. Next, we first describe the building blocks we borrow from the SoA, ChromaCode [50], and after that, we describe our improvements.

**Building blocks from the SoA.** ChromaCode's key contribution is to show that the parameter $\Delta L^*$ depends on the *human perception of color* and the *texture* around a pixel. The human perception is self explanatory. Regarding the texture, for instance, changes in lightness are less perceptive in *rough* images (like rocks) than in *soft images* (like clear skies). Thus, the same modulation depth $\Delta L^*$ would affect the flicker effect of each pixel differently.

*Step 1: Perception-based derivation of* $\Delta L$. To determine a proper change of lightness $\Delta L_1^*$ for a pixel location (x,y), ChromaCode employs the CIEDE2000 formula to take human perception into account. The complete formula is explained in [50]. Below, we present a re-arranged equation that suits our purpose. Denoting $L_1^*(x,y)$ as the lightness of pixel $(x,y)$, $k_L$ as a parameter to compensate for different viewing conditions, and $\Delta E_{00}$ as the perceived difference in color between two *complementary* pixels; the modulation depth $\Delta L_1^*(x,y)$ is given by:

$$\Delta L_1^*(x,y) = k_L[1 + \frac{0.015(L^*(x,y) - 50)^2}{\sqrt{20 + (L^*(x,y) - 50)^2}}]\Delta E_{00} \tag{6.1}$$

where $L_1^*(x,y)$ is given for every pixel and $k_L$ is set to 1. The important part is to determine $\Delta E_{00}$. A large value increases the signal's SNR but also the flicker effect. A $\Delta E_{00}$ between 1 and 2 results in acceptable flicker levels.

*Step 2: Texture-based adaptation of* $\Delta L$. In the prior step, $\Delta L^*$ considers only the perceived difference in color $\Delta E_{00}$, but not texture. This step estimates the texture of a pixel area by measuring how abruptly the pixels change. The bigger the changes, the rougher the texture, and the less obvious the flicker effects.

A common approach to calculating texture is Regional Texture Analysis, which constructs a Gray Level Co-occurrence Matrix (GLCM) for every pixel. Based on this matrix, one can calculate the contrast $C(x,y)$ in a pixel area. The construction of the GLCM matrix and contrast is detailed in the appendix. Using this method, ChromaCode [50] further proposes an *average* texture metric $T(x,y)$ around pixel *p(x,y)*:

$$T(x,y) = \frac{C(x,y)}{S(x,y)} \tag{6.2}$$

where $C(x,y)$ is the contrast and $S(x,y)$ is the number of pixels in a $n \times n$ area around pixel $(x,y)$. Based on $T(x,y)$, the following scaling parameter $\alpha(x,y)$ is derived to adjust the modulation depth based on texture:

$$\alpha(x,y) = \frac{T(x,y)}{T_{max}}(1-k) + k, \tag{6.3}$$

where $T_{max}$ is the maximum value of $T(x,y)$ in the frame, and $k$ is a parameter with a default value of 0.5.

In the end, the modulation depth of a pixel $\Delta L_2^*(x,y)$ is determined by the *color perception* $\Delta L_1^*$ and *texture* $\alpha(x,y)$.

$$\Delta L_2^*(x,y) = \Delta L_1^*(x,y) \cdot \alpha(x,y). \tag{6.4}$$



This value modifies the lightness of each pixel in the video.

**Improvements over the SoA.** The SoA provides a valuable starting point to embed information, but there are a few shortcomings that need to be improved for PassiveCam.

The SoA relies on better transmitters, with constant strong light; and better receivers, with cameras having 120 or 240 FPS. Our passive transmitter has weak variable light, and the phone we use has 60 FPS (to develop a more inclusive system). These two differences cause more flicker effects due to variable lighting conditions and a slower modulation. To ameliorate these flicker effects, we propose two improvements.

*Improvement 1: Gaussian kernels.* Given that the *sharp* borders in the binary frames cause noticeable artefacts, we apply a Gaussian kernel over the binary frame to smooth the sharp transitions. This process blurs the borders, making the embedding less noticeable, as surveyed in Section 6.3.5.

*Improvement 2: Step encoding.* In screen-to-camera communication, the frame rate of the receiver (camera) must be the same or higher than the transmitter's (screen). There are still many smartphones limited to capturing at 30 FPS in real-time. In this case, the screen must also transmit at a maximum of 30 FPS. This limitation causes the capacity of most screens with 60 or 120 FPS to be underutilized. Therefore, we propose a method to use this extra frame rate for the sake of flicker reduction. In the SoA, a modulated pixel changes from $+\Delta L^*$ to $-\Delta L^*$, making for an abrupt change of $2\Delta L^*$. However, if the screen can work at a higher rates than the camera, the encoding can be done in smaller, giving the impression of a smoother transition. For instance, let us consider a display with 120 FPS. If we aim for the transmission of binary frames at 30 FPS, a trivial configuration is to have two frames with $+\Delta L^*$ and two frames with $-\Delta L^*$. On the contrary, we can have one frame with no modulation, one frame with $+\Delta L^*$, another frame without modulation, and the last frame with $-\Delta L^*$. In this way, the lightness transition between

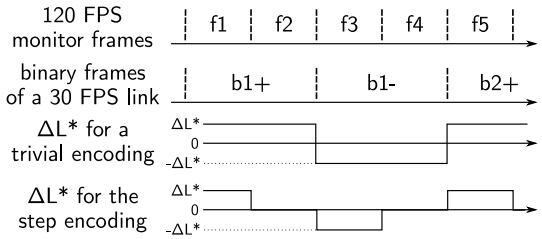


Figure 6.4: Timeline of step encoding versus standard encoding.

frames is reduced by half, from $2\Delta L^*$ to $\Delta L^*$, ameliorating flicker effects. The trivial modulation and and the step encoding are both shown in Figure 6.4 for this example.

*Improvement 3: Optimized texture analysis.* Our third improvement is related to optimizing the computational performance. Embedding information on videos requires several signal-processing steps. The most demanding step is the texture analysis done with the GLCM matrices. This high overhead would not be a problem if data was embedded only once. However, for applications that require periodic encoding, potentially in real-time, it is worth using the optimized method presented in appendix 6.5.1, which can reduce the encoding time by a factor of 500.

## 6.2. DECODING

To decode a video, a smartphone's camera is used. We consider two scenarios: *offline* and *real-time* decoding. The *offline* process first records the video and then recovers data. In contrast, the *real-time* process starts recovering data as soon as the frames are captured. The *real-time* process targets realistic scenarios of a user receiving data from the screen, and the *offline* process aims at evaluating the encoder's performance, regardless of the processing power of a user's phone.

### 6.2.1. OFFLINE DECODING

For the offline decoding, we mount a smartphone on a tripod, and its camera records the encoded video, as described in Section 6.1.2. Next, the files are transferred to a PC for data extraction using the following processing steps:

Step 1) Adjusting the camera's frame rate: As stated by the Nyquist law, the sampling rate should be at least twice the highest frequency in the transmitted signal. With complementary modulation, the highest frequency is half the modulation's frame rate. Thus, if the camera captures data with at least the same frame rate as the video, Nyquist is satisfied. Capturing at a higher rate can be advantageous as there is less chance of frame loss due to camera jitter. However, rolling shutter effects might become present.

Step 2) Adjusting the camera's ISO and shutter speed: ISO is the sensitivity of the camera's sensor to light, and the shutter speed is the duration of the sensor's exposure to light. In CMOS image sensors, there is a chance of capturing a rolling shutter effect, depending on the shutter speed. Usually, increasing the shutter speed (reducing the exposure) removes this effect. However, it darkens the pictures, resulting in the loss of encoded data. Hence, by increasing the ISO, brightness can be adjusted again. Based on the ambient

light, these values can differ. In Section 6.3, we do experiments using different levels of ISO and shutter speed to find the best setup.

Step 3) Data extraction: In Section 6.1.2, we mentioned that the encoding algorithm makes complementary frames: if in frame $i$ (denoted by $f_i^+$), the pixel (x,y) has a lightness of $L_i(x,y)^* \pm \Delta L_i(x,y)^*$, the lightness of the (x,y) pixel in its complementary frame (denoted by $f_i^-$) will be $L_i(x,y)^* \mp \Delta L_i(x,y)^*$. Therefore, subtracting $f_i^+$ and $f_i^-$ yields a new frame with pixel values of $\pm 2 \times \Delta L_i(x,y)^*$. This last frame contains the encoded QR information. Considering this differential process, we implement the decoder.

Following Step 1, we assume that the camera's frame rate is equal to the transmitter's, thus, each frame is captured once and no frames are missed[2]. As a result of the matching rate between the screen and camera[3], the receiver has all the frames and their complements in order, i.e. $\{..., f_{i-1}^+, f_{i-1}^-, f_i^+, f_i^-, ...\}$. Then, we subtract all captured frames from the one before. Our goal is to keep the result when a frame is subtracted from its complement. However, an important point is that the receiver cannot know in advance which frames are complementary. Therefore, in every other subtraction, it operates on frame $i$ ($f_i^+$) and the complement of the previous (non-matching) frame ($f_{i-1}^-$), yielding a corrupt QR code since two different binary frames are subtracted. As we will show in Step 5, these corrupt frames can be detected and do not pose any problems besides consuming the decoder's time.



To generalize our assumption about the frame rates, if the camera captures at a higher rate, there will be more instances of the same frame. In that case, subtracting consecutive frames sometimes results in a dark image, i.e. when the captured instances of the same frame are subtracted.

Step 4) ROI detection: Since the binary codes may not cover the entire frame, a captured video will likely contain both encoded pixels and other surroundings, including non-modulated regions of the video. Before passing the pixels to a QR decoder, the region containing valid data has to be identified. Previous works use visual markers around a screen so that the ROI can be easily detected, but we use a simpler technique. Going back to Step 3, we notice that in subtracted frames, all regions that are not encoded (shifted by $\Delta L^*$) have a lightness of 0, as their pixel values are the same as in their complementary frames. Using this fact to determine our ROI, we just need to find the smallest region inclusive of all pixels with a non-zero lightness, which is a simple task in image processing.

Step 5) QR decoding: This is the last step to extract binary data from pictures. For offline decoding, we use a QR decoder library in Python, and process the ROIs found in Step 4. However, as mentioned in Step 3, every other subtracted frame contains corrupt data. This does not pose any problems in offline decoding, since QR codes have checksums and corrupt frames can be detected and dropped. However, attempting to decode those frames delays the processing, which becomes problematic in a real-time system, which will be discussed below.

[2] This assumption helps simplify the explanation. In practice, some frames will be missed, but they can be recovered using error correction codes

[3] Later, we generalize the decoding procedure for higher camera frame rates

### 6.2.2. REAL-TIME DECODING

After validating the encoding with the offline process, we implement the receiver pipeline on a smartphone to build a real-time link. When a person uses the phone in real-time, the receiver faces extra challenges mentioned below.

#### HAND MOVEMENT FILTERING

A user, unlike a tripod, cannot hold a phone completely steady. Therefore, we have to remove the effect of camera movements before decoding. To address this dynamic, we implement a simple hand motion filter that uses prominent points in consecutive frames as *anchors*, and calculates a matrix to map these prominent features between frames. By applying the inverse transform to the shifted image, its pixels can align well with their counterpart in the other frame, hence alleviating the hand movement effect.

#### LATENCY OPTIMIZATION

As mentioned before, subtracting two non-complementary frames yields undecodable QR codes. Following the method in Step 3, undecodable codes would appear in every other subtracted frame. If the corrupt data is speculated preemptively, it can be discarded right away, without waiting for the QR decoder to do so. Such receiver is called to be *synchronized*.

To acquire synchronization, we build upon the observation that the correct frames are alternating, therefore, at the beginning, the pipeline makes an attempt to decode all frames, corrupt and healthy, but soon after the first successful decoding, the pipeline sends every other frame to the decoder, and discards the rest. Some factors, such as camera jitter, might result in losing this synchronization over time. Therefore, we should perform periodic checks, and if the decoding error is above a threshold, a synchronization has to be performed again.



## 6.3. EVALUATION

### 6.3.1. CORE SETUP

In our experiments, we use three screens: The first screen is an active (normal) LCD that we use as a baseline to compare with passive displays (Figure 6.5a), the second one is a modified passive display obtained from an LG LM215WF4-TLE7 monitor using the procedure of Section 6.1, and the third one is a smart window obtained from a manufacturer [46]. The passive screen and the smart window do not emit any light, therefore, we install them in front of our office's window, as shown in Figure 6.5b. On the receiver side, a smartphone camera is placed at various distances up to 1.5 m from the screen. Using this setup, we carry out the experiments described below.

### 6.3.2. PERFORMANCE IN CLOUDY WINTER DAYS

The fundamental difference between active and passive screens is the backlight source. During the day, sunlight can range from one thousand Lux on a very cloudy day to 100 kLux on a clear day. With normal sunlight, our modified passive screen and the smart window work well. However, it is important to assess how different passive screens perform under unfavorable lighting conditions.

(a) Active monitor (b) Smart window

Figure 6.5: Setup of the experiments.

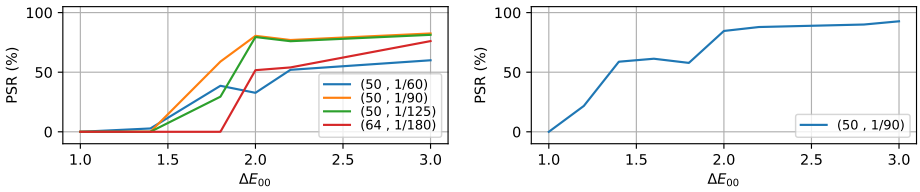


(a) Active monitor at 60 Hz (b) Passive Monitor at 30 Hz

Figure 6.6: Decoding performance on active and passive monitors.

6

To have a controlled scenario, we use offline decoding during a *cloudy winter day*. In these tests, we encode a single QR code in a video with different levels of visibility. We sweep the $\Delta E_{00}$ value in Equation 6.1 from 1.0 to 3.0 in steps of 0.2, yielding different $\Delta L^*$ to embed the QR codes. This video is displayed on the three monitors explained above, and the results are discussed next.

### ACTIVE DISPLAY

First, we use the *active* monitor as a benchmark with a frame rate of 60 FPS. A camera is installed on a tripod at a distance of 50 cm from the monitor capturing videos at 60 FPS. For each transmitted video, we set the camera to work with four different combinations of ISO and shutter speeds. Then, the decoding pipeline mentioned in Section 6.2.1 is used to calculate the PSR. Figure 6.6a shows the link's reliability (PSR) as a function of modulation depth ($\Delta E_{00}$). The four camera settings are denoted by the tuple (ISO, shutter speed), with the shutter speed being in seconds. Among the four combinations, (50,1/90) results in the best PSR, which is about 80% for $\Delta E_{00}$ values above 2.0. However, if $\Delta E_{00}$ is above 1.8, the encoding becomes gradually visible to people. The problem is that if we use this lower value of $\Delta E_{00}$, the PSR drops to about 50%. Hence, overall, with an active screen at 60 FPS, we get around 80% PSR but causing some flicker.

### SMART WINDOW

For this step, the videos are the same but the smart window is bigger than the active display. To capture the whole monitor, we place the camera at a distance of 1.5 m. The smart window has a maximum frame rate of 30 FPS, therefore, we also capture videos at

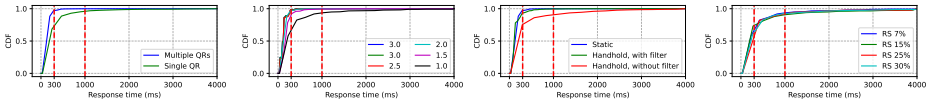


(a) Single QR vs. Multiple QR (b) $\Delta E_{00}$ variations (c) Static vs. handheld (d) Error correction levels

Figure 6.7: Response times for different implementation methods. The thresholds of Table 6.1 are marked with red dashed lines.

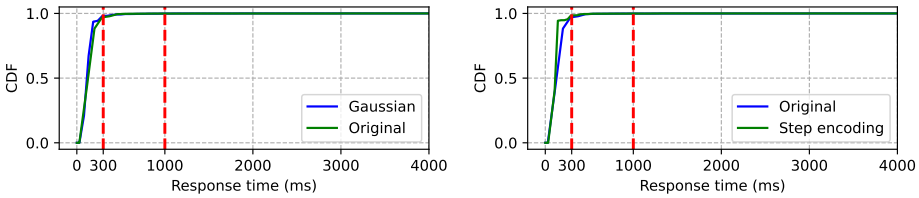


(a) Original vs. Gaussian kernel (b) Original vs. step encoding

Figure 6.8: Response times of different encoding methods.

30 FPS. The results are shown in Figure 6.6b. In these experiments, only one (ISO, shutter speed) setting worked reliably. The results are better than with the active monitor, around a 90% PSR with a $\Delta E_{00}$ above 2.0. This improvement is due to the lower frame rate since it ameliorates the rolling shutter effect. Overall, despite the low sunlight conditions, the active screen and smart window provide comparable performance. This is thanks to the smart window's emphasis on reducing attenuation but at the cost of working only in black-and-white.

#### MODIFIED SCREEN

The active display and the smart window could transmit data packets with various PSRs, as discussed earlier. However, our modified screen could not operate reliably because it attenuates more light than the smart window, as mentioned in Section 6.1. This low performance, however, is only for very low lighting conditions, the demo in the videos is done with our modified screen under normal sunlight conditions. The advantage of our modified screen is that it is obtainable from any monitor.

### 6.3.3. REAL-TIME DECODING

At the beginning of this chapter, we mentioned a sample application for passive screens that synchronizes the audio of a smartphone to a displayed video. In this section, we develop a real-time Android application using the decoding techniques described in Section 6.2 and benchmark its performance. Unlike the offline decoding used in the prior evaluation, a real-time system must have low response times to keep the user engaged. According to studies in this area [78], the maximum allowable response times and their interpretations are listed in Table 6.1. These thresholds are marked with vertical red dashed lines on all graphs in this section. To measure the response times, we calculate the Cumulative Distribution Function (CDF) of successfully decoding a packet within a given time. The response time has a positive correlation with reliability (PSR),

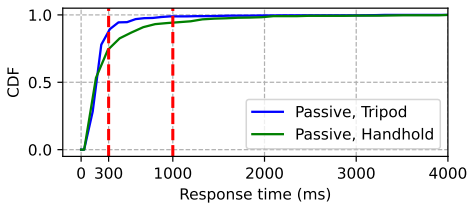


Figure 6.9: Response time of final system on passive display

| Response time | User's perception of the system |
|---|---|
| < 300 ms | Instantaneous |
| 300 ms to 1 s | Immediate |
| 1 to 5 s | Transient, not immediate, but the user does not disengage from the activity. |

Table 6.1: User's experience thresholds according to [78]

i.e. a link of better quality has a shorter decoding time. However, this depends on the phone's processing capabilities and the parameters used in data embedding. The phone we use is a medium-end device (Xiaomi Redmi Note 10 4G) and the Android application is optimized with multithreading to take advantage of the processing power.

In this section, we run the tests on our modified display to provide an upper bound of response times, since the smart window performs even better, as described earlier. The encoding parameters we control and their effect on the system's performance are mentioned below.

### THE IMPACT OF $\Delta E_{00}$

This value determines how perceptible the encoded data is. We sweep this parameter from a low value of 1 to a large value (most visible) of 3 in steps of 0.5. Then we measure the cumulative distribution of the response times. The results are shown in Figure 6.7b. Interestingly, the CDF curves for $\Delta E_{00} \in \{2, 2.5, 3\}$ are similar. There is a 95% chance of successfully decoding packets within 265 ms, 269 ms, and 267 ms, respectively. However, when $\Delta E_{00}$ is decreased to 1.5, the response time increases to 400 ms to have the same 95% success. Furthermore, for $\Delta E_{00} = 1$, the response time further escalated to 1305 ms. Although increasing the $\Delta E_{00}$ results in a shorter response time, it also makes the QR codes more visible. In Section 6.3.5, we perform a survey on visibility, where we show that with $\Delta E_{00} = 1.5$, the users *only* perceive a slight improvement compared to $\Delta E_{00} = 2.0$. Therefore, considering that the response time is substantially better in the latter case, we opt for a $\Delta E_{00}$ value of 2.0 in the rest of the experiments.

### REDUNDANCY OF EMBEDDED DATA

A single QR code occupies a small space and could leave large regions of a frame unused. By duplicating the QR code, the unused space can be utilized in favor of redundancy. To investigate this approach, the performance of a single QR code is compared with that of a video containing six QR codes copied all over the frame. As shown in Figure 6.7a, the CDF

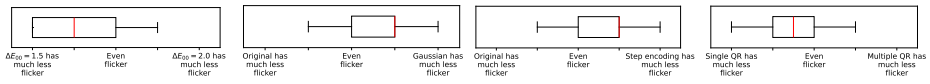


(a) $\Delta E_{00} = 1.5$ vs $\Delta E_{00} = 2.0$ (b) Effect of Gaussian kernel (c) Effect of step encoding (d) Single QR vs. 6 QRs

Figure 6.10: Survey results comparing flicker for different parameters and encoding techniques.

of a single QR code has a probability of 95% at a response time of 805 ms, while the link with 6 QR codes has the same reliability at 267 ms. This is a substantial improvement. As a result, we use the version with 6 QR codes in the rest of the experiments despite being more noticeable to a user. In our survey, we will show that the slight increase in visibility is a valuable trade-off to achieve a considerably lower response time.

### HAND MOTION FILTER

To verify the effect of hand motion on the response time, we do three experiments: (i) the phone is placed on a tripod and the filter is not active, (ii) the phone is held by hand and the filter is still not enabled, and (iii) the phone is held by a user and the hand motion filter is enabled. The results are shown in Figure 6.7c. In experiment (i), the CDF reaches a probability of 95% at 267 ms. In experiment (ii), the same success probability is achieved at 1737 ms, a substantially longer period. This can be attributed to unaligned frames, causing the phone to struggle to decode. Finally, in experiment (iii), a remarkable improvement is seen, with a CDF of 95% at 372 ms. This represents a significant enhancement compared to the configuration without the hand motion filter and is only slightly inferior to the static setup.

### QR ERROR CORRECTION LEVEL

When investigating the effect of $\Delta E_{00}$, we mentioned that a $\Delta E_{00} = 2$ satisfies the real-time requirements but it is not invisible. On the other hand, a $\Delta E_{00} = 1$ performs poorly in terms of response time while making the codes almost invisible. To investigate this trade-off further, we look into the inherent Reed-Solomon (RS) error correction of QR codes. We hypothesize that by increasing the error correction, the *unrecoverable* codes with a $\Delta E_{00}$ of 1 might become *detectable*, resulting in a lower response time.

In this regard, we set the $\Delta E_{00}$ to 1, and use four different RS levels on the QR codes. The CDFs of these experiments are shown in Figure 6.7d. We can see that none of the curves provide good performance according to the real-time classification of Table 6.1. For a CDF of 85%, the response times with different error correction levels are: 7% RS error correction yields a response time of 532 ms, 15% results in 545 ms, 25% gives 528 ms, and 30% results in 530 ms. Contrary to the hypothesis, all error correction levels demonstrate comparable performance. Considering these results, it is better to use a QR code with 7% RS error correction as it occupies less space and makes room to place more data.

### GAUSSIAN KERNEL

Applying a Gaussian kernel to the binary frames makes the encoded data less visible. To verify its effect on response time, we compare two cases with and without a kernel. The results are shown in Figure 6.8a. Without a Gaussian kernel, the CDF reaches 95%

at 266 ms. With the kernel, the response time does not vary and is 267 ms. Hence, the Gaussian kernel is harmless to the response time while it reduces the visual effects of the encoding.

#### STEP ENCODING

The CDF of the response times for transmitters with and without step encoding is shown in Figure 6.8b. When step encoding is enabled, a CDF of 95% is reached at 244 ms. When disabled, it gives a response time of 267 ms. Hence, this enhanced encoding does not affect the response time much and is safe to use.

### 6.3.4. FINAL IMPLEMENTATION

Our final implementation uses the results from the last sections. The video embeds 6 QR codes with an error correction of 7%, the $\Delta E_{00}$ is set to 2.0, and a Gaussian filter is applied. The real-time pipeline is tested with a passive screen and a camera in two conditions: hand-held and on a tripod. These results are shown in Figure 6.9. Based on the measured CDF, there is a 95% chance of decoding packets successfully within 530 ms using a tripod and 1071 ms when held by hand. According to [78], these response times are both classified within or very close to the *immediate* response category

### 6.3.5. SURVEY RESULTS

Although we propose methods to hide the encoding, visual distortions are inevitable since videos are modified. To evaluate modifications, we perform a survey where we place two videos side-by-side: one with and the other without the intended modification. Then, we asked a total of 20 users to compare the flicker of the two videos by choosing one out of five levels. The results are shown in the box plots of Figure 6.10. In these experiments, we consider the following four cases:

**a) Apply a $\Delta E_{00}$ of 1.5 or 2?** As mentioned in Section 6.3.3, there is a significant advantage in the response time when we move from a $\Delta E_{00}$ of 1.5 to 2. It is important to assess the user perception as well. As shown in Figure 6.10a, the median of users said there is "slightly less flicker" for the lower value of $\Delta E_{00}$. Considering this minor effect, and the big advantage in the response time of $\Delta E_{00} = 2$, we opt for this higher value.

**b) Apply Gaussian kernel or not?** Following Figure 6.10b, applying a Gaussian kernel helps reduce flicker.

**c) Apply step encoding or not?** Following Figure 6.10c, users see a better performance when step encoding is applied.

**d) Use single or multiple QR codes?** Using more QR codes occupies more space in a video, which can cause more flicker as validated by the survey in Figure 6.10d. However, this flicker is not significant. Considering its lower response time, the redundancy of QRs is worth implementing.

### 6.3.6. PASSIVECAM IN ACTION

Passive screens are being deployed more and more in public places. This opens opportunities for new applications. Together with members of a company, we propose the development of a real-time link for the following application: when a video is being publicly displayed, it is usually difficult for a user to hear quality audio. Therefore, we

use a phone to synchronize the video so users hear the video's sound on their phone. To make this system, we encode synchronization packets–i.e. frame numbers of the video–unobtrusively using the methods discussed before. Then, with our real-time application, the user's phone can read the hidden messages and play the audio accordingly. A demo of this application for a black-and-white and a color video has been put in the anonymous links of [76] and [77]. More details of this implementation are described in Appendix 6.5.2.

## 6.4. RELATED WORK

**Unobtrusive screen-to-camera communication.** Numerous studies have explored imperceptible data encoding in videos [47, 48, 50, 49, 51, 53, 52, 79]. The pioneering works in this area are InFrame [47] and its subsequent improvement InFrame++ [48]. They are the first to exploit the flicker fusion property of human eyes with complementary frames. However, TextureCode [49] identified that some flicker was present in those studies. The flicker appeared in smooth areas, hence, TextureCode proposed texture analysis to selectively pick the regions where data should be embedded. The latter improves invisibility but it sacrifices throughput, as it only uses areas with rough texture. To maintain invisibility while leveraging the entire frame, ChromaCode combines luminance with texture analysis [50]. Instead of using a uniform delta value to modulate the entire frame, ChromaCode adjusts the delta based on the expected human perception of color and texture. AirCode [53] employs the same video encoding as ChromaCode with the addition of an audio channel transmitting metadata, which compensates for the more error-prone screen channel. Given ChromaCode advancements and the fact that it uses lightness modulation instead of color, we used it as the basis of our work.



Other papers explore color domains to achieve invisibility. Deeplight [51] applies the delta value only to the blue channel as human eyes are less sensitive to blue light. Uber-In-Light uses both the blue and red channels to embed data [52], modifying the green channel just to compensate for the visual distortions. Other studies focus on chromaticity, considering that the maximum perceptible chromatic flicker occurs at approximately 25 Hz [79]. These color based studies are valuable, however, not applicable to black-and-white smart windows.

Overall, compared to all the above studies, our work the first to design a system for passive screens. Furthermore, our system works in real-time with low-end smartphones.

**Passive communication with light.** Another area that inspired our work is one using optical devices to modulate ambient light [44, 33, 80, 25, 42, 64]. These platforms can work with photodiodes and cameras but all of them focus on point-to-point links. To our knowledge, the only paper that moves towards passive screens is Sunbox [40]. This work employs a tiny microdisplay (mm in size) to transmit QR codes to a smartphone via ambient light reflections. However, there is no video transmission, only QR codes, and the phone has to be placed statically on a holder at a distance of three centimeters from the microdisplay.

## 6.5. CONCLUSION

In this paper, we explored a novel screen-to-camera communication link by using passive displays. Besides, by improving on top of the SoA, we encoded data unobtrusively in a video, which was then displayed by our passive and active screens. We showed that by using a smart phone, this encoded data could be extracted. As a proof-of-concept, we tested our custom Android application in a real-time audio synchronization scenario. Additionally, we assessed the performance of this system both in real-time and offline, based on several factors and user surveys. Overall, our work is the first to make a step towards new opportunities in *passive* screen-to-camera communication domain, paving the way for pervasive applications such as smart surfaces and in-video advertising.

### 6.5.1. OPTIMIZATION OF TEXTURE ANALYSIS

In prior literature, regional texture analysis is implemented by constructing a GLCM for every pixel. GLCM is a known method that quantifies the *texture* inside an $H \times W$ window around a pixel location (x,y) of the image. H and W are arbitrary numbers denoting the dimensions of the chosen window. The resulting GLCM has a dimension of $N_g \times N_g$, where $N_g$ is the number of distinct grey levels found in the image. Therefore, it is possible to obtain large GLCM matrices depending on the context of an image. Larger matrices have negative effects on calculations in two directions: (1) They consume time to calculate and access and (2) they take up space in the memory. To optimize for these issues, we simplify the calculations as mentioned below.

Let us denote an element of the GLCM matrix by $p_{(x,y)}(i,j)$, where (x,y) is the location of the pixel in the original image and the tuple (i,j) is the index of an element within the GLCM matrix of that pixel. Following the calculation procedure of GLCM [50], each $p_{(x,y)}(i,j)$ can be written as follows:

$$p_{(x,y)}(i,j) = \frac{1}{R_{(x,y)}} \sum_{r=0}^{H-1} \sum_{c=0}^{W-2} V(c,r) \tag{6.5}$$

$$\text{where } V = \begin{cases} 1, \text{ if } L^*(c,r) = i \text{ and } L^*(c+1,r) = j \\ 0, \text{ otherwise} \end{cases}$$

where $H$ and $W$ are the respective height and width of the arbitrary window around the pixel (x,y), and $R_{(x,y)}$ is the total number of horizontal neighboring in that window. In the summation, the index pair (c, r) sweeps over all pixels in the arbitrary window and sets the value of $V$ to 1 only if the pixel at (c, r) has the lightness of i and its right neighbor has the lightness j. In short, the element (i, j) of the GLCM matrix counts pixel pairs in the arbitrary window such that the left one has the lightness of i and its immediate right neighbor has the lightness of j.

After this, the contrast equation of the pixel at (x, y) reads as follows, assuming that $H = W = n$:

$$C(x,y) = \sum_{n=0}^{N_g-1} n^2 \{ \sum_{i=0}^{N_g} \sum_{j=0}^{N_g} p_{(x,y)}(i,j) \}, \quad \text{s.t.} |i-j| = n \tag{6.6}$$

Substituting Equation 6.5 in Equation 6.6 gives:

$$C(x,y) = \sum_{n=0}^{N_g-1} n^2 \{ \sum_{i=0}^{N_g} \sum_{j=0}^{N_g} \frac{1}{R_{(x,y)}} \sum_{r=0}^{H-1} \sum_{c=0}^{W-2} V(c,r) \} \tag{6.7}$$
$$\text{s.t. } |i-j| = n.$$

Moving the $\frac{1}{R_{(x,y)}}$ factor out of the summation and rearranging the terms will yield:

$$C(x,y) = \frac{1}{R_{(x,y)}} \sum_{n=0}^{N_g-1} n^2 \{ \sum_{r=0}^{H-1} \sum_{c=0}^{W-2} \sum_{i=0}^{N_g} \sum_{j=0}^{N_g} V \} \tag{6.8}$$
$$\text{s.t. } |i-j| = n.$$

Now the part $\sum_{i=0}^{N_g} \sum_{j=0}^{N_g} V$ will either be 1 if $L^*(c,r) = i$ and $L^*(c+1,r) = j$ or 0 otherwise. Therefore, Equation 6.8 can be simplified to:

$$C(x,y) = \frac{1}{R_{(x,y)}} \sum_{r=0}^{H-1} \sum_{r=0}^{W-2} \sum_{n=0}^{N_g-1} n^2 \tag{6.9}$$
$$\text{s.t. } |L^*(c,r) - L^*(c+1,r)| = n.$$

Substituting for the value of $n$ in Equation 6.9 will result:

$$C(x,y) = \frac{1}{R_{(x,y)}} \sum_{r=0}^{H-1} \sum_{r=0}^{W-2} (L^*(c,r) - L^*(c+1,r))^2 \tag{6.10}$$

Using Equation 6.10, we can bypass creating a GLCM for each pixel to reduce the computational time significantly. When benchmarked on a Graphics Processing Unit (GPU), the computational time of the optimized method was 40 ms for two complementary frames, whereas it was 20190 ms using the original method of formulating a GLCM for each pixel, yielding a speed-up of more than 500×.

### 6.5.2. IMPLEMENTATION DETAILS OF THE MUSIC APPLICATION

In this appendix, we describe the details of our application: a user points his smartphone camera towards the passive screen while a video is playing. The smartphone is then triggered to play the audio synchronized with the video.

In our example we use different songs including the video clip “Coldplay - The Scientist”. The embedded QR codes contain a song identifier and its frame’s index. This information is represented by a JSON string serving as a lightweight data interchange format. Each JSON string is structured as {‘s’:$s_{id}$,‘f’:$f_{num}$}, where the $s_{id}$ is an integer representing the song, and $f_{num}$ is the frame index of the video. Each song is saved on the smartphone prior to the experiment. With the $s_{id}$, the application can select the correct song, and with the frame number, it calculates the current time of the video.

To synchronize the audio with the video, the decoded frame number is converted to an absolute time value in milliseconds ($t_{abs}$) using the following equation:

$$t_{abs} = \frac{2 f_{num}}{FPS_{TX}} \cdot 1000 \tag{6.11}$$

where $FPS_{TX}$ represents the screen's frame rate. The factor of 2 arises as each QR code is transmitted using two complementary frames. By multiplying the resulting value by 1000 the absolute time ($t_{abs}$) is found in milliseconds. In the final step, the application must compensate for the time taken to decode. This elapsed time is measured using the internal system clock of the Android phone and is then added to $t_{abs}$ to have an estimate of the current timestamp of the video playback. After this, the phone starts playing the audio from the calculated time in the last step. Thus, the synchronization is achieved.

# 7

# CONCLUSION

In this thesis, we looked into novel solutions to the challenges raised by the ever-increasing number of IoT devices, namely bandwidth scarcity and energy efficiency. Over the past years, the problem of bandwidth scarcity has been partially tackled by moving towards Visible Light Communication (VLC). However, most of these efforts rely on active VLC, where the carrier light is generated by the transmitter itself. As a result, the energy efficiency of these systems is low, since emitting light needs a significant amount of power. To solve this issue, a line of research called passive VLC has emerged, using ambient light for the purpose of communication to reduce the power required by the transmitters.

In this field, optical modulators encode data inside the ambient light already present in the environment, such as that coming from the sun, ceiling lamps, or any other light source. This external modulation of light is the key to reducing power consumption, however, it requires special hardware. In Chapter 1, we introduced some candidates for this task, among which, Liquid Crystals are the most desirable in terms of power consumption. However, their main bottleneck is their very low data rate. An LC modulator cannot switch more than a few hundred times a second. Therefore, we conducted our research with the aim of developing LC-based communication links with higher speeds.

In addition to the problem of low data rate, we identified another critical gap in passive VLC: real-world proof-of-concepts and applications. Without a robust and realistic application, it is difficult to prove the viability of this new technology. As a result, we dedicated part of our efforts to find a solution to this challenge.

In this thesis, we addressed these two shortcomings of passive VLC, i.e. low data rates and lack of applications. In the next two sections, we summarize the research questions we posed as well as our contributions.

## 7.1. CONTRIBUTION TO THE DATA RATE

Increasing the data rate is a multi-faceted challenge that can be tackled from many angles, among which, we investigated two areas: (1) generating faster modulated signals with LC cells, and (2) considering classical MIMO communication methods to increase

bandwidth efficiency. These two perspectives above gave rise to the following two research questions:

*1. Can we exploit the inherent physical properties of liquid crystals to increase the data rate?*

*2. What adaptations are required to implement efficient MIMO techniques with liquid crystals?*

To answer research question 1, first, we explored an inherent property of Liquid Crystals, i.e. birefringence, to increase the data rate of passive VLC platforms. In Chapter 3, dubbed ChromaLux, we showed that stacking multiple LC cells creates peaks and valleys in their otherwise monotonic optical response. By proposing a suitable modulation scheme, we could use this more *varied* response to increase the communication speed. We also built a prototype working with sunlight, and achieved ranges up to 50 m, with a low BER. At the time we published this chapter, the only comparable work using TN cells was RetroTurbo [34], which achieved 8 kbps at a much shorter distance of about 9 meters and using a total of 64 cells (10 times more cells than ChromaLux).

In Chapter 4, called SpectraLux, we tackled research question 1 from a more detailed point-of-view. Our solution for this chapter also stacked several LC cells, however, we used a high-speed spectrometer as the receiver. This sensor gave a detailed and precise look into the light's spectrum and how the different wavelengths were modified by the stack of LC cells. We showed that the light patterns radiated by the LCs allows for the creation of a bigger symbol constellation. Using these symbols, we managed to improve the data rate of our communication link. Although the increase in the data rate was in the same order of magnitude as ChromaLux, this work was the first to take wavelengths into account. In addition, we prototyped a VLC platform with Pi cells for the first time, designed their modulation scheme, and implemented a Deep Neural Network (DNN) to recover transmitted symbols.

As our last contribution to the speed-up of LC communication links, we tackled research questions 2 in Chapter 5. In this chapter, we adapted the well-known communication methods of MIMO to passive VLC. We built a MUMIMO platform with 9 parallel channels, multiplexed by color and polarization. Our mathematical and empirical framework showed the upper limit of using polarization, and created a link operating at about 6.8 kbps using only 9 LCs. In this regard, a competitor in the SoA, RetroMU-MIMO [27], built a MIMO platform with a data rate having the same order of magnitude as our system, however, their approach did not consider parameters that can be well-controlled, such as polarization and color, but rather exploited hard-to-replicate manufacturing differences between LC cells. Thus, our platform provides a more robust MIMO design.

## 7.2. NOVEL APPLICATIONS

Although we showed the suitability of passive VLC for low-power applications, we noticed a lack of robust and useful scenarios where passive VLC plays a critical role. A technology, no matter how advanced, cannot be integrated in daily lives without a proper

use case. This observation led to following research question:

*3. What kind of applications can be developed with novel liquid crystal panels?*

We answered this question in Chapter 6, called PassiveCam, where we considered unobtrusive screen-to-camera communications. In this method, a screen transmits information to a camera, however, a viewer only sees a video and does not notice the embedded data. To make such a passive link, we used LCDs and showed how to modify them to make a passive transmitter. Then, we developed methods to encode data in videos. In addition to a modified LCD, we used a smart window as our transmitter. These windows, otherwise known as transparent screens, are being employed in public places at large scale, for instance, as window glasses at airports. Using these novel screens and our encoding methods, we created a passive VLC link transmitting to a mobile phone while causing only a minimal disturbance to a viewer. For the receiver, we developed a real-time Android application and benchmarked our platform in different scenarios to show its feasibility, robustness, and deployment potential.

In conclusion, this thesis has taken a step forward in alleviating the problems posed by the three research questions. We explored ways to speed up the slow LC modulators, developed bandwidth-efficient links, and provided an innovative use case. However, comparing the current performance (data rate, BER, distance, etc.) of passive VLC platforms with other standard technologies (mainly RF), there is still a clear need to further improve passive VLC systems.

## 7.3. FUTURE WORK



Passive VLC is still in its juvenile stage. Therefore, there are many open research questions. In the list below, we mention some of the items that seemed more prominent to us, and if solved, can make huge advancements in passive platforms.

- **Optimizing LCs**: As shown in Chapters 3 and 4, we stacked some LCs to reveal their non-linear properties. However, this is not the best way to take advantage of birefringence, as it could cause many problems. For instance, the thickness of LCs could not be tuned to obtain the desired birefringence range. In addition, when using multiple cells, precise optical alignment and electrical synchronization between the cells become issues. By making a single optimized cell, one can achieve a more robust VLC platform.

- **Finer control over wavelength**: Until now, the works that divide light's wavelengths use film color filters, which are coarse-grained and do not offer precise control over light's spectrum. By using other technologies, such as dichroic filters, optical gratings, or quantum dot color filters, the management of color channels might be possible at a finer scale. Therefore, a more efficient use of the available bandwidth will be obtained, which in turn contributes to higher data rates.

- **Novel optical modulators**: As mentioned in Chapter 2, passive modulators have different strengths. For example, piezoelectric optical modulators, have a much

higher bandwidth than Liquid Crystals. A line of research could investigate the potential of using the best property of each modulator, such as combining the high bandwidth of piezoelectric devices together with the unique optical properties of LCs. By combining the best features of different devices, a low-power and high-speed modulator might be prototyped.

Overall, passive VLC is a relatively new research area. Recent advances are all valuable, however, they hint that an interdisciplinary approach between embedded systems, chemistry, and microelectronics is needed to break the current boundaries in data rate and power consumption.

# ACKNOWLEDGEMENTS

First and foremost, I would like to thank my wife and family, who provided me with the emotional support to carry myself during the ups and downs of the Ph.D.'s journey.

Second, I would like to thank Marco Zuniga, my advisor, who was almost always involved in my journey, not only about the academic subjects, but in many other aspects of life. He and his wife never hesitated to provide help and support whenever asked for. In the academic work, he made it possible for me to appreciate research as he saw and enjoyed it. During the Corona lockdown, myself and other students were provided support and understanding by him.

Additionally, I thank Koen Langendoen, the chair of the group. His friendly attitude as well as his help during my academic journey could alleviate the path to finishing my dissertation. He was always open to listening and providing detailed feedback.

Lastly, I would like to thank people who I enjoyed collaborating with, talking, and/or hanging out with: Vivian, Miguel, Marco Kaldenbach, and Eric (Weizheng).

# BIBLIOGRAPHY


[1] *The IoT Business Index 2020*. https://impact.economist.com/perspectives/sites/default/files/eiu_arm_iot_business_index_2020_report.pdf. US.

[2] *Internet of Things: Smart cities pick up the pace, Financial times*. https://www.ft.com/content/140ae3f0-1b6f-11ea-81f0-0c253907d3e0. US.

[3] *With An Economic Potential Of 11 Trillion, Internet Of Things Is Here To Revolutionize Global Economy*. https://www.forbes.com/sites/raufarif/2021/06/05/with-an-economic-potential-of-11-trillion-internet-of-things-is-here-to-revolutionize-global-economy/. US.

[4] Keigo Nakatani et al. "A highly integrated RF frontend module including Doherty PA, LNA and switch for high SHF wide-band massive MIMO in 5G". In: *2017 IEEE Topical Conference on RF/Microwave Power Amplifiers for Radio and Wireless Applications (PAWR)*. 2017, pp. 37–39. DOI: 10.1109/PAWR.2017.7875567.

[5] Bo Tang and Petre Stoica. "MIMO Multifunction RF Systems: Detection Performance and Waveform Design". In: *IEEE Transactions on Signal Processing* 70 (2022), pp. 4381–4394. DOI: 10.1109/TSP.2022.3202315.

[6] Changyoung An and Heung-Gyoon Ryu. "MIMO receiver system using single RF front-end". In: *2014 International Conference on Signal Processing and Integrated Networks (SPIN)*. 2014, pp. 297–300. DOI: 10.1109/SPIN.2014.6776966.

[7] Peter Jung. "Time Division Multiple Access (TDMA)". In: Apr. 2003. ISBN: 9780471219286. DOI: 10.1002/0471219282.eot135.

[8] Saleh Faruque. "Frequency Division Multiple Access (FDMA)". In: Jan. 2019, pp. 21–33. ISBN: 978-3-319-91649-1. DOI: 10.1007/978-3-319-91651-4_3.

[9] D. L. HUTT, K. J. SNELL, and P. A. BÉLANGER. "Alexander Graham Bell's PHOTOPHONE". In: *Opt. Photon. News* 4.6 (June 1993), pp. 20–25. DOI: 10.1364/OPN.4.6.000020. URL: https://www.optica-opn.org/abstract.cfm?URI=opn-4-6-20.

[10] *Bluetooth website*. https://www.fcc.gov/about/overview. US.

[11] Robin Chataut and Robert Akl. "Massive MIMO systems for 5G and beyond networks—overview, recent trends, challenges, and future research direction". In: *Sensors* 20.10 (2020), p. 2753.

[12] N.O. Tippenhauer, D. Giustiniano, and S. Mangold. "Toys communicating with LEDs: Enabling toy cars interaction". In: *Proceedings of the IEEE CCNC*. 2012, pp. 48–49.

[13] Ye-Sheng Kuo et al. “Luxapose: Indoor Positioning with Mobile Phones and Visible Light”. In: *Proceedings of the 20th Annual International Conference on Mobile Computing and Networking*. MobiCom ’14. Maui, Hawaii, USA: ACM, 2014, pp. 447–458. ISBN: 978-1-4503-2783-1.

[14] Tianxing Li et al. “Human Sensing Using Visible Light Communication”. In: *Proceedings of the ACM MobiCom*. 2015.

[15] *RONJA communication system*. http://ronja.twibright.com/. US. 2024.

[16] “PureLiFi”. In: *http://purelifi.com/* ().

[17] Harald Haas et al. “What is LiFi?” In: *Journal of Lightwave Technology* 34.6 (2016), pp. 1533–1544. DOI: 10.1109/JLT.2015.2510021.

[18] *An example datasheet of an LED*. https://www.farnell.com/datasheets/1498852.pdf. US.

[19] Jin-Ping Niu and Geoffrey Ye Li. “An Overview on Backscatter Communications”. In: *Journal of Communications and Information Networks* 4.2 (2019), pp. 1–14. DOI: 10.23919/JCIN.2019.8917868.

[20] Colby Boyer and Sumit Roy. “— Invited Paper — Backscatter Communication and RFID: Coding, Energy, and MIMO Analysis”. In: *IEEE Transactions on Communications* 62.3 (2014), pp. 770–785. DOI: 10.1109/TCOMM.2013.120713.130417.

[21] H. Stockman. “Communication by Means of Reflected Power”. In: *Proceedings of the IRE* 36.10 (1948), pp. 1196–1204. DOI: 10.1109/JRPROC.1948.226245.

[22] Lingkun Li, Pengjin Xie, and Jiliang Wang. “Rainbowlight: Towards low cost ambient light positioning with mobile phones”. In: *Proceedings of the 24th Annual International Conference on Mobile Computing and Networking*. 2018, pp. 445–457.

[23] Chun-Ling Chan, Hsin-Mu Tsai, and Kate Ching-Ju Lin. “POLI: Long-Range Visible Light Communications Using Polarized Light Intensity Modulation”. In: *Proceedings of the 15th Annual International Conference on Mobile Systems, Applications, and Services*. MobiSys ’17. Niagara Falls, New York, USA: ACM, 2017, pp. 109–120. ISBN: 978-1-4503-4928-4.

[24] Zhao Tian et al. “PolarTag: Invisible Data with Light Polarization”. In: *Proceedings of the 21st International Workshop on Mobile Computing Systems and Applications*. 2020, pp. 74–79.

[25] Zhice Yang et al. “Wearables Can Afford: Light-weight Indoor Positioning with Visible Light”. In: *Proceedings of the 13th Annual International Conference on Mobile Systems, Applications, and Services*. MobiSys ’15. Florence, Italy: ACM, 2015, pp. 317–330. ISBN: 978-1-4503-3494-5.

[26] Talia Xu, Miguel Chávez Tapia, and Marco Zúñiga. “Exploiting Digital Micro-Mirror Devices for Ambient Light Communication”. In: *19th USENIX Symposium on Networked Systems Design and Implementation (NSDI 22)*. Renton, WA: USENIX Association, Apr. 2022, pp. 387–400. ISBN: 978-1-939133-27-4. URL: https://www.usenix.org/conference/nsdi22/presentation/xu-talia.

[27] Kenuo Xu et al. “Low-Latency Visible Light Backscatter Networking with Retro-MUMIMO”. In: *Proceedings of the Twentieth ACM Conference on Embedded Networked Sensor Systems* (Nov. 2022). DOI: 10.1145/3560905.3568507. URL: http://dx.doi.org/10.1145/3560905.3568507.

[28] Q.H. Spencer et al. “An introduction to the multi-user MIMO downlink”. In: *IEEE Communications Magazine* 42.10 (2004), pp. 60–67. DOI: 10.1109/MCOM.2004.1341262.

[29] *Liquid Crystal datasheet*. https://www.excel-display.com/LightValve.pdf. 2024.

[30] Texas Instruments. *DLP2000 (.2 nHD) DMD Datasheet*. Accessed: 30-1-2024.

[31] *Electro Optical modulators*. https://www.thorlabs.com/newgrouppage9.cfm?objectgroup_id=2729. 2024.

[32] Purui Wang et al. “Renovating road signs for infrastructure-to-vehicle networking: a visible light backscatter communication and networking approach”. In: *Proceedings of the 26th Annual International Conference on Mobile Computing and Networking*. 2020, pp. 1–13.

[33] Xieyang Xu, *et al.* “PassiveVLC: Enabling Practical Visible Light Backscatter Communication for Battery-free IoT Applications”. In: *MobiCom*. 2017, pp. 180–192.

[34] Yue Wu et al. “Turboboosting Visible Light Backscatter Communication”. In: *Proceedings of the Annual conference of the ACM Special Interest Group on Data Communication on the applications, technologies, architectures, and protocols for computer communication*. 2020, pp. 186–197.

[35] Michel Mitov. “Liquid-Crystal Science from 1888 to 1922: Building a Revolution”. In: *Chemphyschem : a European journal of chemical physics and physical chemistry* 15 (May 2014). DOI: 10.1002/cphc.201301064.

[36] *“Neamtic” meaning*. https://www.merriam-webster.com/dictionary/nematic. US.

[37] *Pi cell introduction*. http://www.liquidcrystaltechnologies.com/tech_support/Pi_Cell.htm. US. 2024.

[38] M. Koden et al. “Ferroelectric liquid crystal display”. In: *Shapu Giho/Sharp Technical Journal* (Dec. 1997), pp. 47–50.

[39] *A Ferroelectric liquid crystal on Silicon (FLCoS) manufacturer*. https://www.kopin.com/technologies-products/commercially-available-products/spatial-light-modulators/. US. 2024.

[40] Miguel Tapia et al. “SunBox: Screen-to-Camera Communication with Ambient Light”. In: *Proceedings of the ACM on Interactive, Mobile, Wearable and Ubiquitous Technologies* 6 (July 2022), pp. 1–26. DOI: 10.1145/3534602.

[41] *Hamamatsu line sensors*. https://www.hamamatsu.com/jp/en/product/optical-sensors/x-ray-sensor/x-ray-image-sensor/x-ray-line-sensor.html. 2024.

7

[42] Jiangtao Li, *et al.* “Retro-VLC: Enabling Battery-free Duplex Visible Light Communication for Mobile and IoT Applications”. In: *HotMobile*. 2015.

[43] Sihua Shao, Abdallah Khreishah, and Hany Elgala. “Pixelated VLC-Backscattering for Self-Charging Indoor IoT Devices”. In: *IEEE Photonics Technology Letters* 29 (2017), pp. 177–180.

[44] Rens Bloom, Marco Zúñiga Zamalloa, and Chaitra Pai. “LuxLink: creating a wireless link from ambient light”. In: *Proceedings of the 17th Conference on Embedded Networked Sensor Systems*. 2019, pp. 166–178.

[45] Qing Wang, Marco Zuniga, and Domenico Giustiniano. “Passive Communication with Ambient Light”. In: *Proceedings of the 12th International on Conference on Emerging Networking EXperiments and Technologies*. CoNEXT ’16. Irvine, California, USA: ACM, 2016, pp. 97–104. ISBN: 978-1-4503-4292-6.

[46] *VideoWindow*. https://www.videowindow.eu/. 2023.

[47] Anran Wang et al. “InFrame: Multiflexing Full-Frame Visible Communication Channel for Humans and Devices”. In: *Proceedings of the 13th ACM Workshop on Hot Topics in Networks, HotNets 2014*. New York, NY, USA, Oct. 2014. DOI: 10.1145/2670518.2673867.

[48] Anran Wang et al. “InFrame++: Achieve Simultaneous Screen-Human Viewing and Hidden Screen-Camera Communication”. In: *Proceedings of the 13th Annual International Conference on Mobile Systems, Applications, and Services*. New York, NY, USA: Association for Computing Machinery, May 2015, pp. 181–195. DOI: 10.1145/2742647.2742652.

[49] Viet Nguyen et al. “High-rate flicker-free screen-camera communication with spatially adaptive embedding”. In: *IEEE INFOCOM 2016 - The 35th Annual IEEE International Conference on Computer Communications*. Apr. 2016, pp. 1–9. DOI: 10.1109/INFOCOM.2016.7524512.

[50] Kai Zhang et al. “ChromaCode: A Fully Imperceptible Screen-Camera Communication System”. In: *Proceedings of the 24th Annual International Conference on Mobile Computing and Networking*. MobiCom ’18. New Delhi, India: ACM, 2018, pp. 575–590. ISBN: 978-1-4503-5903-0. DOI: 10.1145/3241539.3241543. URL: http://doi.acm.org/10.1145/3241539.3241543.

[51] Vu Tran et al. “DeepLight: Robust & Unobtrusive Real-Time Screen-Camera Communication for Real-World Displays”. In: *Proceedings of the 20th International Conference on Information Processing in Sensor Networks (Co-Located with CPS-IoT Week 2021)*. New York, NY, USA: Association for Computing Machinery, May 2021, pp. 238–253. DOI: 10.1145/3412382.3458269.

[52] Mostafa Izz et al. “Uber-in-Light: Unobtrusive Visible Light Communication Leveraging Complementary Color Channel”. In: *IEEE INFOCOM 2016 - The 35th Annual IEEE International Conference on Computer Communications*. IEEE Press, 2016, pp. 1–9. DOI: 10.1109/INFOCOM.2016.7524513.

[53] Kun Qian et al. “AIRCODE: Hidden Screen-Camera Communication on an Invisible and Inaudible Dual Channel”. In: *18th USENIX Symposium on Networked Systems Design and Implementation (NSDI 21)*. USENIX Association, Apr. 2021, pp. 457–470. ISBN: 978-1-939133-21-2. URL: https://www.usenix.org/conference/nsdi21/presentation/qian.

[54] F. Donald Bloss. “Optical Crystallography. Mineralogical Society of America Monograph Series, No. 5., 1999 ISBN 0939950499.” In: *Journal of Petrology* 43.3 (Mar. 2002), pp. 579–580. ISSN: 0022-3530.

[55] Yang Zou et al. “Interference colors of nematic liquid crystal films at different applied voltages and surface anchoring conditions”. In: *Opt. Express* 19.4 (Feb. 2011), pp. 3297–3303.

[56] Markus Bauer. *Michel-Levy chart*. https://github.com/markus-bauer/calculated_Michel_Levy_Chart. 2017.

[57] Bjørn Sørensen. “A revised Michel-Lévy interference colour chart based on first-principles calculations”. In: *European Journal of Mineralogy* 1 (Feb. 2013).

[58] *Active 3D glass*. https://bit.ly/31hKJ4m. 2020.

[59] Vsevolod Fréedericksz and V Zolina. “Forces causing the orientation of an anisotropic liquid”. In: *Transactions of the Faraday Society* 29.140 (1933), pp. 919–930.

[60] Alfeus Sunarso, Tomohiro Tsuji, and Shigeomi Chono. “Molecular dynamics simulation of backflow generation in nematic liquid crystals”. In: *Applied physics letters* 93.24 (2008), p. 244106.

[61] *Active 3D glass*. https://www.adafruit.com/product/3330. 2020.

[62] Hadi Askari et al. “Electrical and optical properties of ITO thin films prepared by DC magnetron sputtering for low-emitting coatings”. In: *arXiv preprint arXiv:1409.5293* (2014).

[63] Nikolaos Voudoukis and Sarantos Oikonomidis. “Inverse square law for light and radiation: A unifying educational approach”. In: *European Journal of Engineering Research and Science* 2.11 (2017), pp. 23–27.

[64] Seyed Keyarash Ghiasi, Marco A. Zúñiga Zamalloa, and Koen Langendoen. “A Principled Design for Passive Light Communication”. In: *Proceedings of the 27th Annual International Conference on Mobile Computing and Networking*. MobiCom ’21. New Orleans, Louisiana: Association for Computing Machinery, 2021, pp. 121–133. ISBN: 9781450383424. DOI: 10.1145/3447993.3448629. URL: https://doi.org/10.1145/3447993.3448629.

[65] *Liquid crystal technologies*. http://liquidcrystaltechnologies.com/. Accessed: 2022-05-12. 2016.

[66] Shu-Hsia Chen and Chiu-Lien Yang. “Dynamics of twisted nematic liquid crystal pi-cells”. In: *Applied physics letters* 80.20 (2002), pp. 3721–3723.

[67] Hongfei Cheng and Hongjin Gao. “Dynamic simulation of Pi-cell liquid crystal displays”. In: *Liquid Crystals* 28.9 (2001), pp. 1337–1341.

[68] F. Pedregosa, *et al.* “Scikit-learn: Machine Learning in Python”. In: *Journal of Machine Learning Research* 12 (2011), pp. 2825–2830.

[69] François Chollet et al. *Keras*. https://keras.io. 2015.

[70] *Benchtop Spectroscope*. https://www.patonhawksley.com/product-page/benchtop-spectroscope. 2022.

[71] Neil A Rebolledo, Dmitri C Kyle, and Daniel P Phipps. “Achromatic ferroelectric liquid crystal polarization rotator”. In: *Polarization: Measurement, Analysis, and Remote Sensing XIII*. Vol. 10655. SPIE. 2018, pp. 38–44.

[72] Nanhuan Mi et al. “CBMA: Coded-Backscatter Multiple Access”. In: *2019 IEEE 39th International Conference on Distributed Computing Systems (ICDCS)*. 2019, pp. 799–809. DOI: 10.1109/ICDCS.2019.00084.

[73] Chen He et al. *On the performance of MIMO RFID backscattering channels*. en. Nov. 2012. DOI: 10.1186/1687-1499-2012-357. URL: http://dx.doi.org/10.1186/1687-1499-2012-357.

[74] GG Raleigh and John M Cioffi. “Spatio-temporal coding for wireless communications”. In: *Proceedings of GLOBECOM'96. 1996 IEEE Global Telecommunications Conference*. Vol. 3. IEEE. 1996, pp. 1809–1814.

[75] Seyed Keyarash Ghiasi et al. “SpectraLux: Towards Exploiting the Full Spectrum with Passive VLC”. In: *Proceedings of the 22nd International Conference on Information Processing in Sensor Networks*. IPSN '23. San Antonio, TX, USA: Association for Computing Machinery, 2023, pp. 274–287. URL: https://doi.org/10.1145/3583120.3586966.

[76] *Anonymous demo, black and white*. http://tinyurl.com/2kjkb46r. 2023.

[77] *Anonymous demo, colored*. http://tinyurl.com/3t6mxhy8. 2023.

[78] Rina Doherty et al. “Keeping users in the flow: mapping system responsiveness with user experience”. In: *Elsevier Procedia Manufacturing* (2015).

[79] Satoshi Abe et al. “Imperceptible Color Vibration for Screen-Camera Communication via 2D Binary Pattern”. In: *ITE Transactions on Media Technology and Applications*. Vol. 8. July 2020, pp. 170–185. DOI: 10.3169/mta.8.170.

[80] Sahar Ammar et al. “Sun-Fi: Architecting Glass for Sunlight Data Transmission”. In: *IEEE Communications Magazine* (2023).